


May 2023

# Stoichiometric Determination of Hydride Materials at Extreme Conditions

Gregory Alexander Smith

Follow this and additional works at: <https://digitalscholarship.unlv.edu/thesesdissertations>

 Part of the [Condensed Matter Physics Commons](#), [Other Physics Commons](#), and the [Physical Chemistry Commons](#)

---

## Repository Citation

Smith, Gregory Alexander, "Stoichiometric Determination of Hydride Materials at Extreme Conditions" (2023). *UNLV Theses, Dissertations, Professional Papers, and Capstones*. 4781.  
<http://dx.doi.org/10.34917/36114806>

This Dissertation is protected by copyright and/or related rights. It has been brought to you by Digital Scholarship@UNLV with permission from the rights-holder(s). You are free to use this Dissertation in any way that is permitted by the copyright and related rights legislation that applies to your use. For other uses you need to obtain permission from the rights-holder(s) directly, unless additional rights are indicated by a Creative Commons license in the record and/or on the work itself.

This Dissertation has been accepted for inclusion in UNLV Theses, Dissertations, Professional Papers, and Capstones by an authorized administrator of Digital Scholarship@UNLV. For more information, please contact [digitalscholarship@unlv.edu](mailto:digitalscholarship@unlv.edu).

STOICHIOMETRIC DETERMINATION OF HYDRIDE MATERIALS AT EXTREME  
CONDITIONS

By

Gregory Alexander Smith

Bachelor of Science - Chemistry  
University of Nevada, Las Vegas  
2018

A dissertation submitted in partial fulfillment  
of the requirements for the

Doctor of Philosophy - Chemistry

Department of Chemistry and Biochemistry  
College of Sciences  
The Graduate College

University of Nevada, Las Vegas  
May 2023

April 6, 2023

This dissertation prepared by

Gregory Alexander Smith

entitled

Stoichiometric Determination of Hydride Materials at Extreme Conditions

is approved in partial fulfillment of the requirements for the degree of

Doctor of Philosophy - Chemistry  
Department of Chemistry and Biochemistry

Paul Forster, Ph.D.  
*Examination Committee Co-Chair*

Ashkan Salamat, Ph.D.  
*Examination Committee Co-Chair*

Clemens Heske, Ph.D.  
*Examination Committee Member*

Keith V. Lawler, Ph.D.  
*Examination Committee Member*

Jason Steffen, Ph.D.  
*Graduate College Faculty Representative*

Alyssa Crittenden, Ph.D.  
*Vice Provost for Graduate Education &  
Dean of the Graduate College*

# ABSTRACT

## STOICHIOMETRIC DETERMINATION OF HYDRIDE MATERIALS AT EXTREME CONDITIONS

By

Gregory Alexander Smith

⟨Paul Forster⟩, Examination Committee Co-Chair  
Professor of Chemistry and Biochemistry  
University of Nevada, Las Vegas

⟨Ashkan Salamat⟩, Examination Committee Co-Chair  
Professor of Physics and Astronomy  
University of Nevada, Las Vegas

Hydrogen was predicted to be a high-temperature superconductor at near-megabar conditions in 1968,[1] but only recently was been experimentally observed.[2] This is due to the extraneous metrological constraint of requiring 5 megabars of pressure to stabilize. A more practical approach for synthesis of high-temperature superconductors has been proposed through the use of hydride compounds. Recently, a surge of rare earth hydrides have achieved critical superconducting transition temperatures ( $T_C$ ) close to room temperature.[3, 4, 5, 6] However, due to limitations of the necessary instrumentation to achieve megabar pressures, many techniques traditionally used to measure stoichiometry are unavailable.

Three works presented in this dissertation help elucidate the difficulties in measuring hydride composition in situ using the diamond anvil cell and approaches to guide future studies. The first study observes small displacements from a light crystallographic oxygen sublattice of  $\text{GeO}_2$  in a pre-transition disordered state using complementary X-ray techniques to observe both long and short-range order.[7] More broadly, this works displays how small

changes to a light sublattice result in changes in the electrical properties. In the second study, a carbonaceous sulfur hydride is investigated using single-crystal X-ray diffraction at high pressures.[8] This work shows that even with high solid angle single crystal diffraction, it is still not possible to resolve hydrogen positions at high-pressure conditions. In the final study, measurements of both X-ray absorption and X-ray emission spectroscopy of the rare earth hydride yttrium hydride are also presented. This study shows that the sensitivity of X-ray spectroscopy to local coordination allows for whole integer resolution of stoichiometric hydride compounds.

## ACKNOWLEDGEMENTS

Thanks to my parents for their sacrifice, guidance, and love that helped shape me into the person I am. I'd like to thank Keith Lawler for always being willing to talk through science and the having the time and patience when I needed it the most. Thank you to Christian Childs for showing me the expectations I should hold myself and my work to, and being the most reliable coworker I've had. I'd like to thank Jasmine Hinton, I deeply appreciate the work you've put into the lab and all the people who make it up and being the yin to my yang over these past 5 years. And, of course, thanks to Ashkan Salamat for letting me smash every diamond I could get my hands on.

## DEDICATION

In memory of Jaymie Lydick (1971-2021)

Miss you, see you in the next one,  $\infty + \infty + 1$

## TABLE OF CONTENTS

ABSTRACT .....	iii
ACKNOWLEDGEMENTS .....	v
DEDICATION .....	vi
LIST OF TABLES .....	ix
LIST OF FIGURES .....	xii
LIST OF ABBREVIATIONS .....	xix
CHAPTER 1 INTRODUCTION .....	1
1.1 OUTLINE OF THIS WORK .....	13
1.1.1 The prevalence of pre-transition disordering in the rutile to $\text{CaCl}_2$ phase transition of $\text{GeO}_2$ .....	13
1.1.2 Carbon content drives high-temperature superconductivity in a carbonaceous sulfur hydride below 100 GPa.....	14
1.1.3 Structural determination of clathrate-like yttrium hydrides under extreme conditions.....	15
1.2 OVERVIEW OF EMPLOYED METHODS .....	15
1.2.1 Simple metal models and metallic bonding .....	15
1.2.2 The diamond anvil cell .....	18
1.2.3 High-temperature laser heating .....	19
1.2.4 X-ray diffraction .....	20
1.2.5 X-ray absorption spectroscopy (XAS) .....	23
1.2.6 X-ray Emission Spectroscopy (XES).....	28
CHAPTER 2 THE PREVALENCE OF PRE-TRANSITION OF DISORDERING IN THE RUTILE TO $\text{CaCl}_2$ PHASE TRANSITION OF $\text{GeO}_2$ .....	31
2.1 STATEMENT OF EFFORT AND PERMISSION .....	31
2.2 INTRODUCTION.....	31
2.3 METHODS .....	33
2.4 RESULTS AND DISCUSSION .....	35
2.5 CONCLUSIONS .....	48
2.6 ACKNOWLEDGEMENTS .....	49
CHAPTER 3 CARBON CONTENT DRIVES HIGH TEMPERATURE SUPERCONDUCTIVITY IN A CARBONACEOUS SULFUR HYDRIDE BELOW 100 GPa .....	50
3.1 ABSTRACT .....	50



3.2	STATEMENT OF EFFORT AND PERMISSION .....	50
3.3	MANUSCRIPT .....	50
3.4	ACKNOWLEDGEMENT .....	59
CHAPTER 4 STOICHIOMETRIC DETERMINATION OF CLATHRATE-LIKE YTTRIUM HYDRIDES AT MEGABAR CONDITIONS .....		
4.1	STATEMENT OF EFFORT AND PERMISSION .....	60
4.2	MANUSCRIPT IN PROGRESS .....	60
APPENDIX A: SUPPLEMENTARY INFORMATION TO THE PREVALENCE OF PRE- TRANSITION OF DISORDERING IN THE RUTILE TO $\text{CaCl}_2$ PHASE TRANSI- TION OF $\text{GeO}_2$ .....		
A.1	XRD DETERMINED LATTICES .....	70
A.2	1st-SHELL EXAFS FITS .....	71
A.3	TRANSPORT MEASUREMENTS .....	79
A.4	THEORY .....	80
APPENDIX B: SUPPLEMENTARY INFORMATION TO CARBON CONTENT DRIVES HIGH TEMPERATURE SUPERCONDUCTIVITY IN A CARBONACEOUS SUL- FUR HYDRIDE BELOW 100 GPa .....		
B.1	C-S-H SYNTHESIS .....	87
B.2	EXPERIMENTALLY DETERMINED BIRCH-MURNAGHAN EQUATION OF STATE FITS .....	89
B.3	SC-XRD DETERMINED STRUCTURES .....	91
B.4	$(\text{CH}_4)_x(\text{H}_2\text{S})_{2-x}\text{H}_2$ DAC1 .....	92
B.5	$(\text{CH}_4)_x(\text{H}_2\text{S})_{2-x}\text{H}_2$ DAC2 .....	99
B.6	$(\text{H}_2\text{S})_2\text{H}_2$ DAC3 .....	111
B.7	$(\text{CH}_4)_x(\text{H}_2\text{S})_{2-x}\text{H}_2$ DAC4 .....	114
B.8	HYDROGEN POSITIONS .....	117
B.9	EXTENDED TRANSPORT DATA .....	119
B.10	SIMULATIONS .....	122
APPENDIX C: SUPPLEMENTARY INFORMATION TO STOICHIOMETRIC DETER- MINATION OF CLATHRATE-LIKE YTTRIUM HYDRIDES AT MEGABAR CON- DITIONS .....		
C.1	CELL LIST .....	127
C.2	X-RAY SPECTROSCOPY .....	130
BIBLIOGRAPHY .....		156
CURRICULUM VITAE .....		157

## LIST OF TABLES

1.1	A table comparing Siegbahn and IUPAC X-ray transition notation for equivalent transitions. ....	29
2.1	Birch-Murnaghan equation of state fits across different pressure ranges. The fit was done by fixing $V_0$ to that of the undistorted rutile (0–19.7 GPa) phase. Credit: GA Smith, UNLV: EoS Analysis .....	38
A.1	Experimental unit cell parameters ( $\text{\AA}$ ) and volume ( $\text{\AA}^3$ ) measured by XRD as a function of pressure (GPa). The phase at any given pressure was determined by best Rietveld fit and is denoted as either rutile-type ( $P4_2/mnm$ ) or $\text{CaCl}_2$ -type ( $Pnmm$ ). In the rutile phase $a=b$ . The errors on the fits are reported for each pressure. Credit: GA Smith, Ashkan Salamat UNLV: XRD experiments.	70
A.2	The refined oxygen fractional coordinates and Ge-O bond lengths for the rutile and $\text{CaCl}_2$ phases. In the rutile ( $P4_2/mnm$ , 136) structure the Ge is on the 2a (0,0,0) Wyckoff site and the oxygen is on the 4f (u,u,0) site. In the $\text{CaCl}_2$ ( $Pnmm$ , 58) structure the Ge is on the 2a (0,0,0) Wyckoff site and the oxygen is on the 4g (u,v,0) site. Credit: GA Smith, Ashkan Salamat, UNLV: XRD analysis .....	71
A.3	DFT unit cell volumes ( $\text{\AA}^3$ ) and Ge-O bond lengths ( $\text{\AA}$ , both axial and basal) as a function of pressure (GPa) for the rutile phase. Credit: Daniel Schacher, Keith Lawler UNLV: Theory.....	82
A.4	DFT unit cell volumes ( $\text{\AA}^3$ ) and Ge-O bond lengths ( $\text{\AA}$ , both axial and basal) as a function of pressure (GPa) for the $\text{CaCl}_2$ phase. Credit: Daniel Schacher, Keith Lawler UNLV: Theory.....	83
B.1	The fit parameters of the 2 <sup>nd</sup> Order Birch-Murnaghan equation of state fits. Phase III/IV contributions were determined from fits to both crystals 3 and 4 from Run X2. Credit: GA Smith, UNLV, Ines Collings: EoS analysis. ....	89
B.2	Crystallographic details of $(\text{CH}_4)_x(\text{H}_2\text{S})_{2-x}\text{H}_2$ at variable pressure for c1 in DAC1. Credit: Credit: GA Smith, UNLV: Sample preparation; Ines Collings: SC-XRD analysis. ....	92
B.3	Crystallographic details of $(\text{CH}_4)_x(\text{H}_2\text{S})_{2-x}\text{H}_2$ at variable pressure for c1 in DAC1. Credit: GA Smith, UNLV: Sample preparation; Ines Collings: SC-XRD analysis. ....	93
B.4	Crystallographic details of $(\text{CH}_4)_x(\text{H}_2\text{S})_{2-x}\text{H}_2$ at variable pressure for c2 in DAC1. Credit: GA Smith, UNLV: Sample preparation; Ines Collings: SC-XRD analysis. ....	94

B.5	Crystallographic details of $(\text{CH}_4)_x(\text{H}_2\text{S})_{2-x}\text{H}_2$ at variable pressure for c2 in DAC1. Credit: GA Smith, UNLV: Sample preparation; Ines Collings: SC-XRD analysis. ....	95
B.6	Crystallographic details of $(\text{CH}_4)_x(\text{H}_2\text{S})_{2-x}\text{H}_2$ at variable pressure for c3 in DAC1. Credit: GA Smith, UNLV: Sample preparation; Ines Collings: SC-XRD analysis. ....	96
B.7	Crystallographic details of $(\text{CH}_4)_x(\text{H}_2\text{S})_{2-x}\text{H}_2$ at variable pressure for c3 in DAC1. Credit: GA Smith, UNLV: Sample preparation; Ines Collings: SC-XRD analysis. ....	97
B.8	Crystallographic details of $(\text{CH}_4)_x(\text{H}_2\text{S})_{2-x}\text{H}_2$ at variable pressure for c1 in DAC2. Credit: GA Smith, UNLV: Sample preparation; Ines Collings: SC-XRD analysis. ....	99
B.9	Crystallographic details of $(\text{CH}_4)_x(\text{H}_2\text{S})_{2-x}\text{H}_2$ at variable pressure for c1 in DAC2. Credit: GA Smith, UNLV: Sample preparation; Ines Collings: SC-XRD analysis. ....	100
B.10	Crystallographic details of $(\text{CH}_4)_x(\text{H}_2\text{S})_{2-x}\text{H}_2$ at variable pressure for c2 in DAC2. Credit: GA Smith, UNLV: Sample preparation; Ines Collings: SC-XRD analysis. ....	101
B.11	Crystallographic details of $(\text{CH}_4)_x(\text{H}_2\text{S})_{2-x}\text{H}_2$ at variable pressure for c2 in DAC2. Credit: GA Smith, UNLV: Sample preparation; Ines Collings: SC-XRD analysis. ....	102
B.12	Crystallographic details of $(\text{CH}_4)_x(\text{H}_2\text{S})_{2-x}\text{H}_2$ at variable pressure for c2 in DAC2. Credit: GA Smith, UNLV: Sample preparation; Ines Collings: SC-XRD analysis. ....	103
B.13	Crystallographic details of $(\text{CH}_4)_x(\text{H}_2\text{S})_{2-x}\text{H}_2$ at variable pressure for c3 in DAC2. Credit: GA Smith, UNLV: Sample preparation; Ines Collings: SC-XRD analysis. ....	105
B.14	Crystallographic details of $(\text{CH}_4)_x(\text{H}_2\text{S})_{2-x}\text{H}_2$ at variable pressure for c3 in DAC2. Credit: GA Smith, UNLV: Sample preparation; Ines Collings: SC-XRD analysis. ....	106
B.15	Crystallographic details of $(\text{CH}_4)_x(\text{H}_2\text{S})_{2-x}\text{H}_2$ at variable pressure for c4 in DAC2. Credit: GA Smith, UNLV: Sample preparation; Ines Collings: SC-XRD analysis. ....	108
B.16	Crystallographic details of $(\text{CH}_4)_x(\text{H}_2\text{S})_{2-x}\text{H}_2$ at variable pressure for c4 in DAC2. Credit: GA Smith, UNLV: Sample preparation; Ines Collings: SC-XRD analysis. ....	109
B.17	Crystallographic details of the $(\text{H}_2\text{S})_2\text{H}_2$ loading in DAC3. The hydrogens bonded to S were not included in the refinement. Credit: GA Smith, UNLV: Sample preparation; Ines Collings: SC-XRD analysis. ....	111
B.18	Crystallographic details of the $(\text{H}_2\text{S})_2\text{H}_2$ loading in DAC3 at 23 GPa at position 2. No hydrogen were included in the refinement. Credit: GA Smith, UNLV: Sample preparation; Ines Collings: SC-XRD analysis. ....	112
B.19	Crystallographic details of the $(\text{CH}_4)_x(\text{H}_2\text{S})_{2-x}\text{H}_2$ loading in DAC4 at 90 GPa. Credit: GA Smith, UNLV: Sample preparation; Ines Collings: SC-XRD analysis.	114

B.20  $\Delta T/T_C$  Values for runs T1 and T2. Values were calculated by normalizing Resistance over the superconducting transition and taking values between 90% and 10% of the transition. Also provided are the resistance values used to normalize each measurement. Credit: Dias Group, University of Rochester: Resistance measurements; GA Smith:  $\Delta T/T_C$  analysis. .... 119

## LIST OF FIGURES

1.1	A cartoon showing the process of condensation of a Cooper pair. In the top frame an electron passes through a lattice and in response, the lattice contracts. This creates a positively charged region over-screening the Coulombic repulsion seen in the middle frame and allows for the condensation of a Cooper pair in the final frame.[36, 37, 40] .....	3
1.2	A depiction of response of the magnetic behavior of type-I vs type-II superconductor.[36, 37, 40] .....	9
1.3	A timeline showing when superconductors were discovered and their critical superconducting transition temperature. Included are elemental superconductors, BCS superconducting alloys, cuprates, and hydrides.[3, 4, 5, 6, 10, 63, 70, 71, 72, 73, 74] .....	10
1.4	A graphic showing a representation of X-ray diffraction through Bragg's Law. Here an incident X-ray $k_{in}$ is diffracted at some angle $\theta$ and the resulting diffracted X-ray is $k_{diff}$ . The difference between these $k_{in}$ and $k_{diff}$ results in the scattering vector $Q$ . When $Q$ is equal to the reciprocal lattice vector $G$ of a crystal, diffraction can occur.[36, 37, 100] .....	22
1.5	A graphic showing the Franck-Condon principle. In this representation, a transition occurs from a ground state into a higher energy state due to the stronger overlap of the nuclear wave function. The fluorescence occurs with the same principle and a relaxation into a $\nu=2$ state occurs instead of a relaxation into the ground state.[102, 103, 105] .....	24
1.6	A showing the generic process of both XAS (left) and XES (right) techniques.[107] .....	25
2.1	(a): The central peak position from fitting the $A_{1g}$ and $B_{1g}$ Raman modes against pressure. Linear regressions have been added to both series to help guide the eye, as well as illustrate the $B_{1g}$ Raman mode's deviation from linearity around 27 GPa. (b): The enthalpy per unit cell of the rutile, $\text{CaCl}_2$ , and orthorhombically distorted rutile phase as a function of pressure. All enthalpies are normalized to that of the rutile phase for a given pressure. Credit: GA Smith, UNLV: Raman; Daniel Schacher, UNLV: Theory .....	36

2.2	A figure containing all X-ray techniques performed on GeO <sub>2</sub> in this study. (a) The pressure-volume response of the sample with a third order Birch-Murnaghan equation of state fit across all data to guide the eye. Note, there are at least two phases described by the data involved in said fit. The inset highlights deviations in the pre-transition disordered state. (b) The average Ge–O bond lengths determined from Rietveld analysis. The error bars of both XRD panels are within the symbol size. (c) The mean squared relative displacement as measured by EXAFS. The strong response between 17 and 27 GPa is attributed to the pre-transition disordered state. (d) The average Ge–O bond length determined from EXAFS with the weighted average crystallographic values. Credit: GA Smith, UNLV: Sample preparation, acquisition and analysis; Ashkan Salmat, UNLV: XRD analysis. . . . .	37
2.3	The relative change in the Ge K-edge energy as a function of pressure. These energies were determined as the first critical point of the GeO <sub>2</sub> XAS spectrum. Credit: GA Smith, UNLV: XAS Analysis . . . . .	41
2.4	The response in (top) enthalpy and (bottom) band gap associated with displacing an oxygen within its <i>ab</i> -plane of a 3×3×3 rutile supercell of GeO <sub>2</sub> at 20 GPa (left) and 25 GPa (right). Displacement by 11° relative to the rutile position (within grid resolution) marked with a black x. Credit: Daniel Schacher, Keith Lawler, UNLV: Theory . . . . .	42
2.5	(top) The charge density with an isosurface level of 0.05 $e/a_0^3$ and (bottom) electron localization function with an isosurface level of 0.5 for a 25 GPa 3×3×3 supercell of (left) pristine rutile GeO <sub>2</sub> and (right) rutile GeO <sub>2</sub> with a single 11° oxygen displacement as indicated in Figure A.11. Only one unit cell of the supercell is shown. Credit: Daniel Schacher, Keith Lawler, UNLV: Theory . . . . .	45
2.6	The band structure and projected density of states for a 25 GPa 3×3×3 supercell of (top) pristine rutile GeO <sub>2</sub> and (bottom) rutile GeO <sub>2</sub> with a single 11° oxygen displacement as indicated in Figure A.11. Credit: Daniel Schacher, Keith Lawler, UNLV: Theory . . . . .	46
2.7	Band decomposed charge densities for the (top) valence band maximum and (bottom) conduction band minimum for a 25 GPa 3×3×3 supercell of (left) pristine rutile GeO <sub>2</sub> and (right) rutile GeO <sub>2</sub> with a single 11° oxygen displacement as indicated in Figure A.11. All isosurfaces are at 0.001 $e/a_0^3$ and show only the relevant portion of the supercell. Credit: Daniel Schacher, Keith Lawler, UNLV: Theory . . . . .	47
3.1	(a) Resistance response of C-S-H (Run T1) on cooling, displaying a superconducting transition at 191 K at 97 GPa. (Inset) $R$ response from Run TN at 90 GPa showing metallic behavior. (b) Evolution of $T_c$ with $P$ for Runs T1 and T2. (c) Comparative Raman spectra of Runs T1 and T2, and Run TN at 4.0 GPa and 300 K. The feature marked with an asterisk (*) is second-order Raman scattering from diamond. Credit: Dias Group, University of Rochester: Resistance measurements and Raman; Dean Smith, UNLV: Artistic design. . . . .	52

3.2	<i>P-V</i> relations of C-S-H at 300 K compared with values from H <sub>2</sub> S and [87]. A 2 <sup>nd</sup> order Birch-Murnaghan equation of state was fit with initial volume $V_0 = 400.573 \text{ \AA}^3$ and bulk modulus $K_0 = 11.028 \text{ GPa}$ (black line), and the gray area denotes uncertainty derived from high and low bands for Runs X1 and X2. Phase division for I ( <i>I4/mcm</i> ) → II ( <i>C2/c</i> ) → III/IV ( <i>I4/mcm</i> ) are taken from [87]. Credit: GA Smith, UNLV: Sample preparation and data acquisition; Ines Collings, Centre for X-ray Analytics, Empa: SC-XRD analysis; Dean Smith, UNLV: Artistic design. ....	55
3.3	SC-XRD determined structure at (a) 9 GPa <i>I4/mcm</i> (b) 29 GPa <i>C2/c</i> and (c) 50 GPa <i>I4/mcm</i> C-S-H. (d) DFT derived structure at 90 GPa – bicolor cylinders represent bonds ( $\leq 1.43 \text{ \AA}$ ), silver cylinders represent H atoms shared between two heavy atoms (1.43–1.53 $\text{\AA}$ ), and dashed lines represent H bonds (1.53–2.0 $\text{\AA}$ ). (e) Lowest enthalpy structure found here when substituting a CH <sub>4</sub> for an H <sub>2</sub> S in the 90 GPa structure shown in (d). Yellow spheres represent S throughout, brown spheres C, and pink spheres H. Credit: Keith Lawler, UNLV: Theory. ....	56
4.1	A figure showing representative XES spectra of the various experimental data compared to the theoretical OCEAN calculations for all experimentally observed phases of yttrium hydride. Credit: GA Smith, UNLV: XES experiments; Daniel Schacher, UNLV: OCEAN calculations. ....	65
4.2	The fitted energy difference between the $k\beta_2$ transition and the $K\beta''$ transition with respect to pressure. This evolution is sensitive to coordination number, and each line can be assigned a coordination number through theoretical calculations. Theoretical energy axis has been systematically stretched by 7.5% to allow for visualization with experimental data. Credit: GA Smith, UNLV: XES experiments; Daniel Schacher, UNLV: OCEAN calculations. ....	66
4.3	a) Rietveld refinement of YH <sub>3</sub> at 194 GPa. Peak splitting of the 200 and 220 peaks show the tetragonal distortions of the Fm-3m structure. b) Rietveld refinement of the YH <sub>4</sub> data point at 147 GPa. We observe a hexagonal phase, of unknown origin. An unidentified phase is marked by asterisks. Credit: GA Smith, Emily Siska UNLV: XRD analysis. ....	68
A.1	The Rietveld refinement for the 19 GPa XRD point. Credit: GA Smith, Ashkan Salamat UNLV: XRD experiments. ....	72
A.2	The Rietveld refinement for the 21 GPa XRD point. Credit: GA Smith, Ashkan Salamat UNLV: XRD experiments. ....	73
A.3	The Rietveld refinement for the 23 GPa XRD point. Credit: GA Smith, Ashkan Salamat UNLV: XRD experiments. ....	74
A.4	The Rietveld refinement for the 25 GPa XRD point. Credit: GA Smith, Ashkan Salamat UNLV: XRD experiments. ....	75
A.5	The Rietveld refinement for the 29 GPa XRD point. Credit: GA Smith, Ashkan Salamat UNLV: XRD experiments. ....	76
A.6	The Rietveld refinement for the 31 GPa XRD point. Credit: GA Smith, Ashkan Salamat UNLV: XRD experiments. ....	77

A.7	The Rietveld refinement for the 33 GPa XRD point. Credit: GA Smith, Ashkan Salamat UNLV: XRD experiments. . . . .	78
A.8	EXAFS fits of the 1st shell of GeO <sub>2</sub> . a) the MSRD as determined from fitting the first oxygen octahedral. b) The experimentally determined bond length of the first shell. Credit: GA Smith, Daniel Sneed UNLV: XAS experiments. . . . .	78
A.9	Transport Data with no laser excitation, Resistance in tera-ohms is plotted against pressure. Around 10 GPa we reach our limit of detection of about 8.5 TΩ and believe all further measurements are unreliable past this pressure. Credit: GA Smith UNLV: High-pressure resistance experiments. . . . .	79
A.10	Enthalpy per GeO <sub>2</sub> unit cell as a function of pressure for the rutile, CaCl <sub>2</sub> , manually orthorhombically-distorted rutile, rutile with a single oxygen displaced, and the rutile and CaCl <sub>2</sub> structures with their oxygen positions swapped. The enthalpies are normalized with respect to the rutile phase. Credit: Daniel Schacher, Keith Lawler UNLV: Theory. . . . .	81
A.11	The response in (top) enthalpy and (bottom) band gap associated with displacing an oxygen in the <i>ab</i> -plane of a 2×2×2 rutile supercell of GeO <sub>2</sub> at 20 GPa (left) and 25 GPa (right). Credit: Daniel Schacher, Keith Lawler UNLV: Theory. . . . .	84
A.12	The band structure and projected density of states for a 25 GPa 2×2×2 supercell of (top) pristine rutile GeO <sub>2</sub> and (bottom) rutile GeO <sub>2</sub> with a single 31° oxygen displacement. Credit: Daniel Schacher, Keith Lawler UNLV: Theory. . . . .	85
A.13	Band decomposed charge densities for the (top) valence band maximum and (bottom) conduction band minimum for a 25 GPa 2×2×2 supercell of (left) pristine rutile GeO <sub>2</sub> and (right) rutile GeO <sub>2</sub> with a single 31° oxygen displacement. All isosurfaces are at 0.001 <i>e/a</i> <sub>0</sub> <sup>3</sup> and show only the relevant portion of the supercell. Credit: Daniel Schacher, Keith Lawler UNLV: Theory. . . . .	86
B.1	A plot of the representation of fitted results. Plotted results are presented from first measured point to the either the next phase or highest pressure for a given run. The presented phase boundaries are from the boundaries determined from SC-XRD in this work. Credit: GA Smith, UNLV, Ines Collings: EoS analysis. . . . .	90
B.2	Diamond-anvil sample chambers for experiments 1-4. Credit: GA Smith, UNLV: Sample preparation. . . . .	91
B.3	Selected reciprocal space reconstructions for crystals 1 to 3 of the (CH <sub>4</sub> ) <sub>x</sub> (H <sub>2</sub> S) <sub>2-x</sub> H <sub>2</sub> loading in DAC1. The monoclinic phase is observed for all crystals at 19-20 GPa. Credit: GA Smith, UNLV: Sample preparation; Ines Collings: SC-XRD analysis. . . . .	98
B.4	Selected reciprocal space reconstructions for crystal 1 of the (CH <sub>4</sub> ) <sub>x</sub> (H <sub>2</sub> S) <sub>2-x</sub> H <sub>2</sub> loading in DAC2. No monoclinic distortion is observed in this crystal. The diffraction spots have a large mosaicity in the <b>ab</b> -plane. Credit: GA Smith, UNLV: Sample preparation; Ines Collings: SC-XRD analysis. . . . .	100



B.5	Selected reciprocal space reconstructions for crystal 2 of the $(\text{CH}_4)_x(\text{H}_2\text{S})_{2-x}\text{H}_2$ loading in DAC2. The monoclinic distortion is observed at pressure points 24 and 26 GPa. Credit: GA Smith, UNLV: Sample preparation; Ines Collings: SC-XRD analysis. ....	104
B.6	Selected reciprocal space reconstructions for crystal 3 of the $(\text{CH}_4)_x(\text{H}_2\text{S})_{2-x}\text{H}_2$ loading in DAC2. The monoclinic distortion is observed at 18 GPa. The few reflections observed at 18 GPa is due to crystal alignment issues, which was fixed by re-defining its position after 24 GPa. Weak reflections of the monoclinic distortion are observed for pressure points 29 and 32 GPa. Credit: GA Smith, UNLV: Sample preparation; Ines Collings: SC-XRD analysis. ....	107
B.7	Selected reciprocal space reconstructions for crystal 4 of the $(\text{CH}_4)_x(\text{H}_2\text{S})_{2-x}\text{H}_2$ loading in DAC2. No monoclinic distortion is observed at 24 GPa. Crystal alignment issues means that there are no data above 9 GPa up till 24 GPa. At 24 GPa, the position of $c_4$ was re-defined. Credit: GA Smith, UNLV: Sample preparation; Ines Collings: SC-XRD analysis. ....	110
B.8	Reciprocal space reconstructions for $(\text{H}_2\text{S})_2\text{H}_2$ loading in DAC3. The 23 GPa pressure point has two reconstructions in different positions of the crystal. The $C2/c$ phase is observed for position 2 at 23 GPa. The data quality significantly reduced at 30 GPa and above, where twinning and high mosaicity in the ( <b>ab</b> )-plane are observed. Credit: GA Smith, UNLV: Sample preparation; Ines Collings: SC-XRD analysis. ....	113
B.9	Reciprocal space reconstructions for $(\text{CH}_4)_x(\text{H}_2\text{S})_{2-x}\text{H}_2$ loading in DAC4 at 90 GPa. Two twin domains are present, and each twin has additional weaker reflections visible in the diagonal of the <b>ab</b> -plane, which could be modelled using an incommensurate modulation $\mathbf{q}^*$ vector as 0.241(5) 0.237(5) 0(0.005). Credit: GA Smith, UNLV: Sample preparation; Ines Collings: SC-XRD analysis.	115
B.10	Reflections from the two twin domains (red and blue) with the incommensurate peaks from each domain. Credit: Ines Collings: SC-XRD Analysis. Credit: GA Smith, UNLV: Sample preparation; Ines Collings: SC-XRD analysis. ....	116
B.11	Figures illustrating how the hydrogen positions were allocated starting from $S_8$ for $c_3$ at 12.2 GPa. The difference Fourier maps ( $F_o - F_c$ ) are shown at the levels indicated below each figure. Credit: GA Smith, UNLV: Sample preparation; Ines Collings: SC-XRD analysis. ....	117
B.12	Figures illustrating how the hydrogen positions were allocated starting from $S_8$ for $c_1$ at 14.3 GPa. The difference Fourier maps ( $F_o - F_c$ ) are shown at the levels indicated below each figure. Credit: GA Smith, UNLV: Sample preparation; Ines Collings: SC-XRD analysis. ....	118
B.14	A comparison of the critical temperatures presented in this work with C-S-H from [3] and $\text{SH}_3$ from [175] Credit: Dean Smith, UNLV: design. ....	121
B.15	The $\Delta T/T_C$ values for runs T1 and T2 with pressure. Run T1 displays a much narrower transition than T2, which has a near three times broader transition. A least-squares trendline was added to the T1 data as a guide to the eye. Credit: Dias Group, University of Rochester: Resistance measurements; GA Smith: $\Delta T/T_C$ analysis. ....	121

B.16	4 possible arrangements of the H <sub>2</sub> S units within the refined 50 GPa <i>I4/mcm</i> structure with the lattice and S positions fixed at their refined positions (Fig. 3c of the main text), and using the H positions of the (a) <i>P1</i> structure of [160] or (b-d) constructed from the partial occupancies refined here. Each (b-d) structure was constrained to obey the ice rules and is an example of a class of arrangements with (b) being rings of stacked pinwheels pointed the same direction, (c) being linear chains in [100] with each molecular unit pointed the same direction, and (d) being linear chains along [001] with each molecular unit pointed the same direction. Credit: Keith Lawler, UNLV: Theory. . . . .	123
B.17	The optimized versions of the 50 GPa <i>I4/mcm</i> (keeping the lattice and S positions fixed at their refined positions) structures shown in Fig. SB.16; the (a-d) numbering is the same. Note the H <sub>2</sub> S molecular units in (b-d) remained planar following the optimization. The relative enthalpies are: (a) 0.000 eV, (b) 6.433 eV, (c) 5.057 eV, and (d) 4.605 eV. (d) is the most stable planar structure evaluated here. Credit: Keith Lawler, UNLV: Theory. . . . .	124
B.18	4 possible arrangements of the H <sub>2</sub> S units within the refined 9 GPa <i>I4/mcm</i> structure with the lattice and S positions fixed at their refined positions (Fig. 3a of the main text) and using the same H arrangements and (a-d) numbering as in Fig. SB.16. Credit: Keith Lawler, UNLV: Theory. . . . .	125
B.19	The optimized versions of the 9 GPa <i>I4/mcm</i> (keeping the lattice and S positions fixed at their refined positions) structures shown in Fig. SB.18. The (a-d) numbering is the same. Note that some of the H <sub>2</sub> S molecular units in each of (b-d) shifted away from being planar following the optimization. The relative enthalpies are: (a) 0.000 eV, (b) 1.136 eV, (c) 0.438 eV, and (d) 0.504 eV. Credit: Keith Lawler, UNLV: Theory. . . . .	126
B.20	(a) Lowest enthalpy DFT orientation of 50 GPa <i>I4/mcm</i> (H <sub>2</sub> S) <sub>2</sub> H <sub>2</sub> found here using the experimental unit cell and S positions. (b) The same configuration as (a) using the 90 GPa SC-XRD determined unit cell and S positions. (c) A higher enthalpy, $\Delta H = 267$ meV per unit cell not vibrationally corrected, solution than Figure 3(e) in the main text but with H <sub>2</sub> S molecular orientation more akin to what was found in (b). In (a-d), bicolor cylinders represent bonds ( $\leq 1.43$ Å), silver single color cylinders represent H atoms shared between two heavy atoms (1.43-1.53 Å), and dashed lines represent hydrogen bonds (1.53-2.0 Å). Credit: Keith Lawler, UNLV: Theory. . . . .	126
C.1	A comparison of the EXAFS fits for the <i>I4/mmm</i> YH <sub>4</sub> , <i>I4/mmm</i> YH <sub>3</sub> , and <i>Fm<math>\bar{3}</math>m</i> . The tetragonally distorted YH <sub>3</sub> exhibits the lowest fit error. GA Smith, UNLV: XAS experiments. . . . .	130
C.2	A waterfall plot of the experimentally collected and reduced spectra. In this plot, YH <sub>2</sub> , YH <sub>3</sub> , and YH <sub>4</sub> are green, blue, and red respectively. Credit: GA Smith, UNLV: XES experiments. . . . .	131
C.3	A plot showing all collected <i>K</i> $\beta$ <sub>1</sub> and <i>K</i> $\beta$ <sub>3</sub> spectra of Y metal and YH <sub><i>x</i></sub> samples between ambient and 2 Mbar. There is no apparent change. Between each figure is a 0.1 offset for comparison. Credit: GA Smith, UNLV: XES experiments. . . . .	132

C.4 The energy difference presented in Fig. 4.2 without the systematic 7.5% stretching in energy of theory. Credit: GA Smith, UNLV: XES experiments. 133

## LIST OF ABBREVIATIONS

ANL Argonne National Laboratory

APS Advanced photon source

BCS Bardeen-Cooper-Schrieffer

BMD Bending magnet D

DAC Diamond anvil cell

DFT Density Functional Theory

EXAFS Extended x-ray absorption fine structure

FWHM Full width half maximum

GGA Generalized Gradient Approximations

HPCAT High pressure collaborative access team

IR Infrared

LDA Local-density Approximation

MSRD Mean Square Relative Displacement

NBSE NIST Bethe-Salpeter Equation NIST National Institute of Standards and Technology

OCEAN Obtaining Core Excitations from Ab-initio calculations and NBSE

PBE Perdew-Burke-Ernzerhof

UV ultra violet

PTM Pressure transmitting medium

VASP Vienna ab-initio simulation package

VTC Valence to core

XANES X-ray absorption near edge structure

XAS X-ray absorption spectroscopy

XES X-ray emission spectroscopy

XRD X-ray diffraction

# CHAPTER 1

## INTRODUCTION

Since the first observation of superconductivity in elemental mercury by Onnes in 1911, materials with ever-increasing superconducting critical transition temperatures ( $T_C$ ) have been sought after.[9] Mercury displayed a  $T_C$  of just 4.2 K, only achievable through his recent achievement of liquefying helium just three years earlier.[10] Bardeen-Cooper-Schrieffer (BCS) theory sufficiently described most discovered superconductors when initially proposed in 1957, leading to an eventual Noble Prize in 1972.[11, 12, 13] While this phenomenon was notable, early superconductors had low critical temperatures ( $<40$  K).[14, 15, 16, 17] This limitation necessitated superconductors to be cooled by helium until the discovery of a new class of unconventional superconductors, the cuprates.[18, 19, 20, 21, 22, 23, 24, 25] The discovery of cuprates in 1986 resulted in a rapid increase of known  $T_C$  beyond liquid nitrogen temperatures (77 K). The mechanism by which cuprates achieve superconductivity is not well described by BCS theory and remains poorly understood, presenting a major obstacle to the discovery of materials with optimized superconducting properties. [26, 27] Still, these materials would retain the highest  $T_C$ [28, 29] until they were overtaken by a covalent high-pressure hydride with the discovery of  $\text{H}_3\text{S}$  in 2015.[30] To better understand modern hydride superconductors, we must first understand why they are such effective superconductors. To understand this, we must consider the behavior of metallic hydrogen under pressure.

Hydrogen was predicted to have a high-pressure atomic phase by Wigner and Huntington in 1935, that would display metallic behavior.[31] The metallization of hydrogen is necessary to achieve superconductivity.[11, 12, 13] In a 1-D chain toy model, Peierls distortions can help give insight into the process of metallization of dimer. Peierls distortions result in metal-to-insulator transitions in 1-D solids by introducing a systematic displacement into

a 1-D chain of regularly spaced atoms. The result of this displacement is the appearance of a band gap near the Fermi energy. Physically, this behavior can be explained through the dimerization of a species. Reduction of the bond order leading to lengthening of the coordination length of a dimer results in the regular spacing of atoms along a 1-D chain and can eliminate the associated band gap.[32] However, in molecular hydrogen this effect is not observed as a response to pressure and hydrogen becomes semi-metallic as an indirect bandgap closes.[33, 34] Upon further compression, the bandgap closes and results in hydrogen becoming metallic.[2, 35] Unlike in covalent molecular species (such as the H<sub>2</sub> dimer) that bond through the overlap of the electron orbital overlap, metals bond through attractive electrostatic forces that arise as a result of shared delocalized electron density.[36, 37] A short description of metallic bonding and the Drude and Sommerfeld models can be found in section 1.2.1.

The atomic metallic hydrogen phase would later be predicted to be a high-temperature superconductor by Ashcroft in 1968 at pressures below a megabar.[1] One of the main reasons this was expected was the intrinsically high Debye temperature in hydrogen that is proportional to  $T_C$  in classical BCS theory. In BCS theory, when an electron travels through a lattice, it could cause a Coulombic attraction with the positively charged lattice.[11, 12, 13] This interaction makes good sense as the interaction of two simple charged particles can be described as follows.[38, 39]

$$\mathbf{F} = k_e \frac{q_1 q_2}{|r^2|} \hat{r} \quad (1.1)$$

Where  $\mathbf{F}$  is the vector force,  $k_e$  is equal to  $1/4\pi\epsilon_0$ ,  $q$  is the charge of each particle,  $r$  is the distance between the particles, and  $\hat{r}$  is the normalized unit vector between particles  $r_1 - r_2/|r_1 - r_2|^2$ . A cationic lattice contraction leads to a dense, positively charged region that can once again attract electrons. This region could "overscreen" the Coulombic repulsion resulting in a net positive attraction between electrons. A cartoon of this process can be seen in Fig. 1.1.

When this occurs, it would allow electrons to condense into a Cooper pair where the

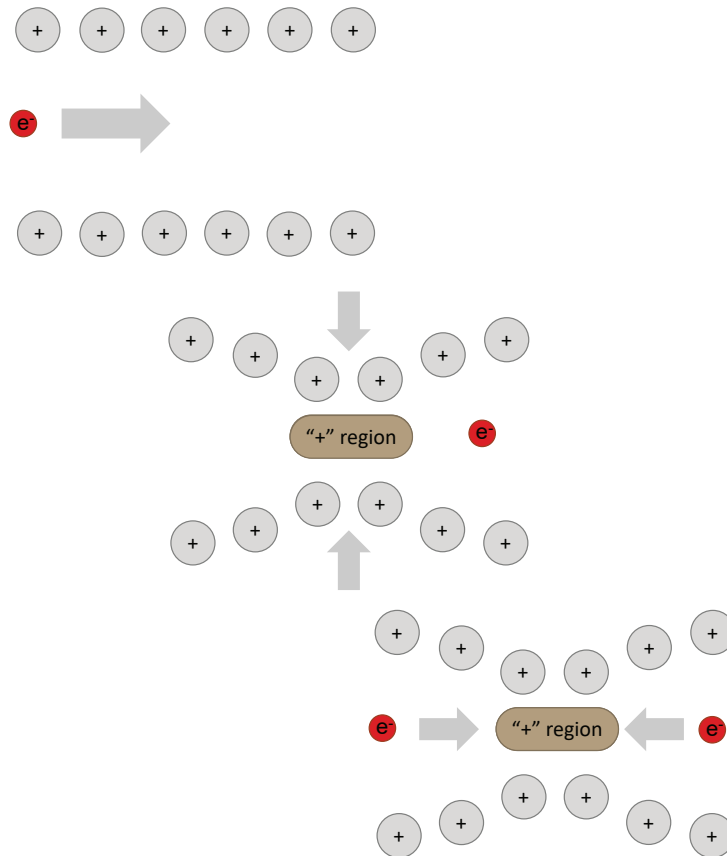


Figure 1.1: A cartoon showing the process of condensation of a Cooper pair. In the top frame an electron passes through a lattice and in response, the lattice contracts. This creates a positively charged region over-screening the Coulombic repulsion seen in the middle frame and allows for the condensation of a Cooper pair in the final frame.[36, 37, 40]



electrons behave as a boson rather than a Fermion. This behavior is critical as it results in electrons no longer needing to follow the Pauli exclusion principle.[41] As a result, the material can enter a superconducting state such that current can pass through the material with no resistance.

As the system enters a superconducting state, an energy gap  $\Delta(\omega)$  occurs.[36, 40, 42] The symmetry about this gap is how the superconducting symmetry is defined. If this gap is symmetric about the Fermi surface, it is said to have s-wave superconducting symmetry. Other orders exist, typically in unconventional superconductors such as the cuprates, where d-wave symmetry occurs displaying four lobes about the Fermi surface of alternating phase.[43] Recently, p-type symmetry has been claimed in thin-films of the iron pnictide, NdFeAs(O, F).[44]

In classical BCS theory, the critical transition temperature is proportional to the Debye temperature defined as the temperature at which all available vibrational modes in a system are excited and for a cubic system can be expressed as follows.[36, 37]

$$\theta_D = \frac{\hbar\nu}{k_B} \left( \frac{6\pi^2 N}{V} \right)^{1/3} \quad (1.2)$$

Where  $\theta_D$  is the Debye temperature,  $\hbar$  is Planck's constant divided by  $2\pi$ ,  $\nu$  is the constant speed of sound in the crystal,  $k_B$  is the Boltzmann constant,  $N$  is the number of phonon modes in the species, and  $V$  is the volume. This is directly related to the Debye frequency, which is the maximum phonon frequency allowed by the model as the following.

$$\omega_D = \frac{\hbar}{k_B} \theta_D \quad (1.3)$$

It makes good logical sense that the lighter the species on a spring, the greater their maximum frequency can be, so it follows that hydrogen should have the largest possible Debye frequency, and hence, the highest Debye temperature. The classical BCS  $T_C$  equation

Ashcroft presented in his 1968 paper is as follows.[1]

$$T_C = 0.85\theta_{De} \frac{1}{N_0 V} \quad (1.4)$$

Here the critical superconducting transition temperature is a function of the Debye temperature, where  $N_0$  is the density of states at the Fermi level and  $V$  is the coupling potential. BCS theory struggled to accurately predict  $T_C$  for materials with strong electron-phonon coupling and further evaluations of superconducting theory were implemented to help describe strong electron-phonon couplers. Migdal showed that it was possible to accurately describe electron-phonon coupling in simple metals.[45] Eliashberg built upon Migdal's work and extended them for superconductors using Green's function.[46] While Eliashberg's formalisms are somewhat formidable, introducing what is now called the Eliashberg spectral function  $\alpha^2 F(\omega)$  helped better describe strong-coupling superconductors, like hydrogen. Presented below is the spectral function as it appears in Allen and Dynes's 1975 paper.[47]

$$\alpha^2 F(\omega) = N_{\uparrow}(0) \frac{\sum_{kk'} |M_{kk'}|^2 \delta(\omega - \omega_Q) \delta(\epsilon_k) \delta(\epsilon_{k'})}{\sum_{kk'} \delta(\epsilon_k) \delta(\epsilon_{k'})} \quad (1.5)$$

Here,  $N_{\uparrow}(0)$  is the single spin density of electronic states at the Fermi surface,  $|M_{kk'}|^2$  is the electron-phonon matrix element, and the delta functions are, essentially, boundary conditions to limit the application to the Fermi surface.  $Q = k - k'$  is the scattering wave vector,  $\omega_Q$  is the frequency of phonon  $Q$  and  $\epsilon_k$  is the kinetic energy of electron  $k$ . The spectral function expresses electron-phonon coupling as a function of frequency  $\omega$  and is used to calculate the dimensionless electron-phonon coupling constant through the following equation.

$$\lambda = 2 \int_0^{\infty} \frac{d\omega \alpha^2 F(\omega)}{\omega} \quad (1.6)$$

Morel and Anderson helped better describe the effective Coulomb repulsion in electron-phonon coupling systems.[48] This was necessary as electrons behave on time scales a factor

$10^3$  faster than phonons.

$$\frac{1}{\mu^*} = \frac{1}{\mu} + \ln \left( \frac{\omega_{el}}{\omega_{ph}} \right) \quad (1.7)$$

Where  $\mu^*$  is the Coulomb pseudo potential,  $\mu$  is the instantaneous Coulomb repulsion,  $\omega_{el}/\omega_{ph}$  is the ratio of propagation time of the plasma frequency to the high-frequency cutoff of the Eliashberg spectral function. Using these parameters, McMillan created a modern interpretation for calculating the superconducting transition critical temperature of an electron-phonon mediated superconductor. Allen and Dynes then would correct the implementation of the Debye temperature by replacing it with a term to represent the characteristic phonon frequency based on the strength of the electron-phonon coupling.

$$T_C = \frac{\omega_{log}}{1.2} \exp \left( -\frac{1.04(1 + \lambda)}{\lambda - \mu^*(1 + 0.62\lambda)} \right) f_1 f_2 \quad (1.8)$$

The Allen-Dynes correction to the McMillan equation is the logarithmic average frequency term  $\omega_{log}$ , replacing the Debye temperature. For weak electron-phonon couplers ( $\lambda < 1.5$ ), the McMillan equation performs well and the . For strong electron-phonon couplers, further correction terms were implemented by Allen and Dynes[47] to equation 1.8.

$$f_1 = [1 + (\lambda/\Lambda_1)^{3/2}]^{1/3} \quad (1.9)$$

$$f_2 = 1 + \frac{(\bar{\omega}_2/\omega_{log} - 1)\lambda^2}{\lambda^2 + \Lambda_2^2} \quad (1.10)$$

Where

$$\Lambda_1 = 2.46(1 + 3.8\mu^*) \quad (1.11)$$

and

$$\Lambda_2 = 1.82(1 + 6.3\mu^*)(\bar{\omega}_2/\omega_{log}). \quad (1.12)$$

$f_1$  and  $f_2$  are the strong-coupling correction and shape correction respectively and are multiplied by the McMillan calculated  $T_C$ . These correction terms were designed to scale to as  $\lambda^{1/2}$

and  $\bar{\omega}_2/\omega_{log}$  for large  $\lambda$  and are presented below. For weak electron-phonon couplers, these correction terms go to zero. These empirical terms are determined through least-squares analysis.[47] For extremely strong electron-phonon couplers ( $\lambda > 10$ ), Allen and Dynes proposed using  $\langle \omega^2 \rangle^{1/2}$  instead of  $\omega_{log}$ . These  $\langle \omega^n \rangle$  terms are the  $n$ th moment of the normalized weight function  $g(\omega)$  and can be expressed as follows.

$$\langle \omega^n \rangle = \frac{2}{\lambda} \int \alpha^2 F(\omega) \omega^{n-1} d\omega \quad (1.13)$$

A notable feature of the McMillan-Allen-Dynes equation is that for weak-coupling superconductors ( $\lambda \ll 1$ ), the equation reduces to be very similar to the classical BCS version with the  $\lambda - \mu^*$  assuming the role of  $N_0 V$ .

As history would prove, the pressure required to metalize hydrogen was much greater than a megabar, nearly 500 GPa. The pressure and care required to produce such pressures in a hydrogen medium was the driving force that advanced high-pressure techniques and instrumentation for many years.[2, 49, 50, 51, 52, 53, 54, 55] These experimental conditions would require nearly 50 years to achieve, finally being performed by Dias *et al.* in 2017.[2] These experimental conditions require an extraordinary feat to achieve, and as such, are difficult to reproduce.

Looking for materials where similar superconducting behavior occurs, but at significantly lower pressures, is necessary to make a practical material. High-pressure turned to hydrides in 2004 when Ashcroft predicted that adding a cationic atom to hydrogen could facilitate a chemical pre-compression of hydrogen, leading to superconductivity in the hydrogen metal sublattice, but at significantly lower pressures.[56] Binary hydrides were predicted to resemble the superconductivity behavior of metallic hydrogen at significantly lower pressures, typically around 1.5 Mbar in  $MH_6$ [57, 58] systems and, eventually, the field turned towards more hydrogen-rich, rare earth hydrides adopting  $REH_9$  and  $REH_{10}$  structures.[59, 60] The heavy cationic species could help to coordinate dense hydrogen sublattices or add electron density to

the anti-bonding  $\sigma^*$  states to facilitate the Wigner-Huntington-like state of metallic hydrogen or both, and as a result, was predicted to increase  $T_C$  substantially.[61] This prediction was verified experimentally, with multiple hydrides with high-temperature superconductivity being discovered in the ensuing years. ThH<sub>10</sub>[62], YH<sub>9</sub>[4], LaH<sub>10</sub>[5], CaH<sub>6</sub>[63], C-S-H[3], and H<sub>3</sub>S[30] all display high-temperature superconductivity. These materials rapidly increased  $T_C$  again, with the caveat that these materials could not be used for devices, as only nanograms of these samples could be synthesized at a time due to high pressures necessary for synthesis, and the release of pressure resulted in decomposition.

In general, there have been two broad pathways to achieving high  $T_C$  in hydride materials: metal hydrides and, more recently, covalent hydrides. The breakthrough observation of superconductivity at 203 K and 155 GPa in H<sub>3</sub>S in 2015 reframed the landscape of high-temperature superconductors.[30] H<sub>3</sub>S is predicted to be a conventional phonon-mediated type-II superconductor. A conventional superconductor is a superconductor with properties well predicted by BCS theory, such as  $T_C$  or  $H_c$ . When a superconductor enters a superconducting state the material will generate surface currents that create a magnetic field that exactly expels the internal magnetic field. This process is known as the Meissner effect. The difference between type-I and type-II superconductors is defined by their response to a magnetic field. An applied magnetic field of strength  $H$  above the critical superconducting field strength  $H_c$  will dispel superconductivity in a type-I superconductor, similar to how temperatures above  $T_C$  quench superconductive behavior.[36, 37] In a type-II superconductor, there are two critical magnetic fields. For a magnetic field below the first critical magnetic field,  $H_{c1}$  the material behaves as it would in a type-I superconductor. Above the second critical magnetic field,  $H_{c2}$ , superconductivity is destroyed. Between these two fields, the material allows magnetic flux through vortices, but the material behaves as a superconductor outside the vortices. The magnetic fields sustainable by a type-II superconductor, on the order of magnitude of 10s of Tesla, are typically much higher than those of type-I superconductors, making type-II superconductors an appealing choice for magnets that can sustain high fields.

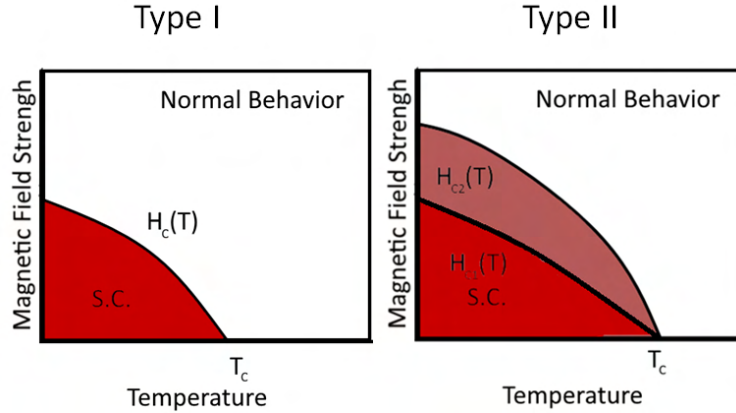


Figure 1.2: A depiction of response of the magnetic behavior of type-I vs type-II superconductor.[36, 37, 40]

A visual summary can be found in Fig. 1.2.

$\text{H}_3\text{S}$  was found to be a superconductor in the clean limit under Mbar conditions.[64] In the clean limit, the coherence length agrees with its theoretical Ginzberg-Landau coherence length. The coherence length in a superconductor,  $\xi$ , is the length over which the superconducting state can be maintained and is described as the average distance between the electrons of a Cooper pair.[40] The Ginzberg-Landau coherence length,  $\xi_{GL}$ , differs from the standard counterpart in that it is a measure of the size of the superconducting order parameter, which characterizes the degree of coherence of the superconducting state.[65]  $\xi_{GL}$  represents the length where the magnetic field penetrates the superconductor.[40] For greater lengths, superconductivity is quenched. In the dirty limit, the electron mean free-path scattering length is far less than  $\xi_{GL}$ , and the coherence length is described by  $\xi = (\ell\xi_{GL})^{1/2}$ . Where  $\ell$  is the mean free scattering path in a superconductor.

Further studies turned to doping of the  $\text{H}_3\text{S}$  system with carbon, producing a carbonaceous sulfur hydride (C-S-H) that under 288 K at 267 GPa, could achieve room-temperature superconductivity for the first time.[3] This work would later be retracted due to concerns over the background subtraction of the performed AC susceptibility measurements.[66] These materials achieve superconductivity through their high electron-phonon coupling, allowing

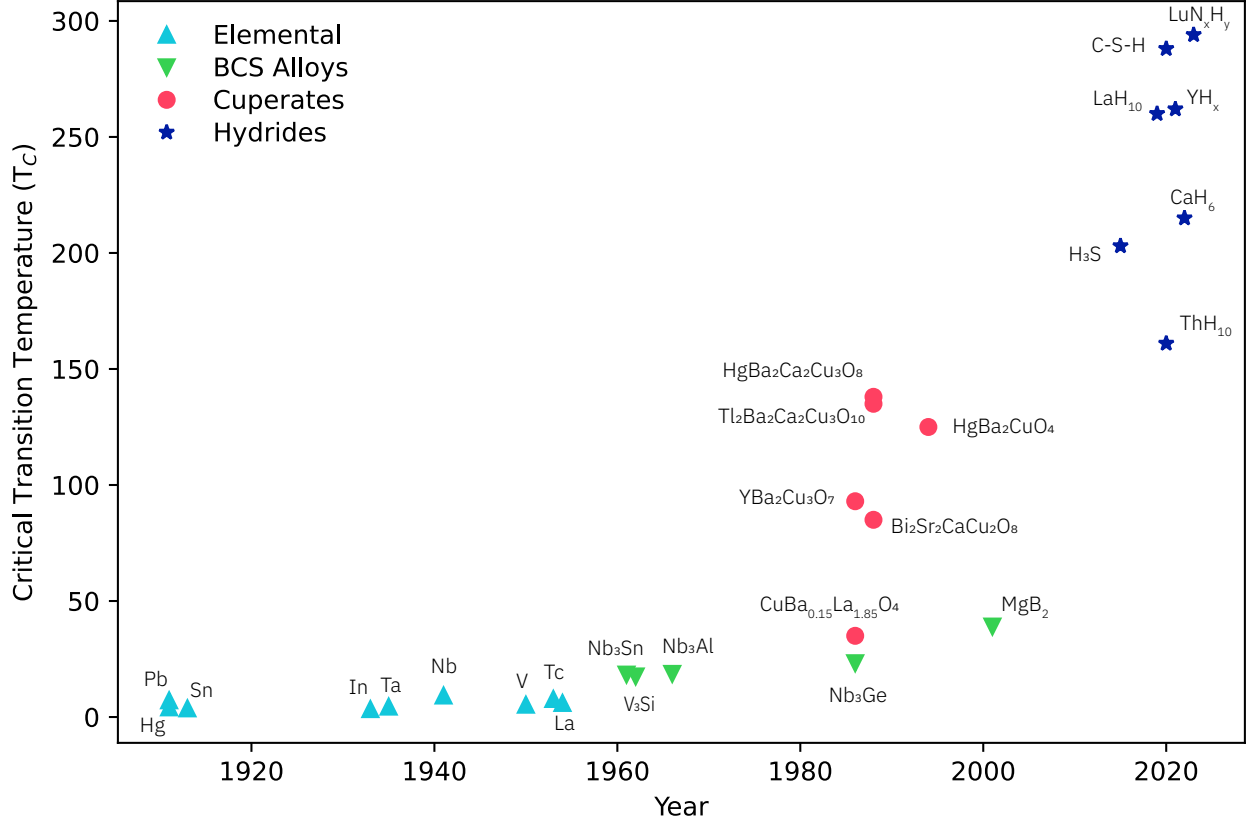


Figure 1.3: A timeline showing when superconductors were discovered and their critical superconducting transition temperature. Included are elemental superconductors, BCS superconducting alloys, cuprates, and hydrides.[3, 4, 5, 6, 10, 63, 70, 71, 72, 73, 74]

for high hydrogen-related density of states near the Fermi surface. The second pathway to superconductivity is through metal hydrides. Binary rare earth metal hydride systems were predicted to be excellent candidates for achieving room temperature superconductivity, with early predictions of both LaH<sub>10</sub> and YH<sub>10</sub> achieving higher  $T_C$ s than 0° C, with well understood, conventional, superconducting mechanisms.[59] Experimental measurements confirmed high  $T_C$ s, but below theoretical predictions with maximum  $T_C$  of 260 K at 188 GPa and 262 K at 182 GPa for LaH<sub>10</sub> and YH<sub>9</sub> respectively.[4, 67] Based on the recent success of binary rare earth hydrides, extension to ternary hydrides has become an exciting field of study. The combination of the previous two materials in (La, Y)H<sub>10</sub> recently achieved a  $T_C$  of 253 K at 183 GPa.[68, 69]

These materials are still pushing the boundaries of what is possible, and require characterization of their properties to help design next-generation superconducting materials, and to better understand their underlying mechanisms and properties. Understanding the most critical behavior of the superconducting hydrogen sublattice within these systems experimentally proves challenging, even at ambient conditions, as it is difficult to characterize hydrogen sublattices under the extreme thermodynamic conditions required for synthesis.[6, 75] Furthermore, X-ray techniques that are very powerful for structural characterization typically struggle with hydrogen materials, as diffraction techniques measure electron density and hydrogen has a very low X-ray scattering cross-section.[76] This, coupled with the non-hydrostatic strain imposed by the anvils necessary to achieve high pressures, results in datasets with insufficient information to establish reliable structures or compositions.

While X-ray diffraction (XRD) is still an excellent tool for determining the cationic sublattice, XRD struggles even at ambient conditions to accurately determine hydrogen sites. A change in coordination number causing an accompanied change in compressibility is a valid expectation. Unfortunately, previous studies have shown that calculated compressibilities have been overestimated, and true coordination numbers differed from what was expected using compressibility, as in  $\text{Sn}_3\text{N}_4$ , which was experimentally determined using X-ray absorption measurements.[77] Where other techniques are not viable due to limitations imposed by the diamond anvil cell, XRD is still a powerful technique to determine heavy cationic sublattices. The result of these experimental challenges is that most of what is known of the hydride sublattice is known through theoretical studies.

The most common approach to determining the stoichiometry of hydrides is to compare experimentally determined compressibilities to calculated counterparts.[78] However, this approach is problematic due to how hydrides are theoretically calculated. Density functional theory (DFT) is a powerful tool based on quantum mechanics for the modeling of electronic densities to allow for the determination of various properties.[79, 80, 81, 82, 83, 84] DFT does not account for temperature effects and the quantum nature of hydrogen which means



that there can be strong anharmonic effects, complicating simulations. All of these factors contribute to the result that DFT often will misjudge the volume for a given pressure of a hydride material. Still, these relations are used to assign stoichiometries to a material. All of these factors result in the thesis statement that we, as the high-pressure community, need to both diversify and advance the metrology necessary to study these low-Z sublattices.

In response to these difficulties, we explore the use of applying techniques established under ambient conditions to the diamond-anvil cell with the intent of probing the structure of low-Z materials. In this dissertation, a selection of works that highlight the importance of the behavior of low-Z species to the bulk properties of a material, the difficulties in their characterization, and extend techniques common in other fields to in situ measurements inside the diamond anvil cell at pressures relevant to the synthesis of super-stoichiometric hydride materials are presented. X-ray spectroscopic techniques are powerful probes for materials with low-Z sublattices under extreme conditions. High-Z species often have edge energies that are able to be probed at X-ray facilities, such as the Advanced Photon Source (APS) at Argonne National Lab, the European Synchrotron Radiation Facility (ESRF), or European X-ray Free Electron Laser (EuXFEL). Due to the diamond anvil being transparent in the hard X-ray regime, many X-ray experiments can be performed axially through the diamond anvil. Though X-ray absorption spectroscopy is already an established technique at high pressure, the metrological constraints necessary for measurement traditionally limit measurements beyond 1.5 Mbar. We expand the use of X-ray spectroscopy into the pressure, chemical, and metrological environments necessary for both the synthesis and characterization of high-stoichiometric hydride materials.

In this dissertation, three studies on different low-Z materials. In the first study[7], I present our work on  $\text{GeO}_2$ , a binary oxide that demonstrates how the low-Z oxide sublattice can impact the bulk behavior of a material. Further, using X-ray spectroscopy, we demonstrate the ability to observe the behavior of a low-Z sublattice when diffraction cannot. In the second study [8], we explore changes in the electronic and structural properties through

variations of carbon content of a carbonaceous sulfur hydride reported to achieve room temperature superconductivity under extreme conditions (288 K at 267 GPa). The effects of the variation of carbon content on structure and superconductivity in C-S-H was studied in the previously unmeasured sub-megabar pressure regime, displaying, at the time of finding, a record  $T_C$  below a megabar through electron transport measurements. The carbon content was quantified qualitatively through the relative intensities of C-H to H-S-H stretching modes using Raman spectroscopy. In the third study, we examine the clathrate-like yttrium hydride system using X-ray spectroscopy. We are able to show the first quantitative measurements of XES at megabar pressures on a hydride material. We show, through direct measurements of the VTC X-ray emissions, differentiation of whole integer stoichiometry from direct measurements of hydrides to be feasible, resolving  $\text{YH}_2$ ,  $\text{YH}_3$ , and  $\text{YH}_4$  through the megabar regime resulting in excellent agreement with theoretical OCEAN calculations.[85]

## 1.1 OUTLINE OF THIS WORK

### 1.1.1 The prevalence of pre-transition disordering in the rutile to $\text{CaCl}_2$ phase transition of $\text{GeO}_2$

The ability to tailor a material's electronic properties using density-driven disordering has emerged as a powerful route to materials design. The observation of anomalous structural and electronic behavior in the rutile to  $\text{CaCl}_2$  phase transition in  $\text{SnO}_2$  led to the prediction that such behavior is inherent to all oxides experiencing such a phase transition sequence.[86] Here, the ultra-wideband gap semiconductor  $\text{GeO}_2$  is confirmed to exhibit anomalous behavior during the rutile to  $\text{CaCl}_2$  phase transition. A phase pure rutile  $\text{GeO}_2$  sample synthesized under high-pressure, high-temperature conditions is probed using synchrotron diffraction and X-ray and optical spectroscopy under high-pressure conditions. Density functional theory calculations show that the enthalpic barrier to displacing oxygen along the  $B_{1g}$  librational

mode decreases with pressure leading up to the rutile to  $\text{CaCl}_2$  phase transition. The band structure of the distorted state shows that such oxygen displacements form small polarons. More broadly, this work displays how small effects in a low- $Z$  cationic sublattice result in dramatic changes in bulk properties. This work further validated techniques necessary to characterize future works on stable compounds inert under atmospheric conditions. The metrological advances developed through this work would be applicable to future works on exciting hydride systems. This work has been published in Physical Review B.[7]

### 1.1.2 Carbon content drives high-temperature superconductivity in a carbonaceous sulfur hydride below 100 GPa

We report a previously unobserved superconducting state of the photosynthesized carbonaceous sulfur hydride (C-S-H) system with a maximum  $T_C$  of 191(1) K below 100 GPa. The properties of C-S-H are dependent on carbon content, and X-ray diffraction along with simulation reveals the system retains molecular-like packing up to 100 GPa. Using single crystal X-ray diffraction (SC-XRD), we observed significant volume discrepancies of up to 2.9% between crystals in the same sample chamber, an unexpected behavior for high-pressure experiments in this pressure regime. The phase progression of C-S-H was confirmed up to 100 GPa of  $I4/mcm$  to  $C2/c$  to  $I4/mcm$ , in agreement with previous studies.[87] However, in carbon-rich samples, the monoclinic  $C2/c$  phase was bypassed, implying that carbon content can impact the phase progression of C-S-H. This work was published in Chemical Communications.[8]

### 1.1.3 Structural determination of clathrate-like yttrium hydrides under extreme conditions

The pathway to high temperature superconductivity, approaching room temperature, has been demonstrated by multiple hydrogen-metal alloys under high-pressure conditions. Despite this, direct measurements of the hydrogen sublattice in a diamond anvil cell (DAC) have been elusive, even at near ambient pressures. In this work we perform X-ray diffraction (XRD) and X-ray emission spectroscopy (XES) up to 200 GPa and measure coordination in the clathrate-like yttrium hydride system. We find that at megabar pressures XES remains a viable candidate to discern stoichiometries through observation of shifts of valence-to-core (VTC) transitions.  $\text{YH}_2$ ,  $\text{YH}_3$ , and  $\text{YH}_4$  are able to be clearly distinguished from experimental XES measurements in this work.

Currently, more calculations are being run to confirm behavior at lower pressures and for higher, unobserved stoichiometries. Initial results are very promising, and we are currently in the process of compiling the manuscript for publication.

## 1.2 OVERVIEW OF EMPLOYED METHODS

### 1.2.1 Simple metal models and metallic bonding

The most simple model for a metal is the Drude model, which more refined models build upon. [36] The Drude model is a semi-classical model due to the way electrons are treated. In the Drude model, nuclei and core electrons are treated as stationary charged spheres, and valence electrons are treated as being free, traveling through a lattice in accordance with the kinetic theory of gases. Like in kinetic theory, an electron behaves as a particle in a gas and travels in a straight line until they collide with a nucleus, where collision time is negligible. The Drude model assumes that  $e^- - e^-$  and  $e^- - \text{ion}$  interactions between collisions are ignored unless an external field is applied. If a field is applied they react in accordance

with Newtonian mechanics but do not create new fields. Ignoring  $e^- - e^-$  interactions is called the independent electron approximation and ignoring  $e^- - \text{ion}$  interactions is the free electron approximation. In the Drude model, the mean time between collisions is represented by  $\tau$  and is independent of electron velocity or position. This is called the relaxation time approximation. These approximations result in the behavior that electrons can only achieve thermal equilibrium through collisions as the free electron gas does not interact with ions in this model. This results in thermal properties, such as the specific heat, being poorly modeled by the Drude model.

The Drude-Sommerfeld model considers the quantum nature of electrons and marries the Drude model to Fermi-Dirac statistics instead of Maxwell-Boltzmann.[36, 37] In the Sommerfeld model electrons still obey the relaxation time and independent electron approximations, but ions impart a periodic potential as well as a boundary condition to the electronic wave function. Rather than classical collisions, ions interact by imposing a periodic boundary condition on core electrons to remain within some volume  $V$  defined by a length  $L$ , such that  $V = L^3$ . To mathematically impose this, we will use the stipulation that any coordinate plus some length  $L$ , will be equal to the initial coordinate position. Electrons are Fermions, and as such, must obey the Pauli exclusion principle limiting an electron to occupy only a single electron level. This is why it is called a free Fermi gas. Here the electron can be described with a quantum interpretation using a free electron wave function  $\psi(\mathbf{r})$ . In the Sommerfeld model, both the free electron and independent electron approximations apply resulting in no interactions and the time-independent Schrodinger equation takes the familiar following form.

$$-\frac{\hbar^2}{2m} \left( \frac{\partial^2}{\partial x^2} + \frac{\partial^2}{\partial y^2} + \frac{\partial^2}{\partial z^2} \right) \psi(\mathbf{r}) = E\psi(\mathbf{r}) \quad (1.14)$$

where the wave function takes on the plane wave form of  $\psi(\mathbf{r}) = e^{i\mathbf{k}\cdot\mathbf{r}}$ . Here  $\mathbf{r}$  is the position vector and  $k$  is the wave vector. Recalling the periodic boundary condition that was imposed,

$e^{ik_r L}=1$ . This constrains  $k$  to discrete values.

$$k_r = \frac{2\pi n_r}{L} \quad (1.15)$$

Where  $n_r$  are integer values. Here, in three dimensions, we can produce a wave vector in each Cartesian coordinate to define a k-space where coordinates are defined by integral multiples of  $2\pi/L$ . Defining with 3 Cartesian components of  $k_r$ , the number of allowed k-space density  $N_{k-SD}$ , or the k-values per unit volume in k-space,  $\Omega$ , can be defined as follows.

$$N_{k-SD} = \left(\frac{L}{2\pi}\right)^3 = \frac{V}{8\pi^3} \quad (1.16)$$

One electron levels are defined by the wave vector and the projection of the electron spin along an axis. The projection can take the value  $\pm\hbar/2$  for either a spin up or down electron allowing two states per wave vector and remaining congruent with the Pauli exclusion principle. For a very large number of electrons  $N$ , being placed into one-electron states, we can build a ground state. The occupied k-values can be estimated as a sphere with radius  $k_F$  that we will call the Fermi wave vector, described by the following statement.

$$\Omega_F = \frac{4\pi k_F^3}{3} \quad (1.17)$$

This sphere is called the Fermi sphere. The surface of the Fermi sphere is called the Fermi surface and divides the occupied states from the unoccupied states. The momentum of the highest occupied electron in this model can be described by  $p_F = \hbar k_F$ , where the  $p_F$  is the Fermi momentum. The kinetic energy of this electron is called the Fermi energy and is described as follows.

$$\epsilon_F = \frac{\hbar^2 k_F^2}{2m} \quad (1.18)$$

This model helps correct the classical dynamics approach to the electron behavior of the Darude model.

Both models help describe how metals bond due to delocalized electrons. In metallic bonding, strong attraction is achieved through ions from sharing of free, delocalized electrons across the Fermi surface. The consequence of this interaction is that these shared electrons move freely through metal creating an electrostatic force with the ion cores. The behavior of these free electrons across the metal helps explain many common properties of metals such as good thermal and electrical conductivity and malleability.

### 1.2.2 The diamond anvil cell

Modern high-pressure experiments are broadly separated into static and dynamic condition experiments. Dynamic experiments are typically achieved using high-energy lasers to rapidly shock samples up to terapascal pressures.[88, 89, 90] At large facilities, such as the National Ignition Facility (NIF), these energies can be as high as 2 MJ. This process is typically destructive, and subsequent observations on the same sample are uncommon. Furthermore, due to the process, shock occurs along the thermodynamic pathway known as the Hugoniot which constrains the pressure and temperature pathway during an experiment. Static condition experiments are popular when any of the mentioned constraints inhibit an experiment. Static compression experiments are most commonly carried out with either large-volume presses or the diamond anvil cell (DAC). As all works in this dissertation were done using the DAC, only this technique will be discussed further.

The DAC leverages the simple principle that pressure is a force applied over an area. As such, if a moderate force is applied to a very small area, the pressures achievable are quite large. This constrains samples to be small, typically no more than a few hundred micrometers in any dimension. These samples are contained within a gasket material, most commonly stainless steel if high pressures and reactivity are not key concerns, or rhenium if high pressures and a well-characterized gasket are important. The typical range of a DAC experiment is between the pressure experienced at the bottom of the Mariana trench (0.1

GPa) to the core of the earth (330 GPa). Modern metrology has recently extended this range into the terapascal regime.[91] Unfortunately, these experiments can only be performed on exceptionally hard and incompressible materials due to the extreme conditions experienced by the sample leading to thinning, eventually leading to anvil failure. Further, constraints are imposed by the aperture geometry of the DAC limiting the axial solid angle aperture for diffraction and fluorescence collection for various techniques.

Despite these many shortcomings, the DAC remains ubiquitous, due to the capabilities of holding samples under pressure nearly indefinitely and the flexibility of techniques available.[7, 8, 92, 93, 94, 95] The use of diamond anvils is the greatest asset of the DAC, resulting in an anvil that is light, low-Z, ultra-hard, incompressible, and has high thermal conductivity and transparency in nearly the entire electromagnetic range, except portions of the UV. Transparency in the X-ray regime coupled with low-Z anvils allows the DAC to be used effectively with both X-ray diffraction and spectroscopy applications. Optical transparency in the IR allows for laser heating and transparency in the visible allows for optical spectroscopy.

To achieve high pressures, a well-machined DAC is required. The tolerances of the side walls of the piston-cylinder interface should be less than 20 microns to consistently achieve megabar conditions. Increasing the surface area along this interface will further increase stability. Using a coating along this interface can further decrease the tolerances while also decreasing the friction coefficient along the compression axis. This, ideally, translates to smoother compression.[96]

### 1.2.3 High-temperature laser heating

High temperatures, typically on the order of a few thousand Kelvin, were achieved through the application of neodymium doped yttrium aluminum garnet (Nd:YAG) or ytterbium lithium fluoride (Nd:YLF) lasers. These near 1  $\mu\text{m}$  lasers typically have short penetration



depths due to the mechanism of coupling to metallic or semiconducting samples. In materials with plasma frequency greater than 300 THz (the frequency associated with 1  $\mu\text{m}$  assuming the speed of light is equal to  $3 \times 10^8$  m/s), incident light couples to surface plasmons.[37] This in turn results in difficulties heating bulk material due to the laser having frequency lower than the plasma frequency resulting in quick attenuation of the light near the surface. This results in typical penetration depths on the order of 10s of nanometers.[97]

Heating insulators are typically impractical at 1  $\mu\text{m}$  due to poor coupling. Fortunately, heating is still possible by using 10  $\mu\text{m}$   $\text{CO}_2$  lasers.[98, 99] Unlike YAG lasers that couple to the surface plasmons, 10 $\mu\text{m}$  light can couple to phonons, allowing for bulk heating in a sample.

#### 1.2.4 X-ray diffraction

X-ray diffraction (XRD) is among the most used techniques in high-pressure physics. A unit cell is the smallest repeating unit that can be used to reproduce a crystal.[36, 37] Bragg diffraction occurs when radiation with a wavelength comparable to the atomic distance, is scattered by the electronic density of a crystal.[100] The following relation, Bragg's law, relates the diffracted light to the interatomic spacings.[101]

$$n\lambda = 2d\sin\theta \tag{1.19}$$

where  $n$  is the diffraction order,  $\lambda$  is the wavelength of the incident X-ray,  $d$  is the atomic spacing, and  $\theta$  is the angle between the incoming X-ray and the plane.[36, 37] A simple schematic showing Bragg's law can be found in Fig. 1.4. This relatively simple model ignores diffraction intensity, which can be described through the differential cross-section ( $d\sigma/d\Omega$ ). The differential cross-section is equal to the number of X-rays scattered per second into a solid angle  $d\Omega$  divided by the incident flux times some portion of the solid angle  $d\Omega$ .[100]

This can be expressed as follows.

$$\frac{d\sigma}{d\Omega} = r_0^2 P |F(Q)|^2 N \nu_c^* \delta(Q - G) \quad (1.20)$$

Where  $r_0$  is the Thompson scattering length,  $P$  is the polarization of the incident radiation,  $|F(Q)|$  is the structure factor of the unit cell,  $N$  is the number of unit cells,  $\nu_c^*$  is the volume of the unit cell in reciprocal space, and  $Q$  is the scattering vector  $k_{in} - k_{diff}$  and  $G$  is the reciprocal lattice vector  $G = h\hat{a} + k\hat{b} + l\hat{c}$ . The coefficients of the reciprocal lattice vector  $hkl$  are called Miller indices and describe the planes on which the atoms are regularly arranged.

The structure factor defines electron density in the unit cell and can be defined for a unit cell as the following statement

$$F(Q) = \sum_j f_j(Q) e^{iQ \cdot r_j} \quad (1.21)$$

where  $r_j$  is the position of an atom with respect to any one lattice site,  $f_j(Q)$  is the atomic form factor and takes the following form.

$$f_j(Q) = \int \rho(r_j) e^{iQ \cdot r_j} dr + f' + i f'' \quad (1.22)$$

Where  $\rho$  describes the electronic density of the atom and  $f'$  and  $f''$  are dispersion correction terms. When  $Q$  is equal to  $G$ , the Laue condition is met and the delta function returns 1. Many light sources can optimize polarization to maximize this term for diffraction. XRD describes the long-range order of a system and is sensitive to the symmetry behaviors of a crystalline sample. Atoms have diffraction power proportional to the square of their atomic number ( $Z$ ), leading to ease when determining high- $Z$  materials, but struggle when determining high- $Z$ /low- $Z$  binary materials, such as hydrides, as the contribution to the area of the diffraction peaks of the light cationic species will be small.[5, 8, 87]

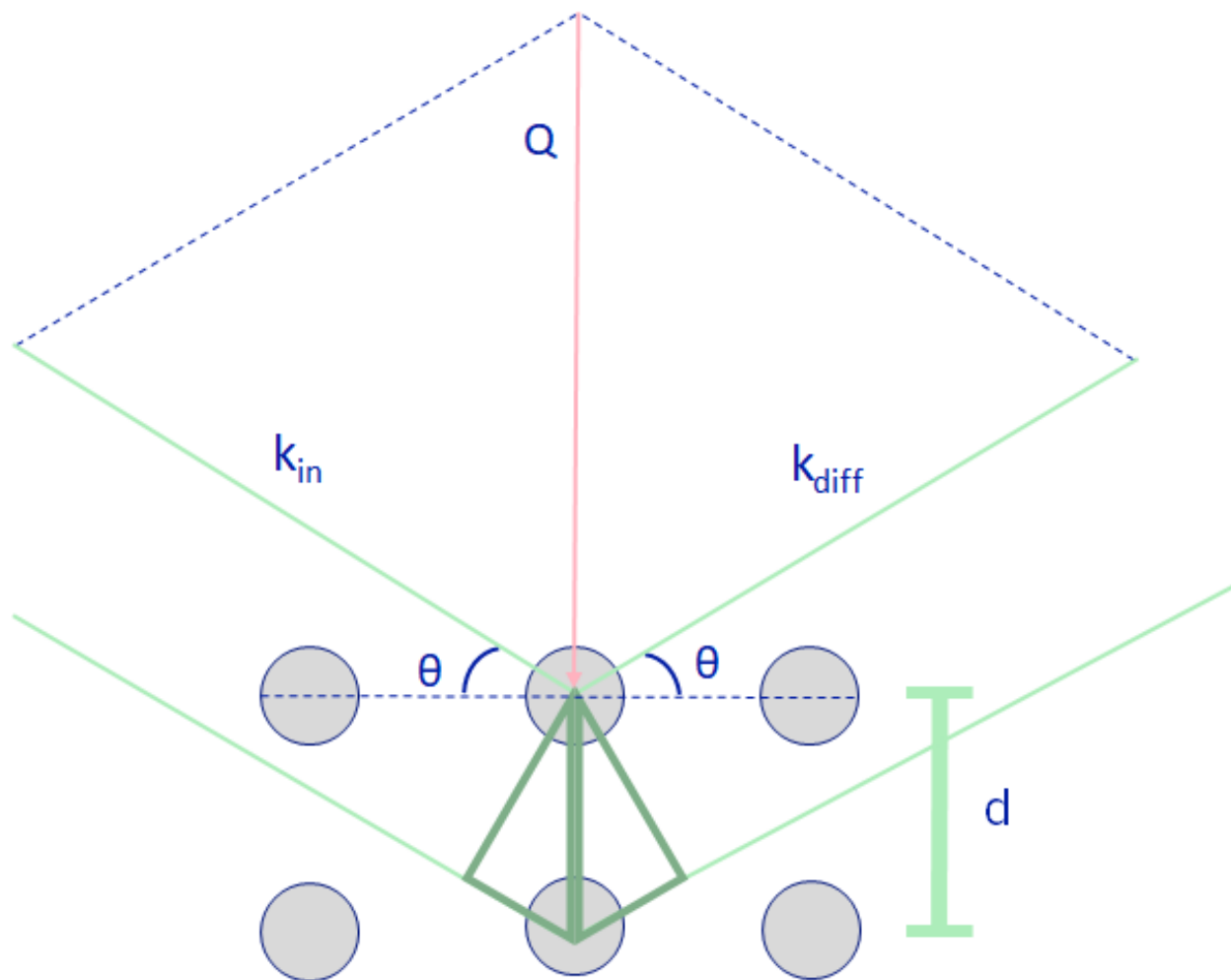


Figure 1.4: A graphic showing a representation of X-ray diffraction through Bragg's Law. Here an incident X-ray  $k_{in}$  is diffracted at some angle  $\theta$  and the resulting diffracted X-ray is  $k_{diff}$ . The difference between these  $k_{in}$  and  $k_{diff}$  results in the scattering vector  $Q$ . When  $Q$  is equal to the reciprocal lattice vector  $G$  of a crystal, diffraction can occur.[36, 37, 100]

### 1.2.5 X-ray absorption spectroscopy (XAS)

In the case of a high-Z/low-Z material, such as rare-earth hydrides, where the rare-earth species have a much higher associated electronic density due to having a higher atomic number than the hydrogen, XRD has difficulties resolving the lighter sublattice. Compared to XRD, X-ray spectroscopic methods are favorable probes for investigating the behavior of light species under extreme conditions. The sensitivity to the local environment of spectroscopic techniques allows for information about the low-Z species, even if the low-Z species would typically be a poor X-ray scatterer. Consequently, if a high-Z sublattice is well characterized crystallographically, X-ray spectroscopy can be a favorable technique to determine its local coordination.

The general probability of a spectroscopic transition occurring per unit time can be described by Fermi's golden rule. Fermi's golden rule states that the transition probability per unit time is equal to the probability of that transition occurring times the density of states at the final state.[100] Fermi's Golden rule to the first order is presented here, though higher orders can be used as well, such as the second order Fermi's golden rule for Raman spectroscopy.

$$P \propto |\langle \psi_f | \hat{O} | \psi_i \rangle|^2 \rho(\epsilon_f) \quad (1.23)$$

Where  $\hat{O}$  is the perturbation operator that describes the transition from initial state  $\psi_i$  to final state  $\psi_f$  and the  $\rho(\epsilon_f)$  is the density of states of the final state of the transition, typically the dipole operator. This described result can be used to predict the probability of observing a spectroscopic transition.

The Franck-Condon principle states that an electronic transition is more likely to occur if there is strong overlap of the nuclear vibrational wave function.[102, 103, 104] The results is that the spectroscopic transition made is not always to the lowest energy state. A visualization tool can be seen in Fig 1.5.

This is due to the time scale of electrons being on the order of hundreds of attoseconds

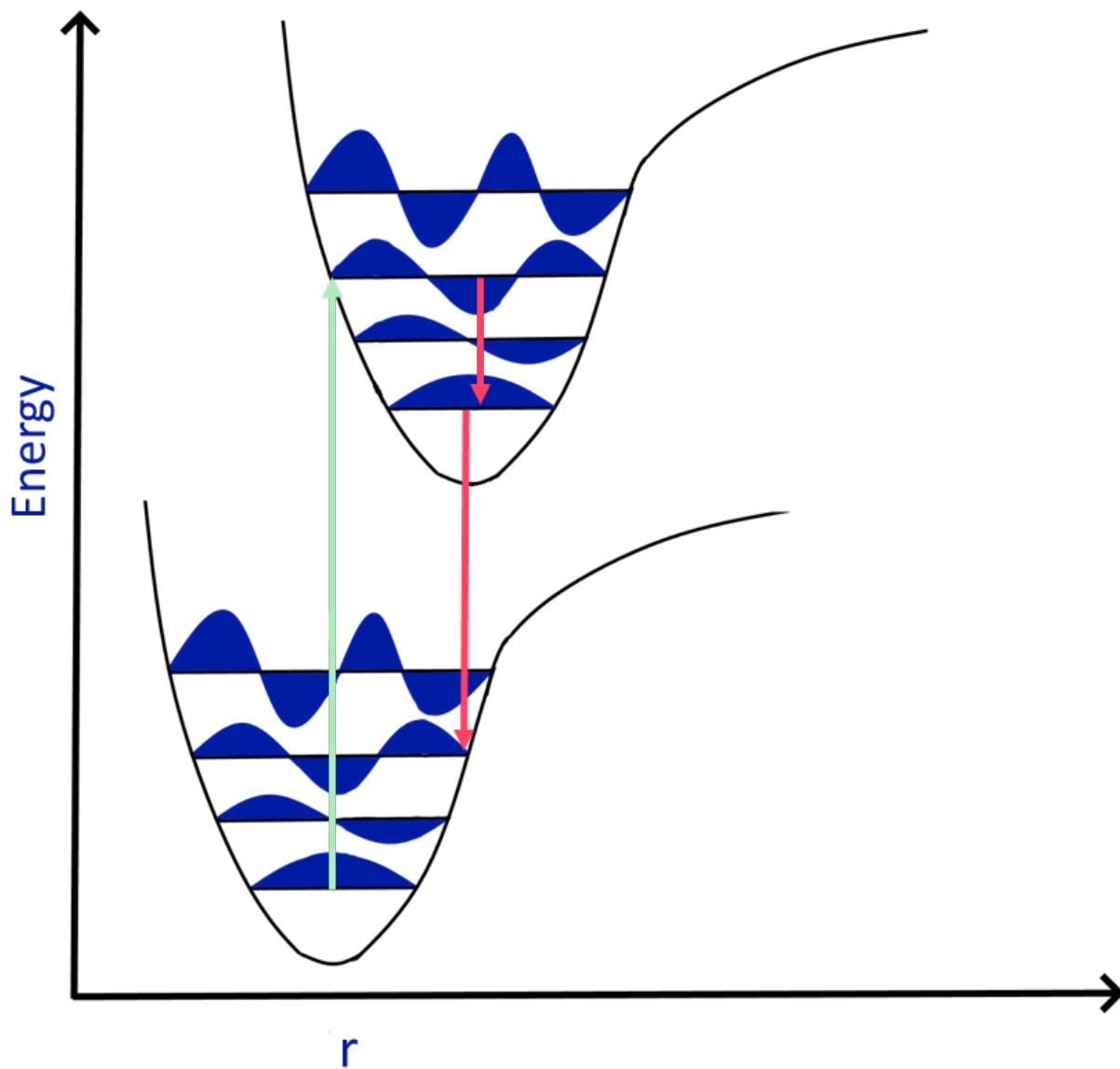


Figure 1.5: A graphic showing the Franck-Condon principle. In this representation, a transition occurs from a ground state into a higher energy state due to the stronger overlap of the nuclear wave function. The fluorescence occurs with the same principle and a relaxation into a  $\nu=2$  state occurs instead of a relaxation into the ground state.[102, 103, 105]

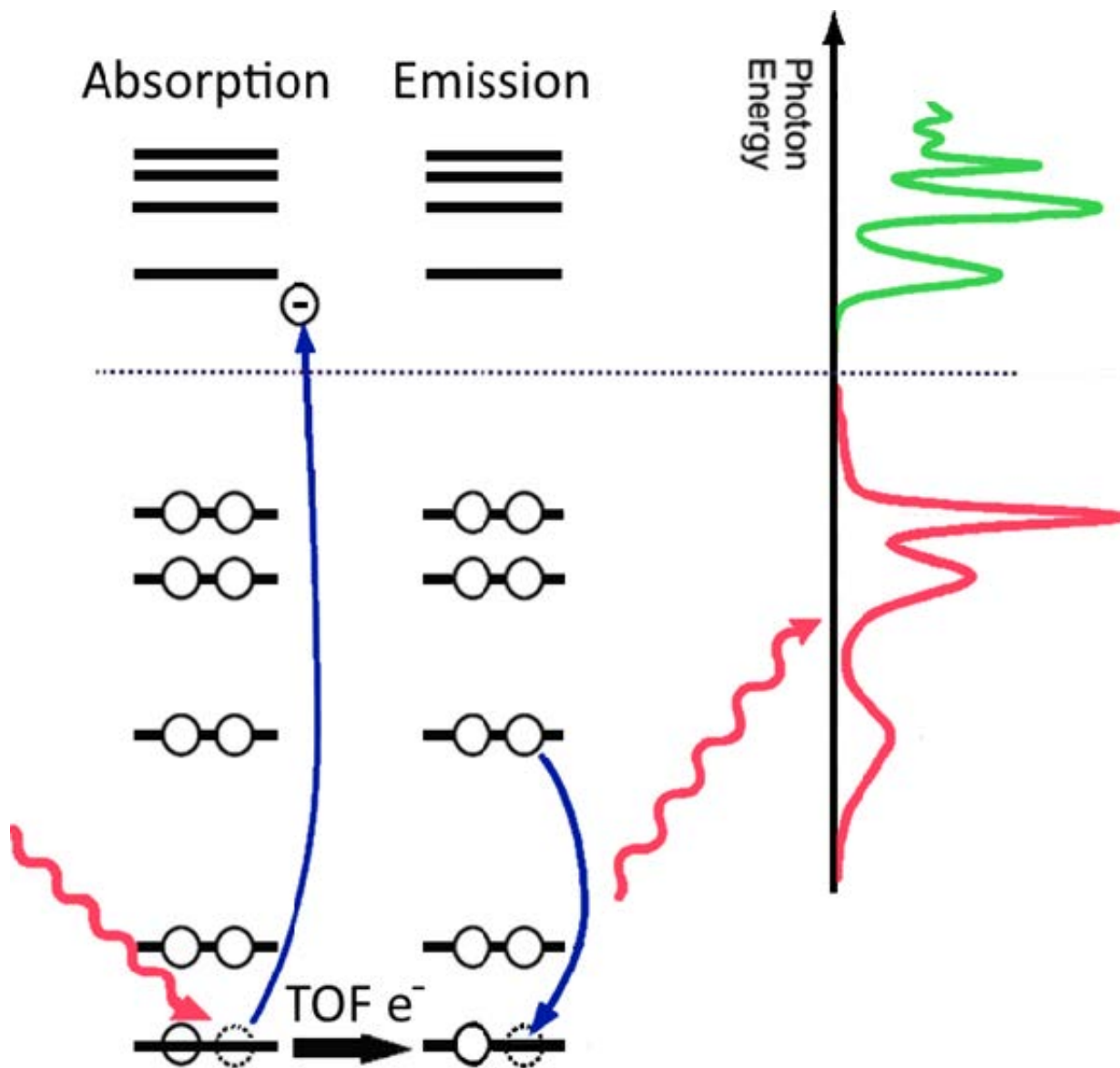


Figure 1.6: A showing the generic process of both XAS (left) and XES (right) techniques.[107]

and the time scale of phonons being on the time scale of hundreds of femtoseconds. Therefore, electrons move a factor of  $10^3$  times faster resulting in the nucleus being functionally stationary relative to the time scale of electronic excitation. This principle is similar to the Born-Oppenheimer approximation, where nuclei are modeled as stationary relative to electrons owing to them being more massive.[106]

X-ray absorption spectroscopy is often described as a one-photon process in which a

photon is tuned to the energy necessary to excite an electron from a core state to the lowest unoccupied orbital, or beyond into the continuum.[100, 108, 109] In Fig. 1.6 the process for both XAS and XES measurements are shown as a visual aid. These measurements are often done by scanning across energy at a synchrotron with a monochromator and using gas ion chambers where the negative log of the ratio of the reference chamber to the detection chamber shows the absorbance spectra. Through this process, three important features should be highlighted, the first is the white line. The white line is the absorption described above, in which a photon is absorbed to the first conduction state. It is called a K-edge if this excitation comes from a 1s state, an L-edge if from a 2s or 2p state, an M-edge if from a 3s, 3p, or 3d state, and so on. For high-pressure experiments, it is common to tune to a K-edge, as many light sources optimized for high-pressure physics are optimized to hard X-ray allowing for probing of 3d to 4d. Lighter species can be probed still, difficulties often arise from constraints of the DAC and atmosphere.[110, 111]

The next region is called the X-ray absorption near-edge spectroscopy (XANES) region. The XANES region includes pre-edge features, the white line itself, and usually up to 100-150 eV after the white line. Pre-transition features occur from transitions from molecular orbitals from scatter-ligand interactions or other features such as d to d dipole forbidden interactions. This leads to XANES being a powerful tool for determining the electronic behavior of a species. These can be very insightful features, but nearly always require theoretical calculations, such as the OCEAN code[85], that solves the Bethe-Salpeter equation.

The final region is everything beyond the XANES region which is called the extended X-ray absorption fine structure region (EXAFS) region. In this region, we observe how an electron interacts with its nearest neighbors after being ejected into the continuum as a spherical wave. The interference patterns produced from this wave with neighbors results in EXAFS, unlike XRD, being sensitive to the local structure and coordination of a material. As a consequence of EXAFS occurring after an electron is ejected into the continuum, EXAFS does not probe the unoccupied states, leading EXAFS to be a structural probe, rather than

an electronic probe.

While quite powerful, raw EXAFS spectra are rarely interpreted in the energy space in which they are acquired, but rather in real space in units of length. To make this transition the EXAFS spectra are first converted into momentum space, which is commonly called  $k$  space. The semi-classical transformation to  $k$  space can be derived rather simply by combining statements for photon momentum and kinetic energy.

$$p = \hbar k \tag{1.24}$$

$$T = \frac{p^2}{2m_e} \tag{1.25}$$

Where  $p$  is the momentum of a photon,  $k$  is the wave vector with units of inverse length,  $m_e$  is the mass of an electron, and  $\hbar$  is Planck's constant divided by  $2\pi$ .

Substituting into the kinetic energy equation and solving for  $k$  we will be left simply with a statement for  $k$ .

$$k = \frac{\sqrt{2m_e T}}{\hbar} \tag{1.26}$$

It is common to assume that the kinetic energy is equal to the energy of the incident photon  $E$  minus the energy required to eject the electron from the absorbing atom  $E_0$ , which another substitution results in the commonly used statement to convert from  $E$  to  $k$ .

$$T = E - E_0 \tag{1.27}$$

$$k = \frac{\sqrt{2m_e(E - E_0)}}{\hbar} \tag{1.28}$$

So far all math performed has been algebraic, but the transformation from  $k$  space to real space will require some calculus in the form of a Fourier transform. A generalized Fourier



transform to convert from  $k$  space to  $r$  space takes the form of the following equation.

$$f(r) = \int_a^b f(k)e^{-2\pi ikr} dk \quad (1.29)$$

Where  $r$  is the distance from the scatterer and  $a$  and  $b$  are the window in which the transform is performed.

### 1.2.6 X-ray Emission Spectroscopy (XES)

X-ray emission spectroscopy (XES) is similar to XAS in that it is an energy-specific technique, but differs in both how it's performed and what this technique probes. In XES, light with energy sufficient to vacate a core state is introduced to the sample to eject electrons from the targeted species, into an excited state. Then after the excited electron relaxes back into the core state, it releases a photon of the energy equal to difference between the excited state and the core state. As such, this is sometimes commonly called a two photon process. A diagram of this process can be found in Fig. 1.6. This measured photon, unlike XAS that probes unoccupied states, tells us about the occupied states.[100, 112, 113]

Siegbahn notation is the most common naming convention for X-ray emission transitions despite having shortcomings.[114] In Siegbahn notation, an emission that occurs between a  $2p_{3/2}$  state to a  $1s$  state would be represented by the symbol  $K\alpha_1$ . This is because the first letter signifies where the transition terminates, so the letter  $K$  implies transitions that relax into the  $1s$  state. The alpha implies the transition occurs from an  $n + 1$  quantum number; in our case, in a  $K$  transition, alpha corresponds to an  $n=2$  state, in this case, a  $2p$  state, while a  $\beta$  transition should correspond to an  $n=3$  state, either a  $3p$  or  $3d$  transition. The subscript is chosen for historical reasons in that it is the most intense transition, therefore given the subscript 1,3 but is now somewhat arbitrary.

The International Union of Pure and Applied Chemistry (IUPAC) created a much more descriptive and useful notation that has confoundingly, not experienced widespread adoption,

Table 1.1: A table comparing Siegbahn and IUPAC X-ray transition notation for equivalent transitions.

Initial state	Final state	Siegbahn	IUPAC
K	L <sub>3</sub>	K $\alpha_1$	K-L <sub>3</sub>
K	L <sub>2</sub>	K $\alpha_2$	K-L <sub>2</sub>
K	L <sub>1</sub>	K $\alpha_3$	K-L <sub>1</sub>
K	M <sub>3</sub>	K $\beta_1$	K-M <sub>3</sub>
K	N <sub>2,3</sub>	K $\beta_2$	K-N <sub>2,3</sub>
K	M <sub>2</sub>	K $\beta_3$	K-M <sub>2</sub>
K	N <sub>4,5</sub>	K $\beta_4$	K-N <sub>4,5</sub>
K	M <sub>4,5</sub>	K $\beta_5$	K-M <sub>4,5</sub>
L <sub>3</sub>	M <sub>5</sub>	L $\alpha_1$	L <sub>3</sub> -M <sub>5</sub>
L <sub>3</sub>	M <sub>4</sub>	L $\alpha_2$	L <sub>3</sub> -M <sub>4</sub>
L <sub>2</sub>	M <sub>4</sub>	L $\beta_1$	L <sub>2</sub> -M <sub>4</sub>
L <sub>3</sub>	N <sub>4,5</sub>	L $\beta_2$	L <sub>3</sub> -N <sub>4,5</sub>
L <sub>1</sub>	M <sub>3</sub>	L $\beta_3$	L <sub>1</sub> -M <sub>3</sub>
L <sub>1</sub>	M <sub>2</sub>	L $\beta_4$	L <sub>1</sub> -M <sub>2</sub>
L <sub>3</sub>	O <sub>4,5</sub>	L $\beta_5$	L <sub>3</sub> -O <sub>4,5</sub>

but provides a more clear explanation of these transitions.[115] A comparison of transition names between the two systems can be found in Table 2.1.3 In this notation, a state is explained solely by its electronic configuration, with a 1s state simply stated as a K and ascending n states as L, M, N, and so on. A number is assigned based on ascending associated spin state, so a 2s would be labeled L<sub>1</sub>, 2p<sub>1/2</sub> would be an L<sub>2</sub> state a 2p<sub>3/2</sub> would be L<sub>3</sub> state, and so on. For a K $\beta_3$  transition in Siegbahn notation, this would correspond to a K-M<sub>2</sub> transition using IUPAC notation. This is of course a transition from the 3p<sub>1/2</sub> state to the 1s state.

Unfortunately, there are more complications in assigning transitions in compounds as well. Many absorber-ligand transitions in Siegbahn notation are simply given a prime (') to denote a crossover transition, such as a K $\beta''$  that is not assigned directly to an element, however, most of these in IUPAC are grouped into K-V transitions, which are non-descriptive. Unfortunately, these valences to core transitions are very powerful for determining the co-

ordination and bond length of the ligand species. For this work both notations will be presented, as the valences to core  $K\beta''$  (K-V) transition is critical to understand the power of XES in determining the coordination of low- $Z$  sublattices.

## CHAPTER 2

### THE PREVALENCE OF PRE-TRANSITION OF DISORDERING IN THE RUTILE TO $\text{CaCl}_2$ PHASE TRANSITION OF $\text{GeO}_2$

#### 2.1 STATEMENT OF EFFORT AND PERMISSION

This work was peer reviewed and published in Physical Review B.[7] In this work, I performed experiments, analyzed data, and performed the writing for this work. Reproduced with permission from Physical Review: <https://journals.aps.org/copyrightFAQ.html#thesis>

#### 2.2 INTRODUCTION

All group 14 dioxides can adopt a rutile structure, though in the case of  $\text{CO}_2$  it is molecular,[116] and the non-molecular group 14 dioxides can undergo a high-pressure rutile to  $\text{CaCl}_2$  phase transition.[117, 118, 119, 120] For  $\text{SiO}_2$ , Landau theory predicts an important variation in the elastic constants leading to a substantial softening of the shear modulus about the rutile to  $\text{CaCl}_2$  transition which should have a strong influence on  $\text{SiO}_2$ 's sound wave velocity and is of high relevance to interpret seismic reflectors in the earth's mantle.[121, 122] The rutile to  $\text{CaCl}_2$  transition in  $\text{GeO}_2$  has been previously reported to occur at 26 GPa,[117] intermediate between that of  $\text{SiO}_2$  at 55 GPa and  $\text{SnO}_2$  at 15.4 GPa.[118, 117, 86] The milder conditions for phase transformations in  $\text{GeO}_2$  than  $\text{SiO}_2$  has long been exploited by the Earth science community for systematic mineralogical substitution with silicate minerals.[123] This analogy between silicates and germanates has helped to build the mineralogical model of the Earth and constraining the origin of seismological discontinuities in the deep Earth's mantle. For example, the transformation of the spinel structure to post-

spinel in the magnesio-silicate perovskite to identify the boundary between the upper and lower mantle at 660 km depth.[124]

The rutile phase of  $\text{GeO}_2$  has been recently considered for its electronic properties in the burgeoning field of ultra-wide bandgap semiconductors (UWBG).[125] Its 4.680 eV bandgap[126] is in the UV-C region of the electromagnetic spectrum, which is ideal for making solar-blind photodetectors as well as light sources for pathogen inactivation in food and water treatment.[127, 128]  $\text{GeO}_2$  has also received attention as a potential passivator for Ge semiconductor technologies, but high temperature decomposition into GeO has led to complications in the manufacturing process.[129] Thus, Ge based semiconductor devices remain unpopular despite having superior bulk electron and hole mobilities over Si, integral to improving device performance as the physical size of modern transistors are reaching a limit of scaling.[130] Rutile  $\text{GeO}_2$  is also predicted to be ambipolarly dopable through first-principles defect calculations by substituting group 13 cations in Ge sites to serve as an electron acceptor with ionization energies in the 0.45 to 0.5 eV range.[131] Such doping enables p-type conduction through the impurity band, allowing for a tuning of the bandgap and design of application-tailored materials.

Recently, a four-fold increase in conductivity during the rutile-type ( $P4_2/mnm$ ) to  $\text{CaCl}_2$ -type ( $Pnmm$ ) transition was observed in the transparent conducting oxide  $\text{SnO}_2$ . [86] The transition from the rutile to the  $\text{CaCl}_2$  structure is a ferroelastic, second-order phase transition typically accompanied by a continuous volume change, and it can vary in pressure depending on the deviatoric stress and temperature.[132, 121] The rutile to  $\text{CaCl}_2$  phase transition is driven by the softening of the Raman active  $B_{1g}$  octahedral librational mode, which with increased pressure allows for larger energetically accessible octahedral libration angles.[122] The anomalous conductivity observed during the rutile to  $\text{CaCl}_2$  transition in  $\text{SnO}_2$  is best attributed to a disordered, pre-transition state with single atom displacements of the oxygen sub-lattice enabled by a reduced energetic barrier for displacement from the softened  $B_{1g}$  librational mode. The oxygen displacements effectively decrease the band gap

of the material before the transition to the  $\text{CaCl}_2$  phase.[86]

This behavior is predicted to be universal in oxide materials experiencing this phase transition rather than inherent to the chemistry of the charged species in the material. Understanding and controlling this phenomena will allow for a pressure mediated tuning of the optoelectronic properties of materials. Here, we evaluate the universality of the pre-transition disordered state during the rutile to  $\text{CaCl}_2$  phase transition for  $\text{GeO}_2$  via spectroscopic, diffraction, and theoretical methods. We comment on the how the defects affect the electronic properties of a rutile oxide.

## 2.3 METHODS

Samples of rutile  $\text{GeO}_2$  were synthesised in a large-volume press under high-pressure and temperature conditions. Static high-pressure experiments were conducted using custom-designed diamond anvil cells (DAC). Helium was used as the pressure transmitting media (PTM) and pressure was controlled via a membrane for fine pressure resolution. Pressure was determined using the ruby fluorescence scale.[133] Raman spectroscopy experiments were carried out on a home-built design, utilizing Optigrate volume Bragg gratings for low frequency measurements.

X-ray absorption and diffraction measurements were performed at HPCAT (United States, APS, sector 16), and were acquired on the same sample sequentially at each pressure. X-ray diffraction (XRD) was performed axially, ( $\lambda = 0.3738 \text{ \AA}$ ), through the diamond anvil using Boehler-Almax conical design diamonds to allow for a  $70^\circ$  angle aperture. Diffraction data was integrated using *Dioplas* software and Rietveld analysis was performed using *GSAS* software. The calculated absorption length for  $\text{GeO}_2$  was calculated by *Hephaestus* software, and was matched by acquiring X-ray absorption (XAS) measurements radially through the sample chamber by using beryllium as the gasket material. XAS was acquired on the Ge K-edge with energy scanned by 350 eV before the white line of 11.103 keV and 1 keV after

using a bare silicon mirror to tune energy. Raw XAS data was reduced and analyzed using `Demeter` and `FEFF`.<sup>[134, 135]</sup>

XAS spectra were fit using a window of 2.8 to 13.7  $\text{\AA}^{-1}$ , using  $k$  weights of 1, 2, and 0.5 chosen to achieve a better fit.  $S_0^2$  was determined by restraining the value to one and fitting all data, and then fitting only the amplitude reduction factor over all fits simultaneously. All data was then refit using the optimized value in a two shell fit, by fitting all values with the starting guess of  $\Delta R=0$ ,  $\text{MSRD}=0.001$ , and  $\Delta E=0$ . All variables were fit, and then  $\Delta R$  and  $\text{MSRD}$  values were fit for each shell. Finally  $\Delta E$  was refined again.  $\text{MSRD}$  values were restrained to be equal of greater than zero. Both 1 and 2 shell fits were performed.

Ab initio density functional theory (DFT) simulations using VASP (Vienna Ab initio Simulation Package) were used for structural optimizations and to determine the effect of pressure mediated defects.<sup>[79, 80, 81, 82, 83]</sup> The strongly constrained and appropriately normed (SCAN) meta-GGA functional with Grimme's -D3 dispersion correction was used throughout.<sup>[82, 136, 137, 138]</sup> Each simulation used a  $\Gamma$  centered  $k$ -point grid with a  $0.3 \text{\AA}^{-1}$  spacing.<sup>[139]</sup> The tetrahedron method with Blöchl corrections were used to integrate the Brillouin zone due to its high degree of accuracy for non-metals.<sup>[140]</sup> Projector-augmented wave (PAW) PBE pseudo-potentials were utilized for both Ge and O with valence configurations of  $s^2p^2$  and  $s^2p^4$ , respectively.<sup>[141, 142]</sup> Energy and force convergence parameters were set to a difference of  $10^{-10}$  eV and  $10^{-3}$  eV/ $\text{\AA}$ , respectively. Structural optimizations were performed as two sequential optimizations then a final energy evaluation resetting the plane-wave basis set between each step to minimize the effect of Pulay stress. Band structure plots were created by re-determining the bands along the high symmetry points and lines of a simple orthorhombic cell using a fixed, pre-converged charge density. Band structure and density of states plots were made using the `sumo` package.<sup>[143]</sup>

## 2.4 RESULTS AND DISCUSSION

The Landau free-energy potential with respect to the motion of the  $B_{1g}$  librational mode in rutile structures is expected to soften as a function of pressure,[122] thus a defining feature of a group 14 dioxide’s rutile to  $\text{CaCl}_2$  phase transition should be the abrupt hardening of a previously softening  $B_{1g}$  mode while the other vibrational Raman modes harden.[86] Figure 2.1a shows that the central frequency of the  $A_{1g}$  mode exhibits the expected hardening by increasing linearly without any deviations from 1 to 30 GPa. Likewise, the  $B_{1g}$  mode exhibits the expected softening from the onset of compression until a clear hardening is observed by 28.4 GPa. A linear fit to the softening range of the  $B_{1g}$  mode remarks a transition pressure into the  $\text{CaCl}_2$  phase of 27 GPa based on where the deviation from linearity first occurs. DFT optimizations of the rutile and  $\text{CaCl}_2$  structures of  $\text{GeO}_2$  across the same pressure range show the  $\text{CaCl}_2$  phase becoming the enthalpically favorable phase by  $\sim 27$  GPa (Figure 2.1b). According to the optimizations, the transition into the  $\text{CaCl}_2$  structure should be accompanied by a small volume change,  $< 0.2 \text{ \AA}^3$ .

The XRD determined volume-pressure relation for compressed  $\text{GeO}_2$  (Figure 2.2a) roughly follows a  $3^{\text{rd}}$ -order Birch-Murnaghan equation of state (EOS) up to 33.7 GPa. Closer inspection reveals the full data set EOS fit is in very tight agreement with the experimental data until 19.7 GPa, after which noticeable deviations from the fit occur (Figure 2.2a inset). As diffraction was collected in a He PTM, it is unlikely these distortions are due to non-hydrostaticity at these pressure conditions,[144] but are rather the system experiencing pre-transition disordering. By 29.6 GPa the distortions appear to be relieved, indicating the system has transitioned into the  $\text{CaCl}_2$  phase as confirmed by Rietveld analysis of the XRD data. A table containing the Rietveld refined lattices as a function of pressure may be found in Appendix A. The transition into the  $\text{CaCl}_2$  phase is accompanied by a smaller than predicted volume drop of  $\sim 0.03 \text{ \AA}^3$  according to a  $3^{\text{rd}}$ -order Birch-Murnaghan EOS fit of just the undistorted rutile phase (0–19.7 GPa).

Fitting an EOS up until any distortion is observed ( $\leq 19.7$  GPa) and up until the  $\text{CaCl}_2$



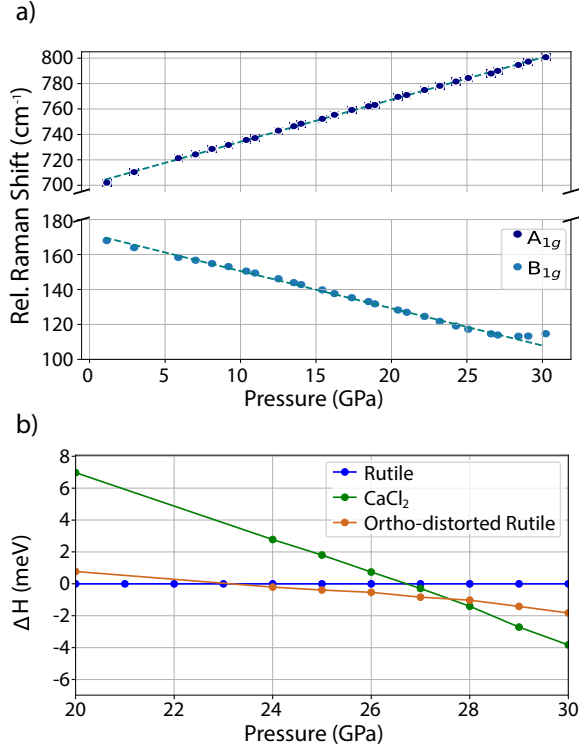


Figure 2.1: (a): The central peak position from fitting the  $A_{1g}$  and  $B_{1g}$  Raman modes against pressure. Linear regressions have been added to both series to help guide the eye, as well as illustrate the  $B_{1g}$  Raman mode’s deviation from linearity around 27 GPa. (b): The enthalpy per unit cell of the rutile,  $\text{CaCl}_2$ , and orthorhombically distorted rutile phase as a function of pressure. All enthalpies are normalized to that of the rutile phase for a given pressure. Credit: GA Smith, UNLV: Raman; Daniel Schacher, UNLV: Theory

phase is confirmed by Rietveld analysis ( $\leq 28.0$  GPa), shows a marked 4% drop in the determined bulk modulus despite the latter fit encapsulating all of the data of the former (Table 2.1). Extending the region of the ‘pristine’ rutile phase out to 21.5 GPa shows only a slight reduction to the fit bulk modulus showing that while disordering may be present by 21.5 GPa it only becomes significant at higher pressures. Oddly, the fit up to 28.0 GPa shows a marked increase in the derivative of the bulk modulus, and a fit over just the ‘disordered’ region (21.5–28.0 GPa) shows an increase in the bulk modulus and a decrease in its derivative. These ambiguities are likely artifacts of the fit and can be alleviated by reducing the fit to that of a 2<sup>nd</sup>-order Birch-Murnaghan equation of state with  $V_0$  fixed to that of the pristine rutile phase ( $\leq 19.7$  GPa). In doing so, the bulk modulus is actually seen to increase

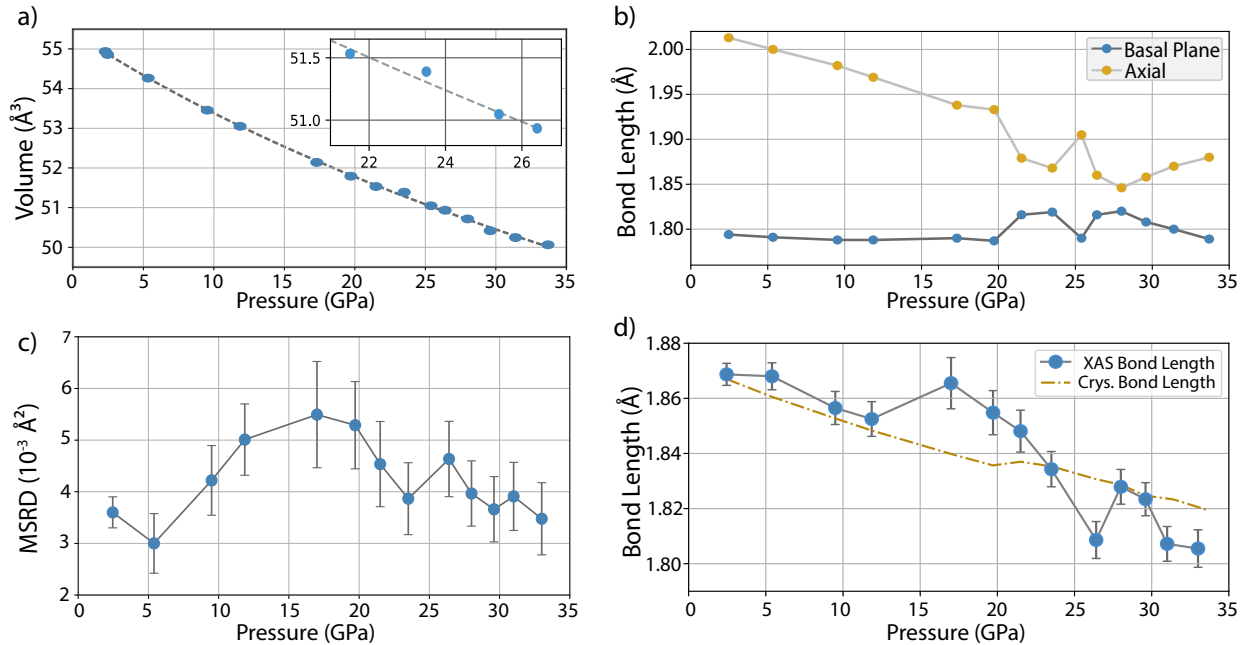


Figure 2.2: A figure containing all X-ray techniques performed on GeO<sub>2</sub> in this study. (a) The pressure-volume response of the sample with a third order Birch-Murnaghan equation of state fit across all data to guide the eye. Note, there are at least two phases described by the data involved in said fit. The inset highlights deviations in the pre-transition disordered state. (b) The average Ge–O bond lengths determined from Rietveld analysis. The error bars of both XRD panels are within the symbol size. (c) The mean squared relative displacement as measured by EXAFS. The strong response between 17 and 27 GPa is attributed to the pre-transition disordered state. (d) The average Ge–O bond length determined from EXAFS with the weighted average crystallographic values. Credit: GA Smith, UNLV: Sample preparation, acquisition and analysis; Ashkan Salmat, UNLV: XRD analysis.

Table 2.1: Birch-Murnaghan equation of state fits across different pressure ranges. The fit was done by fixing  $V_0$  to that of the undistorted rutile (0–19.7 GPa) phase. Credit: GA Smith, UNLV: EoS Analysis

Order	Pressure (GPa)	$V_0$ ( $\text{\AA}^3$ )	$B_0$ (GPa)	$B_0'$
<i>3<sup>rd</sup></i>	0–19.7	55.45	231.83	6.46
	0–21.5	55.45	231.18	6.55
	0–28.0	55.47	221.91	7.95
	0–33.7	55.43	234.78	6.55
	21.5–28.0	55.45 <sup>a</sup>	239.19	6.17
<i>2<sup>nd</sup></i>	0–19.7	55.38	254.77	
	0–21.5	55.38 <sup>a</sup>	255.85	
	0–28.0	55.38 <sup>a</sup>	262.78	
	0–33.7	55.38 <sup>a</sup>	264.37	
	21.5–28.0	55.38 <sup>a</sup>	265.44	

for any set including data above 19.7 GPa (Table 2.1). There is again only a slight difference if only the 21.5 GPa pressure point is included, but a much larger increase for the whole region that is driven by the data in the region between 21.5 and 28.0 GPa. Thus, there is a clear deviation from a crystalline rutile phase after 19.7 GPa, and disordering is present in  $\text{GeO}_2$  by 21.5 GPa persisting at least until the transition into the  $\text{CaCl}_2$  phase.

The difference in scattering intensity for Ge and O is small enough for reliable Rietveld identification of the lighter anion atomic positions, enabling accurate tracking of the Ge–O bond lengths within a coordination octahedra as a function of pressure (Figure 2.2b). The  $\text{GeO}_6$  octahedra are initially irregular with an axial Ge–O distance of 2.01  $\text{\AA}$  and an in basal plane distance of 1.79  $\text{\AA}$  at 2.46 GPa. Only the basal Ge–O interactions are covalent according to covalent radii for Ge (1.20  $\text{\AA}$ ) and O (0.66  $\text{\AA}$ ).<sup>[145]</sup> In line with this, the Ge–O bonds in the basal plane are seen to be very resistant to compression up to 20 GPa, while the axial ones are not. At 19.7 GPa, when the EOS fit for the rutile phase begins to break down, there is a clear indication of atomic disordering in  $\text{GeO}_2$  from the sharp deviation in the pressure response of the bond lengths. As not all the oxygens are displaced in the pre-transition disordered state, the result is an averaged out picture resulting in erratic behavior that increases as defect

concentration grows but diminishes as the defects saturate. This deviation persists until  $\text{GeO}_2$  has accessed the  $\text{CaCl}_2$  phase, wherein the axial bond lengths increase and the basal lengths decrease with pressure. However, the DFT predicted structures state both Ge–O bond lengths should monotonically decrease with increased pressure, so there are residual defects even after the  $\text{CaCl}_2$  phase transformation.

Extended X-ray absorption fine structure (EXAFS) spectroscopy probes the local coordination about an excited atom type providing complimentary information to the equilibrium distances from electron densities discerned by diffraction. The average Ge–O distance within the first coordination shell of  $\text{GeO}_2$  is obtained through fitting an X-ray absorption spectra through a two shell fit, and the resultant pressure response is shown in Figure 2.2d. The resolution of the EXAFS experiment is insufficient to resolve bond lengths beyond  $\sim 0.1 \text{ \AA}$ , in line with most modern EXAFS measurements, so axial and basal distances were not differentiated within a coordination shell. In the rutile phase there is a trend of decreasing average bond length within the first coordination shell with increasing pressure, in line with the diffraction and DFT data (DFT tables in Appendix A). EXAFS shows an earlier onset of disordering than XRD via the average bond lengths at 17.3 GPa and highlights disordering in the system. At 28 GPa EXAFS shows a return to good agreement with the average crystallographic bond length before diverging again at higher pressures. The second cumulant of the EXAFS fit represents the mean squared relative displacement (MSRD) of the atoms, which differs from mean squared displacement (MSD) that can be obtained from XRD in that the MSRD is relative to the atoms’ instantaneous motion from each other, rather than their deviations from their crystallographic equilibrium position. This, while a small distinction, is significant as phonons often transverse in the same direction, however, this will not affect the MSRD as it is only affected by deviations relative to the scattering atom.[146] The  $U_{iso}$  term from the XRD Rietveld refinement was fixed at 0.02 for all atoms and was not refined. Figure 2.2c shows the onset of disordering with a nearly factor of 2 increase of the EXAFS MSRD around 17.3 GPa from 5 GPa, which is in good agreement of disorder with

the half path length. Taken as a marker of deviations of the parallel instantaneous average bond lengths, the initial rapid rise of the MSRD highlights the rapidly increasing librational angle as permitted by a rapidly flattening enthalpy landscape. Both EXAFS metrics indicate reordering following the initial maximum at 17.3 GPa.

The X-ray diffraction shows an abrupt return to the projected trend of pristine rutile phase at 25.4 GPa before deviating again. This indicates a return to an ordered state, driven by an increase in symmetrization in the oxygen positions. DFT predicts an orthorhombically distorted rutile phase to be stable around this pressure (Figure 2.1b), yet the improvement in the statistical quality of fit metrics obtained by refining the XRD data with that structure is not sufficient to justify assigning the feature at 25.4 GPa to an orthorhombic rutile phase. Thus, at this pressure the difference between the rutile and  $\text{CaCl}_2$  phases are at their minimum and will deviate from this pressure on. The anomalous behavior in the EXAFS appears to quench around 28.0 GPa, wherein the average bond lengths return close to the rutile trend and the MSRD drops below that of the rutile phase. The EXAFS average bond lengths above 31 GPa are still below those anticipated by the average weighted crystallographic value determined by XRD. DFT predicts slightly longer bond lengths in the  $\text{CaCl}_2$  phase, so these points as well as the overly short XAS determined bond lengths at 26.5 GPa indicate residual defects are present after the phase transformation.

The relative edge shifts of the XAS spectra (taken as the first critical point of the spectra) can be compared (Figure 2.3) to determine if any electronic response occurs as the material disorders. From 2.4 to 21.5 GPa there is effectively no change in the edge energy indicating a consistent chemical environment of the system. However, there is a noticeable increase in edge energy at 23.5 GPa which persists to the highest pressure measured. Such an increase in edge energy is typically interpreted as an increase of the effective oxidation state of the target atom, implying that the presence of defects is driving some of the Ge atoms to a more ionic state. The increase in edge energy peaks just before the transition into the  $\text{CaCl}_2$  phase at 28 GPa, indicating a peak concentration of defects in the sample. Following the

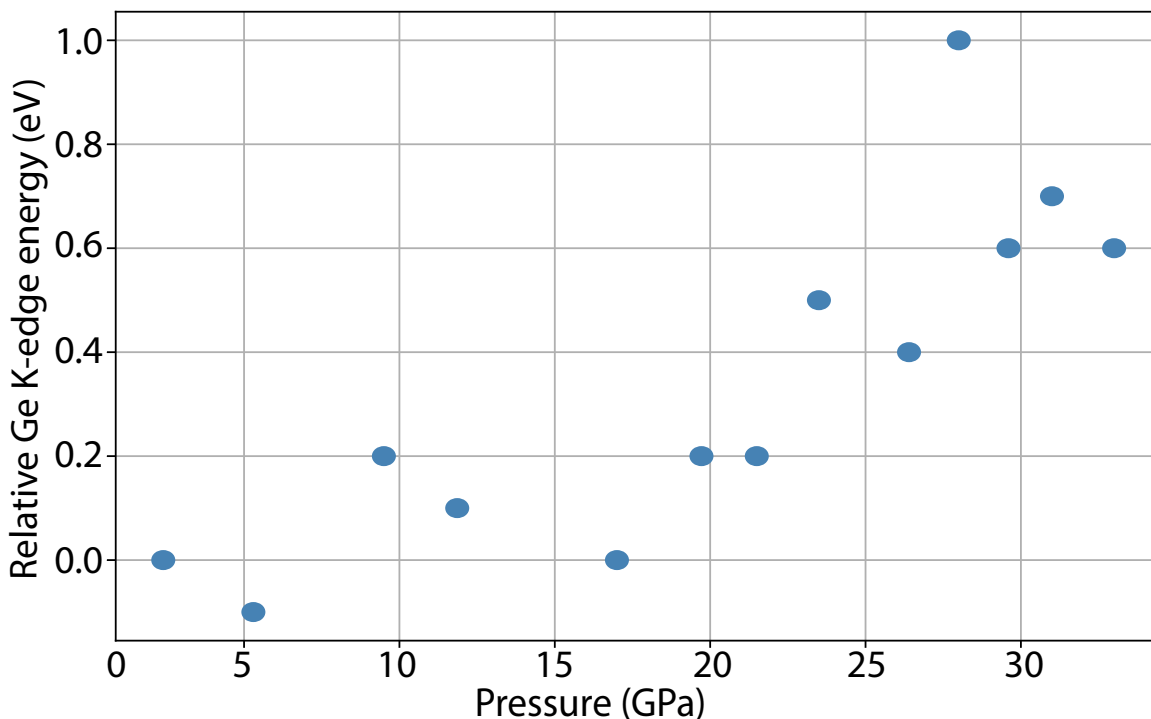


Figure 2.3: The relative change in the Ge K-edge energy as a function of pressure. These energies were determined as the first critical point of the GeO<sub>2</sub> XAS spectrum. Credit: GA Smith, UNLV: XAS Analysis

transformation into the CaCl<sub>2</sub> phase the edge energy decreases while remaining above that of the low pressure rutile phases. While this is an expected effect as these types of oxides typically become more ionic with pressure, the values at the highest pressures still exceed the 0.01 eV/GPa growth rate of the edge energy observed up to 21.5 GPa. Transport measurements using an optometer were attempted to determine if any other electrical responses manifested due to the disordering (full details in Appendix A). Unfortunately, our setup is unable to detect in the sub-picoamp regime, so no useful signal was measured beyond 10 GPa.

To understand the deviations observed in the X-ray measurements, Figure A.11 shows the enthalpic and band gap response for the proposed disordering mechanism of displacing a single oxygen atom along the  $B_{1g}$  librational mode within its respective  $ab$ -plane in a  $3 \times 3 \times 3$  supercell, ie. a 0.91% defect density. In no case is the displacement more favorable than

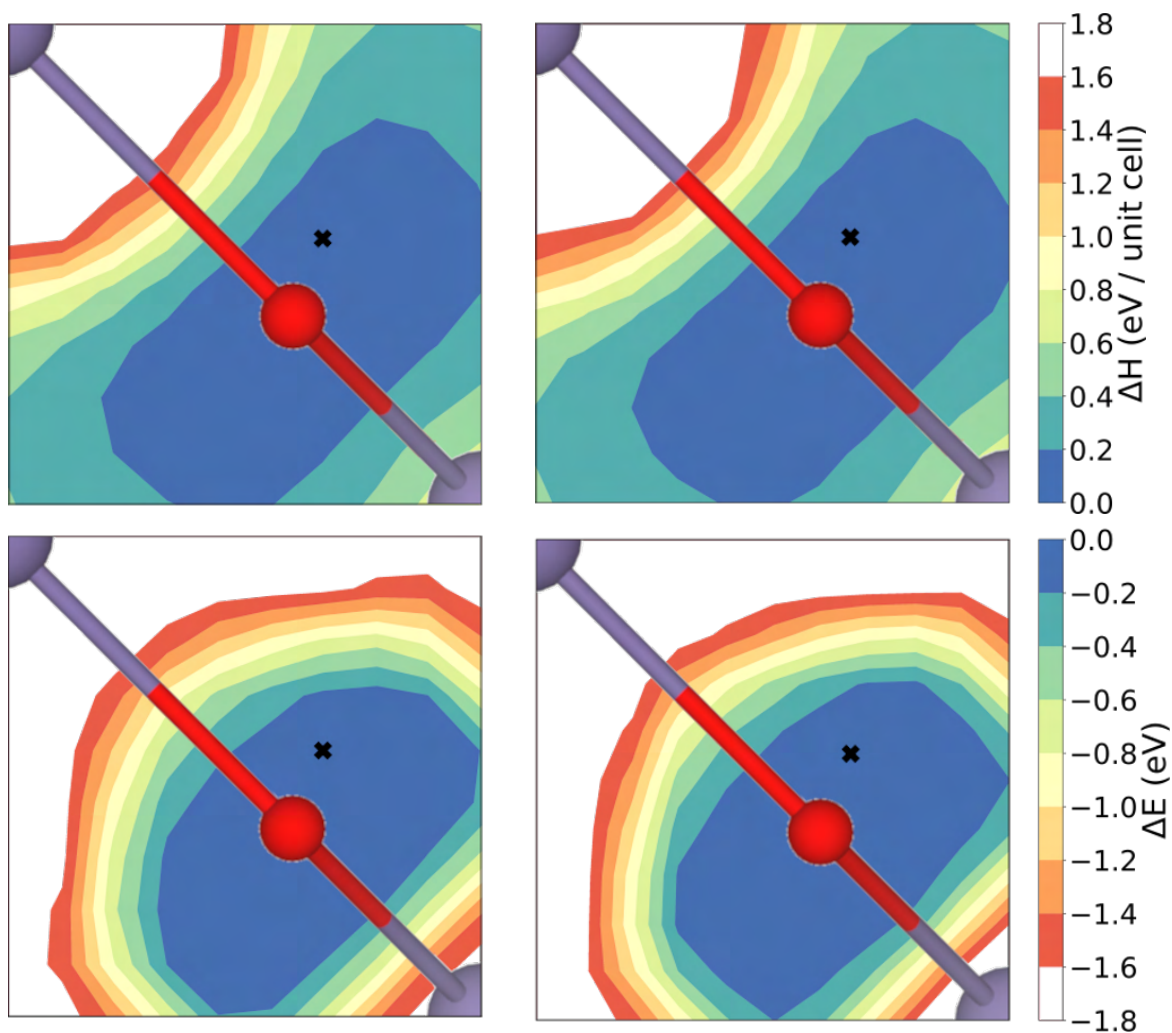


Figure 2.4: The response in (top) enthalpy and (bottom) band gap associated with displacing an oxygen within its *ab*-plane of a  $3 \times 3 \times 3$  rutile supercell of  $\text{GeO}_2$  at 20 GPa (left) and 25 GPa (right). Displacement by  $11^\circ$  relative to the rutile position (within grid resolution) marked with a black x. Credit: Daniel Schacher, Keith Lawler, UNLV: Theory

the base rutile structure, but at both pressures the oxygen can displace by 10-20% along its librational path and still be within a potentially thermally accessible configuration with an  $\Delta H \leq 100$  meV/unit cell. Increasing the defect density to 3.1 % (a  $2 \times 2 \times 2$  supercell, plot in Appendix A) transforms the potential landscape into a steep well about the rutile position such that no significant displacements would be accessible. This confirms there is a low defect concentration at the outset of the disordering as indicated by the equation of state analysis measurements. Interestingly, increasing the pressure with a 0.91 % defect density causes the well to become steeper at the edges, whereas the 3.1 % defect density potential landscape flattens when pressure is increased. This shows that by 20 GPa the quartic nature of the free energy is saturated for low defect concentrations while it is beginning to transform away from a quadratic potential for higher defect concentrations. Both increased defect concentration and increased displacements are allowable with increased pressure, but the effects will be in competition with each other. Therefore, the best explanation for what is observed experimentally is that a low concentration of defects with low displacements emerge around 20 GPa, the magnitude of the displacements increase with pressure, then at a certain pressure a several percent increase in defect concentration can be achieved at the cost of reducing the maximum displacement ( $\sim 26$  GPa), after which the magnitude of the displacements increase with pressure until the  $\text{CaCl}_2$  phase change occurs.

Displacing an oxygen has some effect on the band gap of  $\text{GeO}_2$ , generally lowering it from its value in the pristine rutile state. The effect is minimal with a low defect concentration, not exceeding a 0.03 eV decrease within the 100 meV/unit cell window of configurations at 25 GPa. The response is larger at a higher defect concentration, although it doesn't exceed 0.07 eV at 25 GPa. Such a small predicted response coupled with  $\text{GeO}_2$ 's ultrawide band gap explains why no meaningful transport results were seen with our setup in the disordering region.

To evaluate if other phases could be responsible for the response observed in the X-ray data, several perturbed structures were optimized across 20–30 GPa including rutile super-



cells with single displaced oxygens, swapping the atomic positions between the known phases, and the known phases with small orthorhombic distortions. Nearly all of the perturbed structures revert to either the rutile or  $\text{CaCl}_2$  phase when optimized. However, displacing an O in the  $ab$ -plane within a single rutile unit cell leads to the orthorhombically distorted rutile structure mentioned earlier. The predicted orthorhombic distortion extends  $a$  and contracts  $b$  by similar amounts,  $\sim 0.03 \text{ \AA}$  at 25 GPa. This orthorhombic phase has similar electronic properties to that of the rutile phase but is slightly more dense, leading to its predicted enthalpic favorability between 23 and 27.5 GPa (Figure 2.1b). As stated above, there is insufficient experimental evidence to validate this proposed phase, leaving the structure with a displaced oxygen atom as the leading model to explain the experimental observations.

Having established that distortions along the rutile phase's  $B_{1g}$  librational mode leads to changes in the electronic structure of  $\text{GeO}_2$ , Figure 2.5 contrasts the total charge density and electron localization function for a 25 GPa pristine rutile supercell and one where the single oxygen is displaced by  $1^\circ$  along the  $B_{1g}$  librational mode with a 0.91 % defect density. This point is marked with a black x in Figure A.11, and it was chosen because it is at the edge of the window of potentially accessible displacements with a  $\Delta H$  of 101 meV/unit cell. Note that the octahedra in the  $\text{CaCl}_2$  structure are rotated by  $4^\circ$  relative to the rutile structure. The charge density for the pristine rutile cell (Figure 2.5, top left) shows a strongly polarized charge density about each oxygen atom with lobes in the direction of the Ge atoms with that oxygen in its basal plane, confirming the covalency inferred by bond lengths and their response to compression. When the oxygen atom is displaced (Figure 2.5, top right), its charge density becomes more spherical while the charge density about the other oxygen atoms remain largely unperturbed. The electron localization function (ELF) of the rutile and displaced cell (Figure 2.5, bottom) tell a similar story, where the distortion shifts towards an increased charge localization on the perturbed oxygen. Unlike the total charge density the distorted structure's ELF shows residual charge density (above the uniform electron gas limit) on the Ge atoms the oxygen moved away from. The atom projected charge density

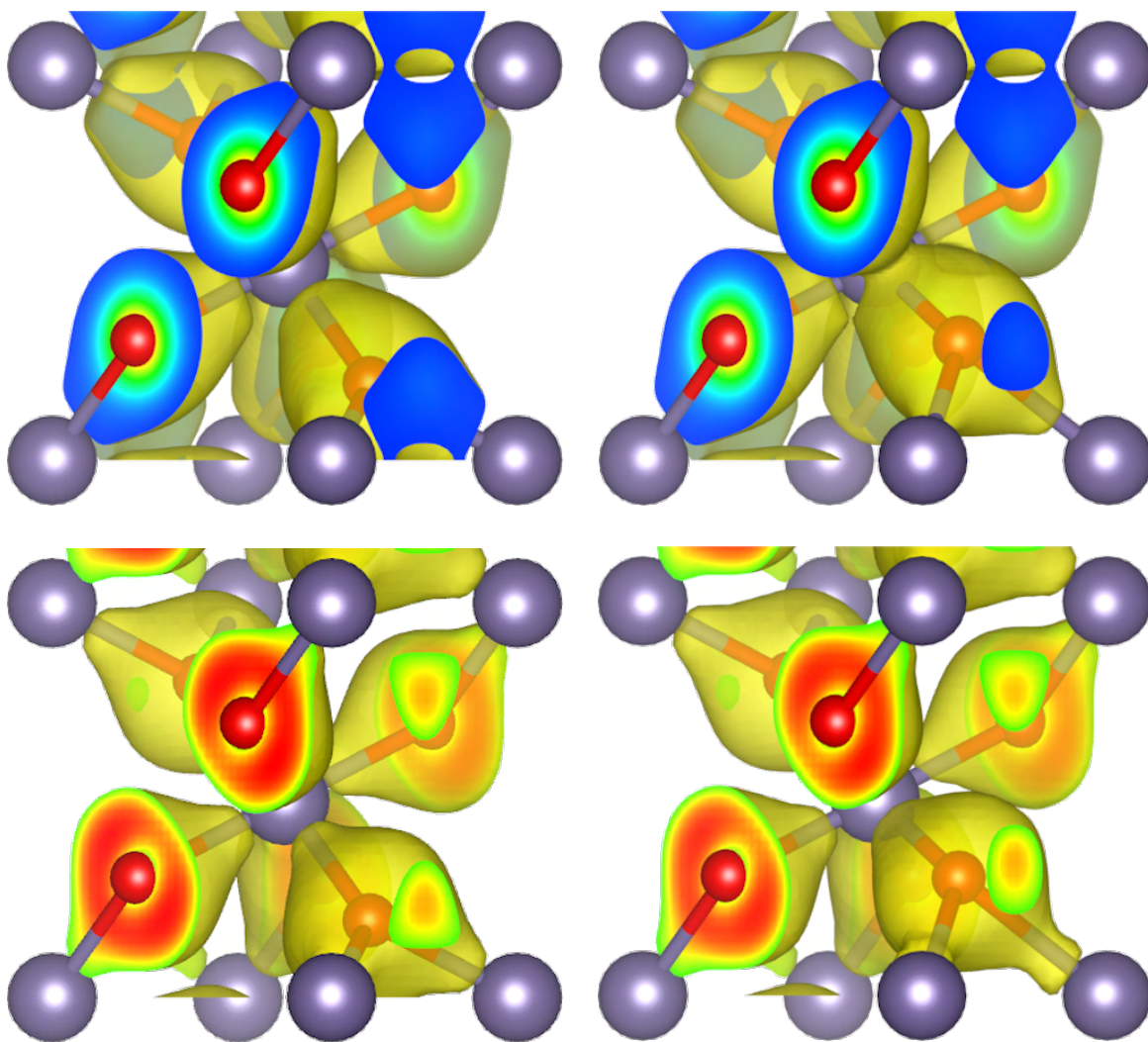


Figure 2.5: (top) The charge density with an isosurface level of  $0.05 e/a_0^3$  and (bottom) electron localization function with an isosurface level of 0.5 for a 25 GPa  $3 \times 3 \times 3$  supercell of (left) pristine rutile  $\text{GeO}_2$  and (right) rutile  $\text{GeO}_2$  with a single  $11^\circ$  oxygen displacement as indicated in Figure A.11. Only one unit cell of the supercell is shown. Credit: Daniel Schacher, Keith Lawler, UNLV: Theory

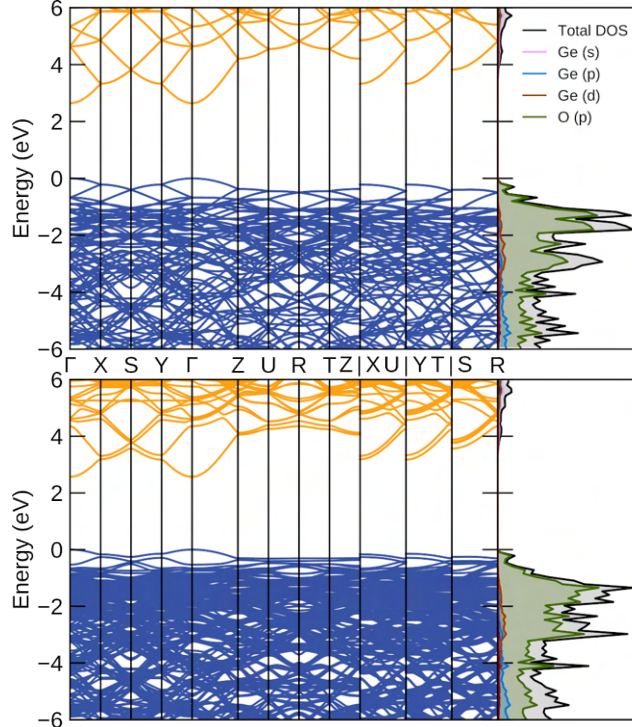


Figure 2.6: The band structure and projected density of states for a 25 GPa  $\times 3 \times 3$  supercell of (top) pristine rutile  $\text{GeO}_2$  and (bottom) rutile  $\text{GeO}_2$  with a single  $11^\circ$  oxygen displacement as indicated in Figure A.11. Credit: Daniel Schacher, Keith Lawler, UNLV: Theory

shows an accumulation of  $0.04e$  of charge on the displaced oxygen, yet those neighboring Ge atoms with residual electron localization loose  $0.1e$  of charge a piece. Thus, the displacement involves metal-to-ligand charge transfer, yet the transferred charge density is more diffuse than the displaced oxygen's PAW sphere.

The band structure for a  $3 \times 3 \times 3$  rutile  $\text{GeO}_2$  supercell with a single displaced oxygen atom (Figure A.12) shows that most of the individual bands within the valence and conduction band don't alter much from the rutile phase beyond degeneracy breaking from the increased asymmetry of the disordered state. The curvature of the bands near the conduction band minimum (CBM) is largely unchanged by the disordering, looking primarily like split versions of the same bands. Near the valence band maximum (VBM), the split bands are flatter than their rutile counterparts. If the defect is propagated further, for instance with a  $31^\circ$  displacement in a  $2 \times 2 \times 2$  supercell, those effect is far more prominent with three nearly

flatten bands comprising the VBM (plot in Appendix A). These changes in curvature of the VBM increase the effective hole mass of the material, in turn effecting several of the material's transport, optical, and electron-phonon related properties.[147] In particular, the increase in effective hole mass along with the mostly unchanged effective electron mass should increase conductivity in disordered rutile materials, although these simulations show the effect will depend heavily on the concentration and magnitude of disordering defects.

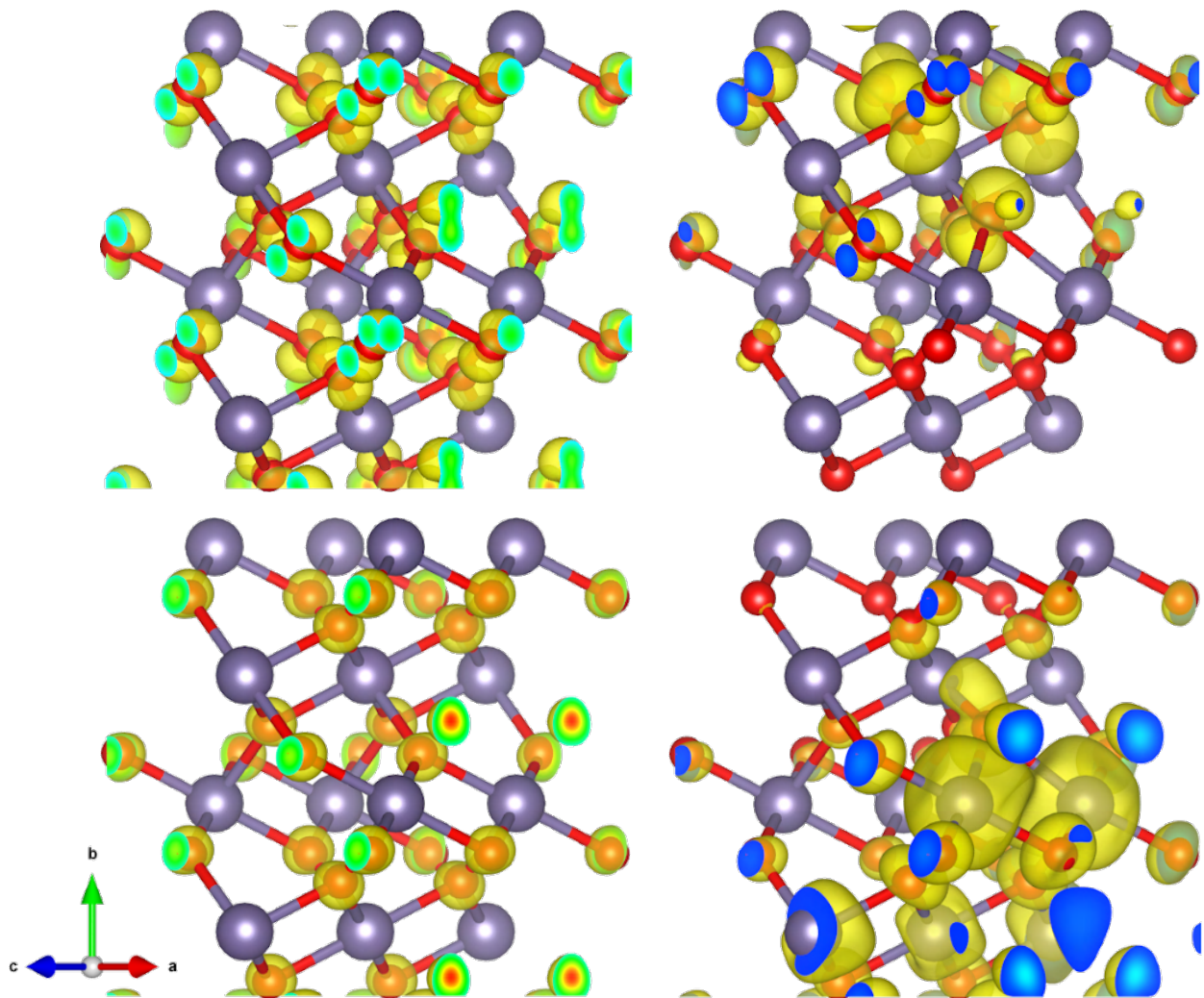


Figure 2.7: Band decomposed charge densities for the (top) valence band maximum and (bottom) conduction band minimum for a 25 GPa  $3 \times 3 \times 3$  supercell of (left) pristine rutile  $\text{GeO}_2$  and (right) rutile  $\text{GeO}_2$  with a single  $11^\circ$  oxygen displacement as indicated in Figure A.11. All isosurfaces are at  $0.001 e/a_0^3$  and show only the relevant portion of the supercell. Credit: Daniel Schacher, Keith Lawler, UNLV: Theory

The flatter bands at the VBM of disordered rutile  $\text{GeO}_2$  can indicate spatial localization, which the band decomposed charge density (Figure A.13) confirms to be the case even for the nearly rutile-like bands of the  $11^\circ$  displacement in a  $3 \times 3 \times 3$  supercell. The VBM of the distorted rutile phase shows the formation of a small polaron composed of a polarized p state on the displaced oxygen with a strong coupling to p states on nearby oxygen atoms. This is in contrast to the VBM of the rutile phase which is a Bloch function of oxygen p states. The formation of small polarons localized on the distorted oxygen atom is in line with the increase in the Ge K-edge energy observed when  $\text{GeO}_2$  defects, in that charge density is localizing on the displaced oxygen and removing covalently shared density from the Ge. Polarons such as these have previously been observed in rutile materials via doping/vacancies [148, 149, 150, 151, 152] (including  $\text{GeO}_2$ )[131] or photoinduction.[152, 153] Small polarons are known to facilitate electron transport via a hopping mechanism mediated through electron-phonon interactions,[154, 149, 153] with a tunneling probability pre-factor on the order of the phonon frequencies and an average rate proportional to the polaron concentration.[155] Thus, pressure inducing such defects offers an alternate means from doping to create small polarons in rutile materials to tune their electronic properties.

## 2.5 CONCLUSIONS

In conclusion, X-ray and Raman measurements confirm disordering in the oxygen sub-lattice of rutile  $\text{GeO}_2$  just before the  $\text{CaCl}_2$  phase transformation, providing further evidence for the universality of a disordered, pre-transition state in rutile oxides. This pre-transition, disordered state is driven by oxygen displacements arising from the softening  $B_{1g}$  octahedral libration mode, with ion identity affecting the stability window for a disordered state. DFT simulations indicate that the disordering of an oxygen atom comes with an enthalpy penalty which also lowers the band gap of the material. The simulations also show the lowered band gap is due to an emerging flat band near the Fermi level in the disordered state which

represent the formation of a small polaron about the displaced oxygen atom.

## 2.6 ACKNOWLEDGEMENTS

This material is based upon work supported by the Air Force Office of Scientific Research under award number FA9550-21-1-0097. Portions of this work were performed at HPCAT (Sector 16), Advanced Photon Source (APS), Argonne National Laboratory. HPCAT operations are supported by DOE-NNSA's Office of Experimental Sciences. The Advanced Photon Source is a U.S. Department of Energy (DOE) Office of Science User Facility operated for the DOE Office of Science by Argonne National Laboratory under Contract No. DE-AC02-06CH11357. The authors thank the UNLV National Supercomputing Institute for computational resources and support.

## CHAPTER 3

# CARBON CONTENT DRIVES HIGH TEMPERATURE SUPERCONDUCTIVITY IN A CARBONACEOUS SULFUR HYDRIDE BELOW 100 GPa

### 3.1 ABSTRACT

We report a previously unobserved superconducting state of the photosynthesized carbonaceous sulfur hydride (C-S-H) system with a maximum  $T_C$  of 191(1) K below 100 GPa. The properties of C-S-H are dependent on carbon content, and X-ray diffraction along with simulation reveals the system retains molecular-like packing up to 100 GPa.

### 3.2 STATEMENT OF EFFORT AND PERMISSION

The following chapter was published in Chemical Communications.[8] In this work, I performed experiments, analyzed data, and performed the writing for this work. Reproduced with permission from Royal Society of Chemistry:

[https://www.rsc.org/journals-books-databases/author-and-reviewer-hub/  
authors-information/licences-copyright-permissions/](https://www.rsc.org/journals-books-databases/author-and-reviewer-hub/authors-information/licences-copyright-permissions/)

### 3.3 MANUSCRIPT

The superhydride superconductor is envisioned as a hydrogen dominant alloy which lowers the pressure required to achieve the favorable properties and high- $T_c$  predicted for dense metallic hydrogen.[56, 31, 1, 156] Hydrogen within these alloys takes part in an extended

bonding network, be it the purely hydrogenic clathrate sublattice of a metal superhydride, or a covalent network with other elements as in  $\text{H}_3\text{S}$ . [157, 4, 158] There have been record breaking milestones within the covalent superhydrides, including a 203 K  $T_c$  for  $\text{H}_3\text{S}$  at 155 GPa [159, 160, 161] and a 288 K  $T_c$  at 267 GPa in carbonaceous sulfur hydride (C-S-H). [3] C-S-H was first synthesized from elemental precursors at 4 GPa, and then compressed without thermal annealing into its final reported superconducting state, a pathway likely leading to metastable states. C-S-H has since been synthesised by reacting elemental S and  $\text{CH}_4\text{-H}_2$  fluid mixtures. [162] In principle, this method permits greater control of C concentration, although the reported C-H Raman modes are comparably weak, and whether it leads to high- $T_c$  states is yet to be studied. From either synthetic route, C-S-H displays a rich phase diagram below 100 GPa where evidence points to a retention of molecular-like packing as well as metallization. [3, 162]

While the exact identity of the record-breaking C-S-H material has yet to be discerned, candidate structures have been proposed from crystal structure prediction (CSP) and virtual crystal approximation simulations. [163, 164, 165, 166, 167, 168] Many of the CSP candidates for C-S-H are molecular or exhibit a molecular sub-unit, including the leading candidates with  $\text{CH}_4$  intercalating or replacing an  $\text{H}_3\text{S}$  unit within the  $\text{H}_3\text{S}$  perovskite-like lattice. [163, 164, 167, 169] While these low-dimensional sub-units seem contrary to the extended bonding network, our recent simulations showed that dispersion interactions can potentially be important in covalent superhydrides with such sub-units. [170] Along these lines, it was recently discovered that a metal superhydride with a relatively low hydrogen concentration,  $\text{YH}_6$ , exhibits an anomalously high  $T_c$  at lower pressures than its more studied higher hydrogen content counterparts. [171]

Building on the high  $T_c$ s reported at 100s of GPa for the superhydrides, the next goal towards achieving ambient superconductivity is to lower the critical pressure required to form superconducting phases. [172] Herein, we investigate C-S-H below 100 GPa to probe for lower-pressure superconducting states predicted by CSP, and to further understand the



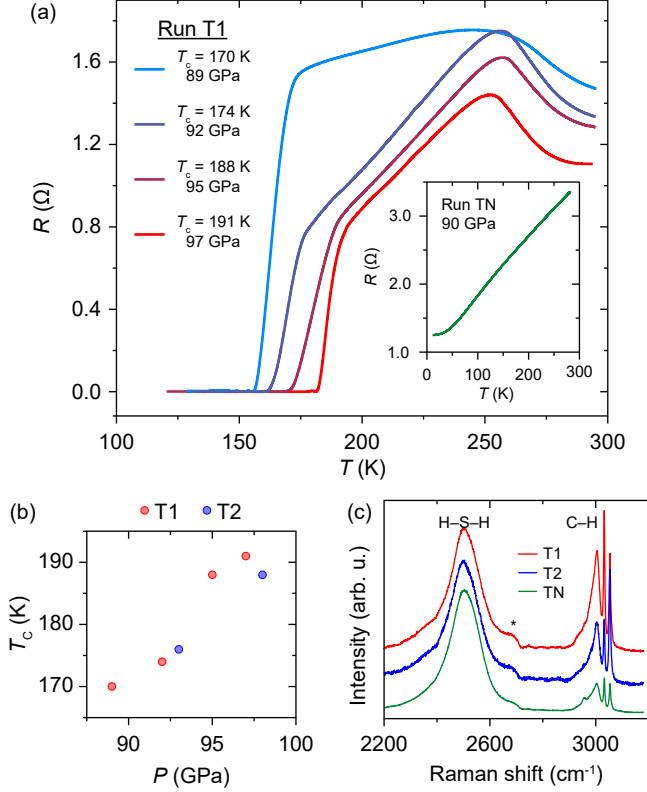


Figure 3.1: (a) Resistance response of C-S-H (Run T1) on cooling, displaying a superconducting transition at 191 K at 97 GPa. (Inset)  $R$  response from Run TN at 90 GPa showing metallic behavior. (b) Evolution of  $T_c$  with  $P$  for Runs T1 and T2. (c) Comparative Raman spectra of Runs T1 and T2, and Run TN at 4.0 GPa and 300 K. The feature marked with an asterisk (\*) is second-order Raman scattering from diamond. Credit: Dias Group, University of Rochester: Resistance measurements and Raman; Dean Smith, UNLV: Artistic design.

consequences of the thermodynamic pathway for synthesizing C-S-H from elemental precursors. We present electrical transport measurements in this previously unexplored pressure regime that reveal a remarkably high  $T_c$  in some crystals, raising the question as to how these macroscopic quantum states emerge over such dramatically different  $P$ - $T$  ranges. Synchrotron single crystal X-ray diffraction (SC-XRD) identifies structural evolution of C-S-H up to 100 GPa and Raman spectroscopy shows that the C content in C-S-H produced by photochemistry varies in each crystal synthesised. That variation directly affects the material properties with subtle differences in packing densities. Density functional theory (DFT) assists in understanding the H positions of the determined phases.

All crystals of C-S-H here are synthesized using the procedure of [3] (full details in Appendix B). Ball-milled mixtures of elemental C and S with dimensions about 15% of the diamond culet (typically 100–250  $\mu\text{m}$ ) are placed into the sample chamber of a diamond anvil cell, along with a ruby sphere.[173] Gas phase  $\text{H}_2$  is loaded at 0.3 GPa.[174] Samples are then pressurized to 3.7–4.0 GPa and excited for several hours using light from a 514 nm laser with power ranging from 10 and 150 mW depending on sample response. Crystal growth is monitored *in situ* by visual observation, and Raman spectroscopy confirms the transformation into C-S-H by the presence of characteristic C–H, S–H, and H–H Raman modes. Samples are compressed to 10 GPa after transformation and characterization by Raman spectroscopy to avoid decomposition.

We performed electrical transport measurements on 3 newly-synthesized crystals of C-S-H – Runs T1, T2, and TN – following the methods described in [3] (Fig 3.1). In 2 separate runs, we observe maximum  $T_c$ s of 191(1) K at 97(5) GPa (Run T1, Fig 3.1a and Fig 3.1b) and 188(1) K at 98(5) GPa (Run T2, Fig 3.1b). These transitions occur at roughly half the pressure required to achieve a similar  $T_c$  in either C-S-H or S-H/S-D.[3, 175] Runs T1 and T2 are contrasted with Run TN, which does not exhibit a superconducting transition at 90(5) GPa on cooling to 10(1) K, despite exhibiting metallic character (Fig 3.1a inset). The shape of the  $T_c$  vs. pressure (Fig 3.1b) implies this superconductivity comes from a distinct phase than that at 267 GPa. Also observed in Run T1 is the previously noted behavior of C-S-H to exhibit increasingly narrow  $\Delta T/T_c$  as a function of increasing pressure and  $T_c$ , exhibiting a minimum  $\Delta T/T_c$  of 0.0373 at 97 GPa (data in Appendix B).

By virtue of our focus on the lower pressure phases of the C-S-H ternary, the samples used in this study are significantly larger than those in [3], by a factor of 3–10, and these larger crystals have a heterogeneous C concentration compared with crystals from our previous work. This inhomogeneity is evidenced by variations in the relative intensities of Raman modes originating from C–H stretches around 3000  $\text{cm}^{-1}$  and H–S–H bends around 2500  $\text{cm}^{-1}$ , ie.  $I_{\text{C-H}}/I_{\text{H-S-H}}$ . Fig 3.1c shows representative Raman spectra of C-S-H crys-

tals from each of the three runs following their initial synthesis at 4 GPa, with variations in  $I_{C-H}/I_{H-S-H}$  evident. Run TN, which did not exhibit a superconducting transition at 90(5) GPa, has an intensity ratio  $I_{C-H}/I_{H-S-H}$  of 0.27. Meanwhile, Runs T1 and T2 have  $I_{C-H}/I_{H-S-H}$  of 1.16 and 0.93, respectively. It is important to note that even our Run TN has a higher  $I_{C-H}/I_{H-S-H}$  than the samples reported in [3] which become superconducting at room temperature under compression ( $I_{C-H}/I_{H-S-H} = 0.08$ ). Thus, increased C concentration in the C-S-H ternary system is linked to a significant reduction in the pressure required to reach the superconducting regime.

Each of the  $R(T)$  responses at the different pressures measured from Run T1 feature a turning point above the superconducting transition around 250 K (Fig. 3.1a). At these conditions C-S-H exhibits the temperature response of a finite gap system, whereas just below 250 K the temperature response is metallic. This behavior at 250 K likely results from either a structural or electronic phase transition. An electronic transition would not likely be accompanied by a change in symmetry, and a structural transition in a hydride material might also be indistinguishable using XRD if the heavy atom sublattice does not re-order, as is the case for the  $R3m$  to  $Im\bar{3}m$  transition in  $H_3S$ . [161] Resistance continues to decrease with lowering temperature before a sharp drop to zero resistance as the critical temperature is crossed. Such a difference in  $T_c$  to that of [3] could be expected, as their thermodynamic approach to a superconducting state begins from cooling in the recently confirmed  $Im\bar{3}m$  phase emerging above 159 GPa [162] rather than the previously reported phase IV. [3]

SC-XRD measurements on other crystals were conducted at HPCAT with  $\lambda = 0.34453 \text{ \AA}$ . Conical diamonds with  $80^\circ$  apertures were used for greater completeness in SC-XRD. Fig 3.2 shows the  $P$ - $V$  response of 8 C-S-H crystals from 3 separate runs, with all data on phase III/IV collected during Run X2. 2<sup>nd</sup>-order Birch-Murnaghan equations of state are fit to each crystal and phase (values in Table SI). We observe subtle systematic differences in  $V$ - $P$  relations across the different crystals measured at the same thermodynamic conditions. The largest difference in  $V$  is 2.9% at 28.9(5) GPa in Run X2 between crystals C1 and C4.  $K_0$

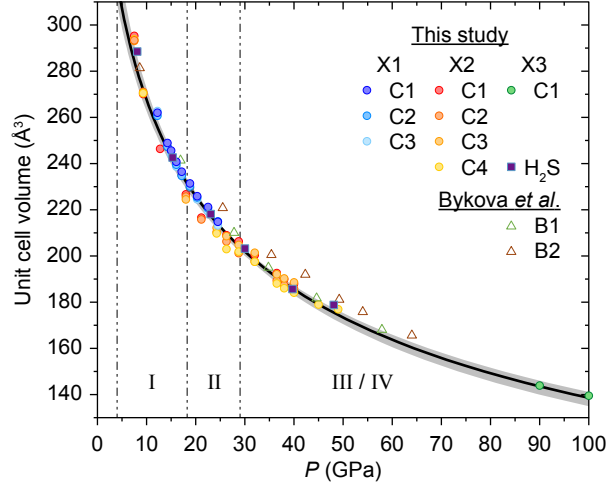


Figure 3.2:  $P$ - $V$  relations of C-S-H at 300 K compared with values from H<sub>2</sub>S and [87]. A 2<sup>nd</sup> order Birch-Murnaghan equation of state was fit with initial volume  $V_0 = 400.573 \text{ \AA}^3$  and bulk modulus  $K_0 = 11.028 \text{ GPa}$  (black line), and the gray area denotes uncertainty derived from high and low bands for Runs X1 and X2. Phase division for I ( $I4/mcm$ )  $\rightarrow$  II ( $C2/c$ )  $\rightarrow$  III/IV ( $I4/mcm$ ) are taken from [87]. Credit: GA Smith, UNLV: Sample preparation and data acquisition; Ines Collings, Centre for X-ray Analytics, Empa: SC-XRD analysis; Dean Smith, UNLV: Artistic design.

was found to range between 7.321 and 14.496 GPa for Runs X1 C3 and X2 C3.  $V$  trends for all of the C-S-H crystals measured are equal or lower than that of our own measurements on pure H<sub>2</sub>S+H<sub>2</sub>, which in turn is noticeably lower than that reported for C-S-H prepared from mixtures of molecular gases.[87] This, along with differences in the electronic response between crystals measured here and in [3], suggests a large variability in C-S-H stoichiometry generated by photochemistry under pressure.

Leading up to 18 GPa, SC-XRD measurements confirm phase I [3] as the Al<sub>2</sub>Cu-type structure ( $I4/mcm$ ) previously identified in CH<sub>4</sub>-H<sub>2</sub> and H<sub>2</sub>S-H<sub>2</sub> mixtures.[176, 177, 87] The  $I4/mcm$  phase is inferred between 4 to 9 GPa as no change is observed by Raman spectroscopy. Due to insufficient C concentration or unique crystallographic placements, SC-XRD measurements are unable to resolve between C and S on the  $8h$  Wyckoff positions, thus Fig 3.3a displays only H<sub>2</sub>S units on the  $8h$  sites. Applying the Bernal-Fowler "ice rules" [178] to determine the H positions within  $I4/mcm$  of the H<sub>2</sub>S molecular units results

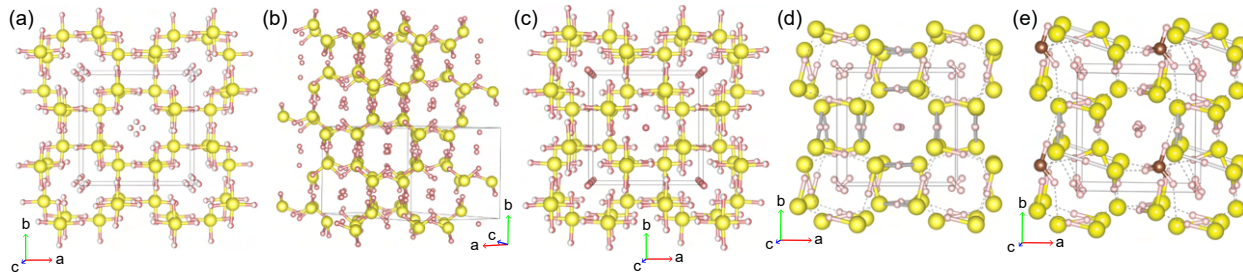


Figure 3.3: SC-XRD determined structure at (a) 9 GPa  $I4/mcm$  (b) 29 GPa  $C2/c$  and (c) 50 GPa  $I4/mcm$  C-S-H. (d) DFT derived structure at 90 GPa – bicolor cylinders represent bonds ( $\leq 1.43 \text{ \AA}$ ), silver cylinders represent H atoms shared between two heavy atoms (1.43–1.53  $\text{\AA}$ ), and dashed lines represent H bonds (1.53–2.0  $\text{\AA}$ ). (e) Lowest enthalpy structure found here when substituting a  $\text{CH}_4$  for an  $\text{H}_2\text{S}$  in the 90 GPa structure shown in (d). Yellow spheres represent S throughout, brown spheres C, and pink spheres H. Credit: Keith Lawler, UNLV: Theory.

in partially occupied  $16k$  Wyckoff positions, and this constrains the  $\text{H}_2\text{S}$  molecular units to be planar within  $\{002\}$  as in [177].

A CSP study on the H–S system identified a  $P1$  modification which mostly varies from the  $I4/mcm$  H positions owing to out-of-plane rotation of the molecular sub-units.[160] Comparing several planar arrangements of the H atoms (keeping the lattice and S positions fixed at their experimental values) versus the arrangement of the  $P1$  structure with DFT and the vdW-DF2 functional shows a  $\sim 0.44 \text{ eV}$  preference for a non-planar H arrangement.[179] This indicates C-S-H will have non-planar arrangements of  $\text{H}_2\text{S}$  molecular units to facilitate interactions between the shorter 3.30  $\text{\AA}$  inter-plane nearest neighbor S atoms. The magnitude of the enthalpic differences shows weak packing forces that could enable the molecular sub-units to behave as weakly constrained rotors within their respective molecular volume when thermalized. Given the orientational preference in the interplane direction and the S–S nearest neighbor distances being within the van der Waals and  $\text{H}_2\text{S}$  dimer H-bonding distances,[180] there is at least some weak H-bonding contributing to the cohesion of the lattice along with the primary van der Waals forces.

Above 18 GPa, C-S-H transforms into a  $C2/c$  phase (Fig 3.3b). This transition was observed in all crystals of Run X1 and in  $\text{H}_2\text{S}+\text{H}_2$ , but was not present in C1 and C4 of Run X2.

The absence of  $C2/c$ -type C-S-H in some crystals is consistent with observations in [87] and [162], where the phase is observed only in crystals with low C content, and further exemplifies the variation in stoichiometry in C-S-H formed by photochemistry. It is worth noting the similarities between the  $C2/c$  structure of C-S-H and previously documented structures of H-S. The  $Cccm$  H-S structure from [160] is preferred by [181] owing to its H-S-H network providing an additional distinct environment for molecular  $H_2$  units, which is reflected in the Raman vibron. This and the  $I222$  structure reported by [177] differ from the  $C2/c$  structure only in the orientation of  $H_2S$  sub-units and apparent directionality of the H bonding network. The  $C2/c$  phase resembles a monoclinically-distorted version of the  $I4/mcm$  phase where the [101] direction of the  $C2/c$  structure roughly corresponds to the [001] direction of the  $I4/mcm$  structure. In both cases, that direction resembles a 2-dimensional pore formed by S atoms interconnected by inter-plane H-bonding that encapsulates the  $H_2$  molecules, and the views shown in Fig 3.3 are all oriented to look along this pore-like structure. The H positions determined by SC-XRD are reminiscent of the 9 GPa structural optimizations.

C-S-H transforms back into an  $I4/mcm$  structure around 29 GPa (Fig 3.3c) which persists to our highest measurements at 100 GPa. Our measured phase transitions by SC-XRD agree well with those reported in Raman studies.[3] The H positions of the  $H_2S$  units are again best modeled crystallographically within the constraint of the  $I4/mcm$  group to be in a planar configuration. However, DFT dictates that orientations with out-of-plane H positions are 5–7 eV more enthalpically favorable, and the lowest enthalpy configuration found here (structure in Appendix B, but like Fig 3.3d) shows a H-bonding network creating 2 dimensional channels along [001].

The previous reported transformation from phase III to IV around 45 GPa or metallization above 60 GPa are not distinguished by SC-XRD as the structural solution remains  $I4/mcm$  up to our highest measurement at 100 GPa. Optimizing the lowest enthalpy 50 GPa configuration using the lattice and S positions determined by SC-XRD at 90 GPa shows a H-bond symmetrization along [001] as in  $Im\bar{3}m$   $H_3S$  (Fig 3.3d).[161] Other configurations

were evaluated confirming the structure with zig-zag H-bonding along [001] is the most enthalpically favorable at 90 GPa. This marks a transition from a double-well to a single-well potential for those H atoms, and is accompanied by a significant drop in the band gap (of the S and H only system) from 1.99 eV at 50 GPa to 0.25 eV at 90 GPa. Thus, the transition from phase III to phase IV is this transition from H-bonding to covalency which eventually drives metallization. It should be noted that the planar configurations considered at 50 and 90 GPa are metallic, so any H<sub>2</sub>S molecules metastably trapped in planar orientations could drive metallization sooner than the double-to-single well transition.

A prototypical carbonaceous model can be created by substituting one of the H<sub>2</sub>S molecules of Fig. 3.3d with a CH<sub>4</sub> molecule. Optimizing the H positions of that model shows a disruption to the zig-zag S–H–S network along [001] in the vicinity of the CH<sub>4</sub> (structure in Appendix B), coupled with a reduction of metallicity compared to the S–H system. The lowest enthalpy structure found increases the band gap to 1.36 eV but does orient the CH<sub>4</sub> to form linkages reminiscent of those seen in *R3m* CSH<sub>7</sub>.<sup>[170]</sup> A higher enthalpy (structure in Appendix B) structure rotates the CH<sub>4</sub> such that the adjacent H<sub>2</sub>S molecules are more like Fig 3.3d accompanied by a  $\sim 0.27$  eV lower band gap. While a metallic modification of this model was not identified here, these results suggest that the turning points of the  $R(T)$  curves in Fig. 3.1a arise from orientational ordering and H-bond symmetrization within the C-S-H sample.

In conclusion, new transport measurements on C-S-H with greater C content show a transition to a superconducting state with maximum  $T_c$  of 191 K at 91 GPa – significantly lower than previously observed. SC-XRD confirms a phase evolution of *I4/mcm* to *C2/c* to *I4/mcm* in crystals with lower C content, while more carbonated crystals bypass the monoclinic phase. The absence of an measurable transition from phase III to IV seen in earlier Raman studies indicates that the transition is likely a reordering of the H which leaves the S sublattice unchanged, which is supported by DFT simulations. That greater C content inhibits the formation of monoclinic C-S-H, but also promotes a transition to

a superconducting state at significantly lower pressures is worthy of further study, and a major challenge for the study of C-S-H is to ensure control of the product and controllable concentration of the constituent elements during the photo-induced reaction.

### 3.4 ACKNOWLEDGEMENT

This work supported by the U.S. Department of Energy, Office of Basic Energy Sciences under Award Number DE-SC0020303. This research is funded in part by the Gordon and Betty Moore Foundation's EPiQS Initiative, Grant GBMF10731 to AS and RPD. Portions of this work were performed at HPCAT (Sector 16), Advanced Photon Source (APS), Argonne National Laboratory. HPCAT operations are supported by DOE-NNSA Office of Experimental Sciences. The Advanced Photon Source is a U.S. Department of Energy (DOE) Office of Science User Facility operated for the DOE Office of Science by Argonne National Laboratory under Contract No. DE-AC02-06CH11357.



## CHAPTER 4

### STOICHIOMETRIC DETERMINATION OF CLATHRATE-LIKE YTTRIUM HYDRIDES AT MEGABAR CONDITIONS

#### 4.1 STATEMENT OF EFFORT AND PERMISSION

In this work, I performed experiments, analyzed data, and performed the writing for this work

#### 4.2 MANUSCRIPT IN PROGRESS

The dream of achieving room temperature superconductivity began nearly 60 years ago with the prediction of high-temperature superconductivity in the type-II superconductor metallic hydrogen. [1]. The practical limitations for achieving metallization of hydrogen at 495 GPa and 5.5 K [2] turned many towards hydrogen dominant alloys beginning with binary metal hydrides, predicted to resemble the superconductivity behavior of metallic hydrogen at significantly lower pressures, typically around 1.5 Mbar in  $MH_6$  structures[57], and eventually, the field turned towards more hydrogen-rich, rare earth hydrides adopting  $REH_9$  and  $REH_{10}$  structures [59]. The addition of heavy cationic species to help coordinate dense  $H^-$  sublattices or add an electron to the non-bonding ( $\sigma^*$ ) orbital to create the Wigner-Huntington like state of atomic metallic hydrogen, or both, was predicted to increase  $T_C$  substantially. [61]

Binary rare earth metal hydride systems were predicted to be excellent candidates for achieving near room temperature superconductivity, with early predictions of both  $LaH_{10}$  and  $YH_{10}$  both achieving higher  $T_C$ s than 0 C, with well understood, conventional, super-

conducting mechanisms [56]. Experimental measurements confirmed high  $T_C$ s, but below theoretical predictions with maximum  $T_C$ s of 260 K at 188 GPa and 262 K at 182 GPa for  $\text{LaH}_{10}$  and  $\text{YH}_9$  respectively [5, 4]. Based on the recent success of binary rare earth hydrides, extensions to ternary hydrides has become an exciting field of study, such as the combination of the previous two materials being combined in  $(\text{La,Y})\text{H}_{10}$  recently being studied achieving a  $T_C$  of 253 K at 183 GPa[68].

Despite these achievements, experimentally characterizing the most critical behavior of the superconducting hydrogen sublattice [75] within these systems proves challenging, even at ambient conditions. X-ray diffraction is an excellent probe to characterize the heavy cationic sublattice, but due to scattering being proportional to the square of the atomic number, information on the hydrogen sublattice is sparse. These experimental challenges result in most of what is known of a hydrides sublattice is known through theoretical studies.

Many experimental studies infer hydrogen coordination [5, 182, 67] through compressibility in diffraction, corroborated through calculations, but density functional theory often struggles with hydrogen containing materials due to the quantum effects of strongly anharmonic Morse potentials, difficulty handling temperature, and inability to account for fractional stoichiometries without exponentially more resource intensive supercells. A change in coordination number having an accompanied change in compressibility is a valid expectation. However, previous studies have shown calculated compressibilities can be overestimated, and true coordination number differed from what was expected using compressibility in  $\text{Sn}_3\text{N}_4$ , as experimentally determined using x-ray absorption measurements [77].

A promising technique to determine coordination, x-ray emission spectroscopy (XES), has recently become viable at megabar pressures due to advancements at x-ray source facilities and presents a technique that could stoichiometrically fingerprint hydrides. XES has proven to accurately determine coordination in structurally complicated systems such as amorphous germania, where using the  $K\beta''$  "cross-over transition" information on both bond length and coordination number were extracted, due to the sensitivity of both the broaden-

ing and intensity in XES [94]. Using valence to core (VTC) regions of the emission spectra should allow for indirect observations of stoichiometry as a result of changes in the p-DOS of these hydride materials. Furthermore, XES has proven to be robust, effective at discriminating between samples when with phase coexistence at high pressures and temperatures [93], potentially even allowing for determination of fractional stoichiometries.

In this study, we present VTC x-ray emission spectroscopy data to show that differentiation of integer stoichiometries through direct measurements of hydrides are possible, resolving  $\text{YH}_2$ ,  $\text{YH}_3$ , and  $\text{YH}_4$  at pressures relevant to the synthesis of the super-hydride systems.

XES measurements were performed at ID20 at the ESRF above the K edge of yttrium (17.2 keV). Modified BX90 design cells were made to optimize the use of mismatched Boehler-Almax conic with standard brilliant cut diamonds that would accommodate a 30 degree radial exit aperture for collection of XES spectra. Beam was delivered axially and measurements were made radially using a van Hamos style spectrometer.

Samples of 99% purity yttrium foil were loaded into the diamond anvil cell with a Re foil or Be gasket micromachined using a pulsed 1064 nm laser. Cells were then sealed inside a glove box with an argon environment with less than 0.5 ppm  $\text{O}_2$  and  $\text{H}_2\text{O}$ . Cells were loaded with 3 kbar of  $\text{H}_2$  gas and compressed to 10 GPa to allow for high initial density of  $\text{H}_2$ . At 10 GPa cells were laser heated using a 1070 nm YLR laser and again at the final pressure.

X-ray diffraction was acquired at 17.01 KeV using a PILATUS 300KW detector at the ESRF at ID20 and diffraction for the highest pressure samples with Be gaskets were acquired at ID15 at the ESRF at 30 keV to allow for high resolution diffraction. *Dioplas* software was used to integrate detector images and diffraction patterns were refined using *GSAS-II*.

Unexpected anvil failure during XES measurements hindered acquisition of a thorough data point density above a megabar. Anvil failure occurred, typically within less than an hour, during measurements when cells were above a megabar, even with aggressive attenuation, leading us to believe it is likely not a result of X-ray damage threshold. The cause of

this failure is not well understood, though the anvil failure always occurs on the diamond incident to the beam during acquisitions. It should be noted that pressure was not modulated during measurement and pressure hadn't changed since the cells had been laser heated between 2 weeks and 2 months prior. Anvil failure occurred on all samples observed in hydrogen, neon, and helium mediums, making hydrogen radicalization an unlikely candidate of anvil failure, though, likely a contributing factor to cells that had a hydrogen PTM. The x-ray beam certainly creates a large number of free electrons and currently, we speculate that these electrons lead to anvil failure at high pressures. It is possible that acquiring spectra relatively close to the k-edge results in near resonant effects potentially leading to plasmonic heating, though this effect was not measured and we do not believe we see signs of heating, for example broadening, in our results.

XES spectra were computed by use of the Bethe-Salpeter equation as implemented in the OCEAN code. Calculations were performed on various stoichiometries of YH at multiple pressures from 0 to 200GPa. Density functional theory utilizing the Perdew-Burke-Ernzerhof (PBE) exchange-correlation functional via the Quantum Espresso software package was used to calculate the ground state electronic structure and perform ion relaxations for each structure. The SCF calculation was done on a 9x9x9 k-grid while the screening calculation was done on a 3 x 3 x 3 k-grid. Norm-conserving Vanderbilt pseudopotentials provided by the oncvpsp code were used for both Hydrogen and Yttrium and have a valency of 1 electron (1s) and 20 electrons (4p4d5s) respectively. The maximum energy for bands in the final state wave function is set to 150eV above the edge. Ionic optimizations for each structure were first performed at each pressure with symmetry enforced prior to the calculation of spectra.

Yttrium hydride presents itself as a unique binary hydride, as all known changes in hydrogen coordination are accompanied by a change in the cationic sublattice. Furthermore, yttrium has a k-edge of 17.038 keV, far from diamond absorption, and achievable for XES detection at many modern synchrotrons. Yttrium hydride displays a rich stoichiometric morphology, existing in  $\text{YH}_2$ ,  $\text{YH}_3$ ,  $\text{YH}_4$ ,  $\text{YH}_6$ ,  $\text{YH}_9$ , and is predicted, though never observed,

to have a  $\text{YH}_{10}$  stoichiometry. Furthermore,  $\text{YH}_3$ ,  $\text{YH}_4$ ,  $\text{YH}_6$ , and  $\text{YH}_9$  all were predicted to have high  $T_{CS}$  and all have been experimentally observed, with the exception of  $\text{YH}_3$  [183], potentially due to its strong electron-phonon coupling constant (1.5) resulting in instability of soft phonons quenching superconductivity [184, 185]. These attributes make yttrium hydride an ideal candidate to validate these measurements at megabar conditions. Despite ideal conditions crystallographically, published studies in the same pressure regime, using similar methodologies, produce unique results, only furthering the necessity of metrology that that can empirically measure coordination and highlighting the difficulty of synthesizing samples at high-pressures [67, 171].

$K\beta_1$  and  $K\beta_3$ (K-M<sub>2</sub>, K-M<sub>3</sub>) and VTC transition spectra of the  $K\beta_2$  (K-N<sub>2,3</sub>) and  $K\beta''$  emission were collected on the yttrium hydride system and representative spectra can be found in Fig. 4.1.

Collected spectra show good agreement with theoretical calculations, despite OCEAN's reliance on DFT optimization. The intensity in  $\text{YH}_3$  of the  $k\beta''$  sharpens with pressure. This makes XES measurements a promising candidate for high-pressure determination of coordination due to the atypical behavior of quality of data improving with increasing pressures. Background subtracted spectra of the VTC spectra can be found in Appendix C Fig C.2.

VTC transitions are weak due to their lower spatial overlap with the 1s state relative to other core states with significantly larger overlap integrals, resulting in core states dominating the transition probability. In the yttrium metal system, the  $K\beta_3$  emission is a factor five times stronger than the intensity of the  $K\beta_2$  emission. The  $K\beta_1$  and  $K\beta_3$  correspond to core states of the metallic yttrium species and, as such, are not expected to be sensitive to pressure. A figure showing all collected  $K\beta_1$  and  $K\beta_3$  spectra can be found in Appendix C Fig C.3. In contrast, the  $K\beta''$  is a cross-over transition and sensitive to ligand behavior. Relative changes in the intensity occurring with increasing pressure are expected to result in the sharpening of the  $K\beta''$  transition due to the higher spatial overlap corresponding to a decrease in orbital radius<sup>3</sup>. Likewise, shifts in energy can be related to coordination through

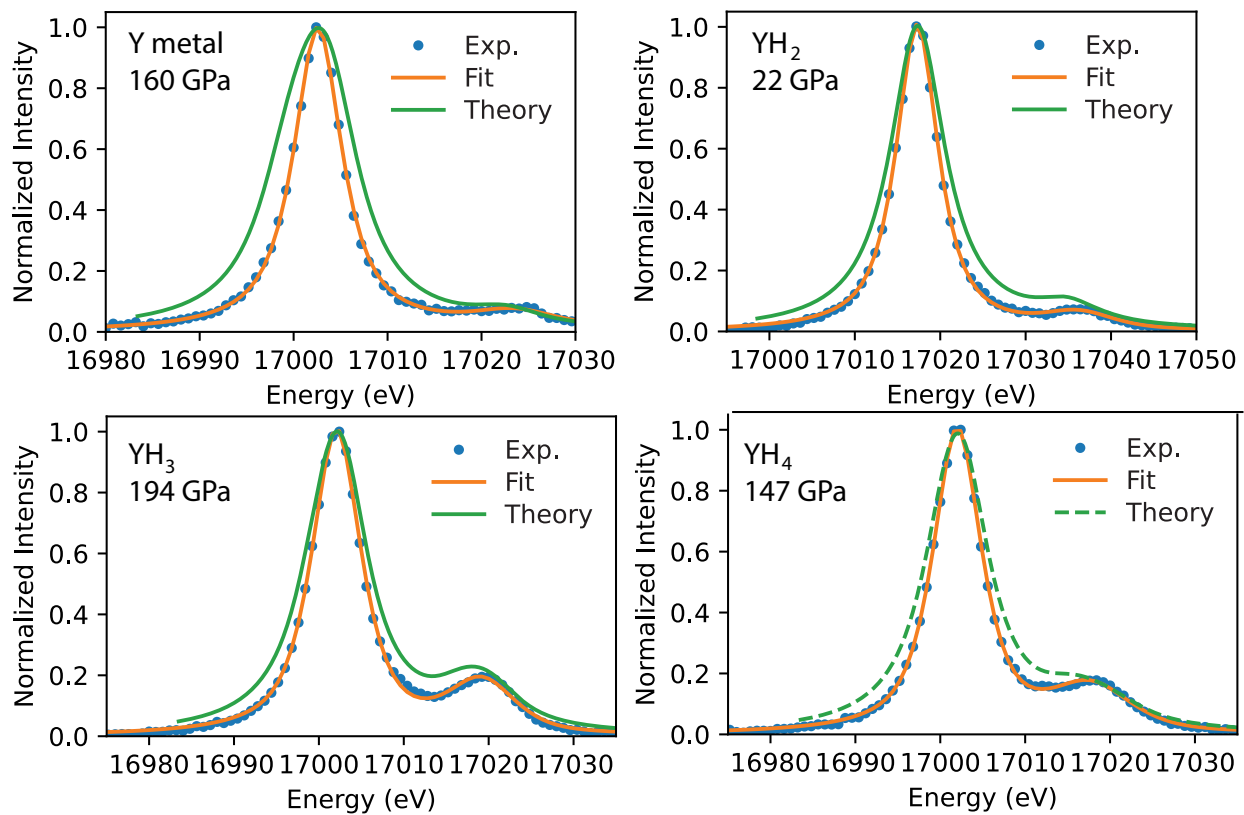


Figure 4.1: A figure showing representative XES spectra of the various experimental data compared to the theoretical OCEAN calculations for all experimentally observed phases of yttrium hydride. Credit: GA Smith, UNLV: XES experiments; Daniel Schacher, UNLV: OCEAN calculations.

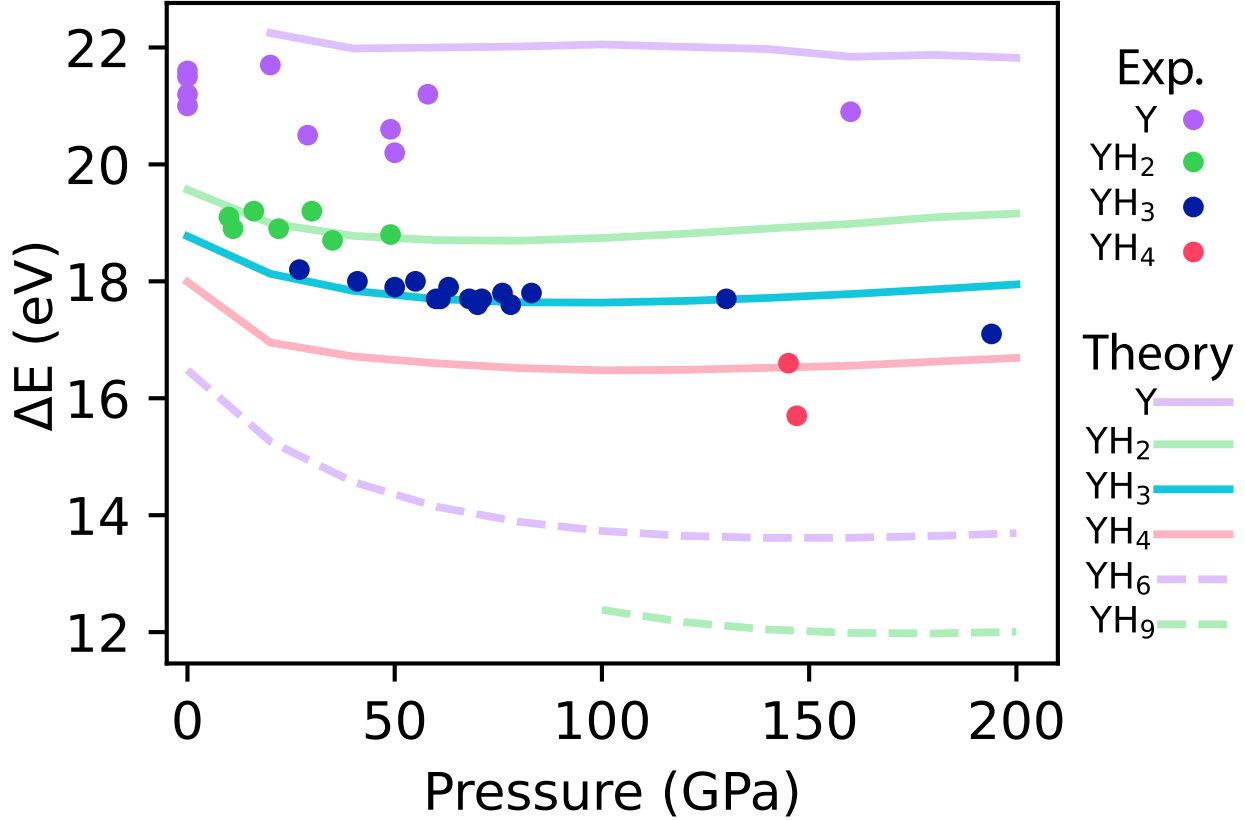


Figure 4.2: The fitted energy difference between the  $k\beta_2$  transition and the  $K\beta''$  transition with respect to pressure. This evolution is sensitive to coordination number, and each line can be assigned a coordination number through theoretical calculations. Theoretical energy axis has been systematically stretched by 7.5% to allow for visualization with experimental data. Credit: GA Smith, UNLV: XES experiments; Daniel Schacher, UNLV: OCEAN calculations.

the correlation of observations of the p-DOS and the expected shift that accompanies changes in stoichiometry.

Fitting the  $K\beta_2$  and  $K\beta''$  allows for tracking of relative changes in both energy and intensity. The results of the difference in energy of the fits is displayed in Fig. 4.2, and shows the differentiation of synthesized Y metal,  $YH_2$ ,  $YH_3$ , and  $YH_4$  up to 194 GPa.

A shift towards lower energy of the peak  $k\beta''$  peak indicates a change in coordination of about an eV per hydrogen formula unit. This agrees well with the theoretical trends despite what appears to be a systematic offset in  $\Delta E$  of 7.5%. Raw spectra can be found in Fig.C.4 created by multiplying the energy of all spectra by some constant before fitting

as is common in other XES works [94] in the SI. The use of Fig. 4.2 should only to be as general trend guide, as agreement beyond is functionally coincidental due to the difficulty DFT has with quantum effects common to hydride materials. Conversion from  $\text{YH}_2$  to  $\text{YH}_3$  was well resolved, showing the sensitivity of XES to integer changes in stoichiometry. At 147 GPa  $\text{YH}_4$  was observed and confirmed with diffraction and shows to be well resolved by XES measurements. The 194 GPa  $\text{YH}_3$  data point shows a generally lower than expected trend in  $\Delta E$  relative to the rest of the  $\text{YH}_3$  spectra. The  $I4/mmm$  data point at 147 GPa shows a lower separation than expected relative to theoretical trends, perhaps implying a fractional stoichiometry between 4 and 6. We believe the reason for these difference can be explained through the diffraction.

Representative XRD patterns confirming the expected phase behavior of yttrium hydride can be found in Fig. 4.3. The 194 GPa  $\text{YH}_3$  data point shows tetragonal distortions in the  $Fm-3m$  structure towards a  $I4/mmm$  structure in  $\text{YH}_3$ , with  $c/a$  ratio of 1.454, larger than the ideal 1.414 value. Volume per formula unit of these two phases are within a tenth of a percent of each other, with the  $I4/mmm$  phase showing a smaller volume. The relative drop in  $\Delta E$  in XES at this point could be due to the tetragonal distortions resulting in a slight change in the partial density of states, though, both the  $Fm-3m$  and  $I4/mmm$  display 14 fold coordination. Observation of  $\text{YH}_3$  in the  $Fm-3m$  phase in this pressure range has been previously reported and diffraction is in line with previous studies. The  $I4/mmm$  has been previously reported to be enthalpically competitive near 190 GPa where theoretical calculations show a difference of less than 0.01 eV per  $\text{YH}_3$  unit with the a  $P21/m$  phase. [186] Two unidentified peaks are present about the 220 reflection. These peaks could be indicative of an  $Fm-3m$  structure as they agree to 111 and 200 peaks, though volumetrically these peaks cannot be attributed to  $\text{YH}$ .

Extended x-ray fine structure (EXAFS) on the sample at 194 GPa radial through the gasket at the Swiss light source (SLS) at the micro XAS beamline to acquire further insight into the observed trend in  $\Delta E$ . Measurements show at 200 GPa, that the yttrium atom



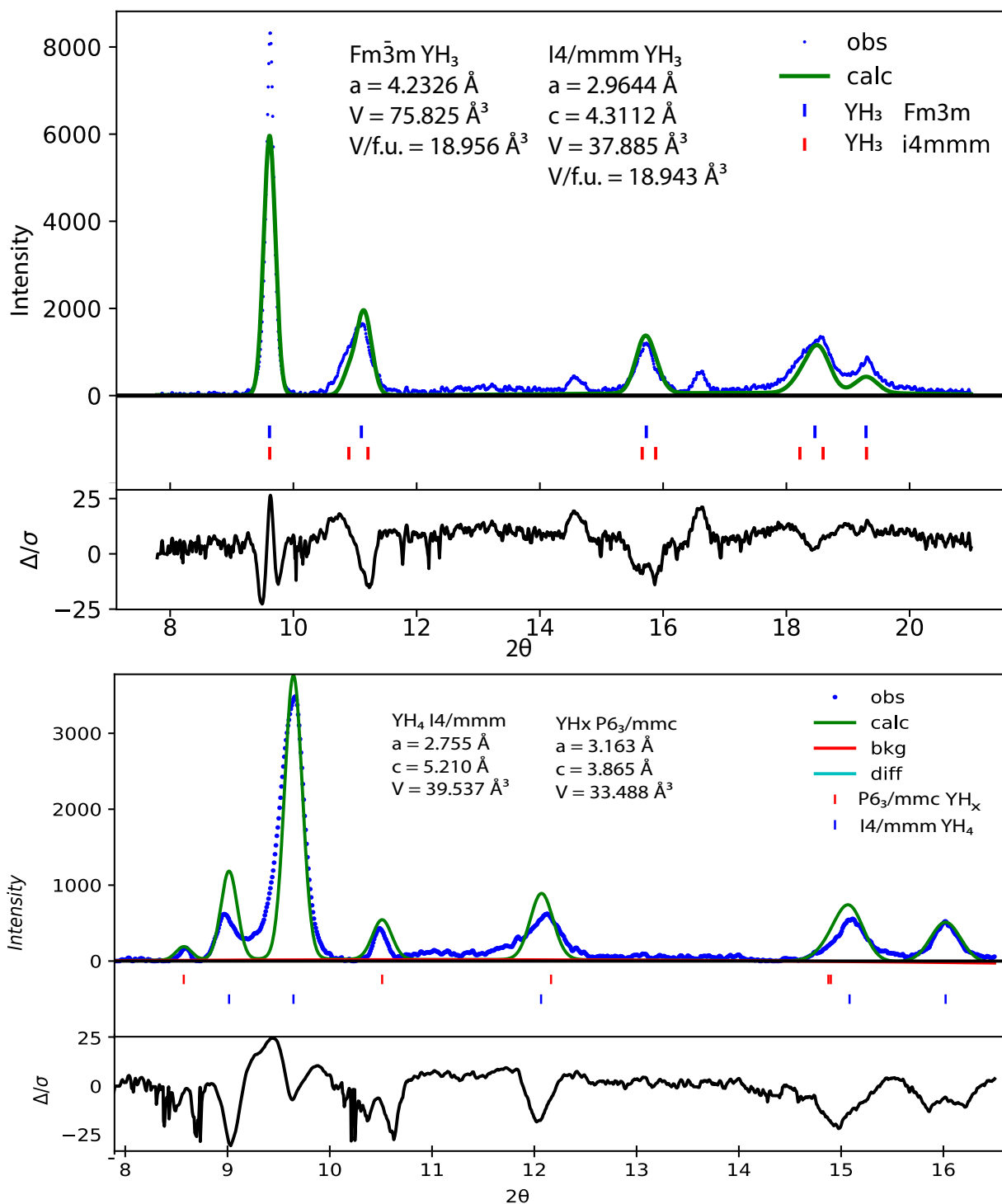


Figure 4.3: a) Rietveld refinement of YH<sub>3</sub> at 194 GPa. Peak splitting of the 200 and 220 peaks show the tetragonal distortions of the Fm-3m structure. b) Rietveld refinement of the YH<sub>4</sub> data point at 147 GPa. We observe a hexagonal phase, of unknown origin. An unidentified phase is marked by asterisks. Credit: GA Smith, Emily Siska UNLV: XRD analysis.

positions begin to deviate from cubic  $\text{YH}_3$  agreeing well that a tetragonal distortion exists. EXAFS fits and spectra can be found in Appendix C Fig. C.1. Perhaps surprisingly for these thermodynamic conditions, the data is EXAFS quality implying it is unlikely that mixed phases of yttrium hydride are present in this sample. This is because EXAFS of mixed phases often disrupts signal resulting in no EXAFS signal, as was observed in the sample that was  $\text{YH}_4$  at 147 GPa. This implies that unaccounted diffraction peaks in the tetragonally distorted  $\text{YH}_3$  are likely not attributed to a yttrium hydride sample, but in the  $\text{YH}_4$  sample likely are.

For the 147 GPa data point we observe two unidentified peaks. In the yttrium hydride system,  $\text{YH}_3$ ,  $\text{YH}_7$ , and  $\text{YH}_9$  all have been theoretically predicted to have hexagonal, or nearly hexagonal phases [186, 171]. The agreement to any of these phases seems unlikely, as the  $c/a$  ratio is very close to 1, which is unlike any of the theoretically predicted hexagonal phases. Still, we observed a less than 10% phase fraction of this phase, assuming hexagonal symmetry, and believe it can be attributed to a  $\text{YH}_{4+}$  stoichiometric phase due to the XES trends we observe and loss of EXAFS signal implying mixed phase existence.

Experimental XRD, XAS, and XES measurements were performed on the  $\text{YH}_x$  system up to 194 GPa. XES was able to distinguish whole integer stoichiometries through 194 GPa, effectively resolving Y,  $\text{YH}_2$ ,  $\text{YH}_3$ , and  $\text{YH}_4$ . New metrological advancements are necessary to quantitatively measure non-integer stoichiometries that have been traditionally overlooked in the search of high-temperature superconductors, such as non-superstoichiometric hydrides, in light of the recent discovery of room-temperature superconductivity in the  $\text{LuH}_3\text{N}_x$  system.

## APPENDIX A

### SUPPLEMENTARY INFORMATION TO THE PREVALENCE OF PRE-TRANSITION OF DISORDERING IN THE RUTILE TO $\text{CaCl}_2$ PHASE TRANSITION OF $\text{GeO}_2$ THE PREVALENCE OF PRE-TRANSITION OF DISORDERING IN THE RUTILE TO $\text{CaCl}_2$ PHASE TRANSITION OF $\text{GeO}_2$

#### A.1 XRD DETERMINED LATTICES

Table A.1: Experimental unit cell parameters ( $\text{\AA}$ ) and volume ( $\text{\AA}^3$ ) measured by XRD as a function of pressure (GPa). The phase at any given pressure was determined by best Rietveld fit and is denoted as either rutile-type ( $P4_2/mnm$ ) or  $\text{CaCl}_2$ -type ( $Pnmm$ ). In the rutile phase  $a=b$ . The errors on the fits are reported for each pressure. Credit: GA Smith, Ashkan Salamat UNLV: XRD experiments.

Pressure (GPa)	Structure	a	b	c	V	wRP	Rp
2.5	Rutile	4.3793(2)		2.8606(3)	54.862(5)	2.10%	0.72%
5.4	Rutile	4.3613(2)		2.8530(3)	54.266(5)	2.40%	1.00%
9.5	Rutile	4.3368(2)		2.8422(4)	53.457(5)	1.94%	0.52%
11.9	Rutile	4.3246(2)		2.8366(3)	53.051(5)	3.10%	0.61%
17.3	Rutile	4.296(2)		2.8239(3)	52.14(5)	2.00%	1.37%
19.7	Rutile	4.2863(3)		2.8190(3)	51.792(5)	2.02%	1.14%
21.5	Rutile	4.2782(2)		2.8155(3)	51.532(5)	1.40%	1.00%
23.5	Rutile	4.2741(3)		2.8131(4)	51.389(5)	1.90%	1.20%
25.4	Rutile	4.2631(5)		2.8088(4)	51.05(2)	3.60%	1.80%
26.4	Rutile	4.259(4)		2.8075(4)	50.93(1)	1.20%	1.00%
28.0	Rutile	4.253(4)		2.8040(4)	50.72(1)	2.12%	2.01%
29.6	$\text{CaCl}_2$	4.265(1)	4.225(1)	2.799(1)	50.42(1)	1.97%	1.67%
31.4	$\text{CaCl}_2$	4.261(1)	4.215(1)	2.797(1)	50.25(1)	2.45%	2.21%
33.7	$\text{CaCl}_2$	4.2635(3)	4.2051(3)	2.7923(5)	50.06(4)	2.60%	1.80%

Table A.2: The refined oxygen fractional coordinates and Ge-O bond lengths for the rutile and CaCl<sub>2</sub> phases. In the rutile ( $P4_2/mnm$ , 136) structure the Ge is on the 2a (0,0,0) Wyckoff site and the oxygen is on the 4f (u,u,0) site. In the CaCl<sub>2</sub> ( $Pn\bar{1}m$ , 58) structure the Ge is on the 2a (0,0,0) Wyckoff site and the oxygen is on the 4g (u,v,0) site. Credit: GA Smith, Ashkan Salamat, UNLV: XRD analysis

P	Structure	u	v	Basal (Å)	Axial (Å)
2.5	Rutile	0.325(2)		1.794(2)	2.013(2)
5.4	Rutile	0.324(2)		1.791(2)	2.000(2)
9.5	Rutile	0.323(2)		1.788(3)	1.982(3)
11.9	Rutile	0.322(2)		1.788(3)	1.969(3)
17.3	Rutile	0.320(1)		1.790(3)	1.938(3)
19.7	Rutile	0.319(2)		1.787(3)	1.933(3)
21.5	Rutile	0.311(1)		1.816(3)	1.879(3)
23.5	Rutile	0.309(2)		1.819(3)	1.868(3)
25.4	Rutile	0.316(2)		1.790(2)	1.905(2)
26.4	Rutile	0.309(2)		1.816(3)	1.860(2)
28.0	Rutile	0.307(2)		1.820(3)	1.846(3)
29.6	CaCl <sub>2</sub>	0.305(2)	0.314(2)	1.808(4)	1.858(4)
31.4	CaCl <sub>2</sub>	0.301(2)	0.321(2)	1.800(4)	1.870(4)
33.7	CaCl <sub>2</sub>	0.303(2)	0.323(2)	1.789(4)	1.880(4)

## A.2 1st-SHELL EXAFS FITS

Figure A.8 Shows the results from fitting the EXAFS data to the first octahedra of GeO<sub>2</sub> with a one shell model. The MSRD of the one shell fit appear in a) and are lower than the MSRDs obtained through the 2 shell fits. In b) the bond lengths obtained from the 2 shell fit are lower than that of only fitting the first shell. These discrepancies are likely due to an incomplete description of the system through a smaller R window being used to only fit the first shell and the system attributing the contributions of the second shell to the values determined in only the first oxygen shell fit.

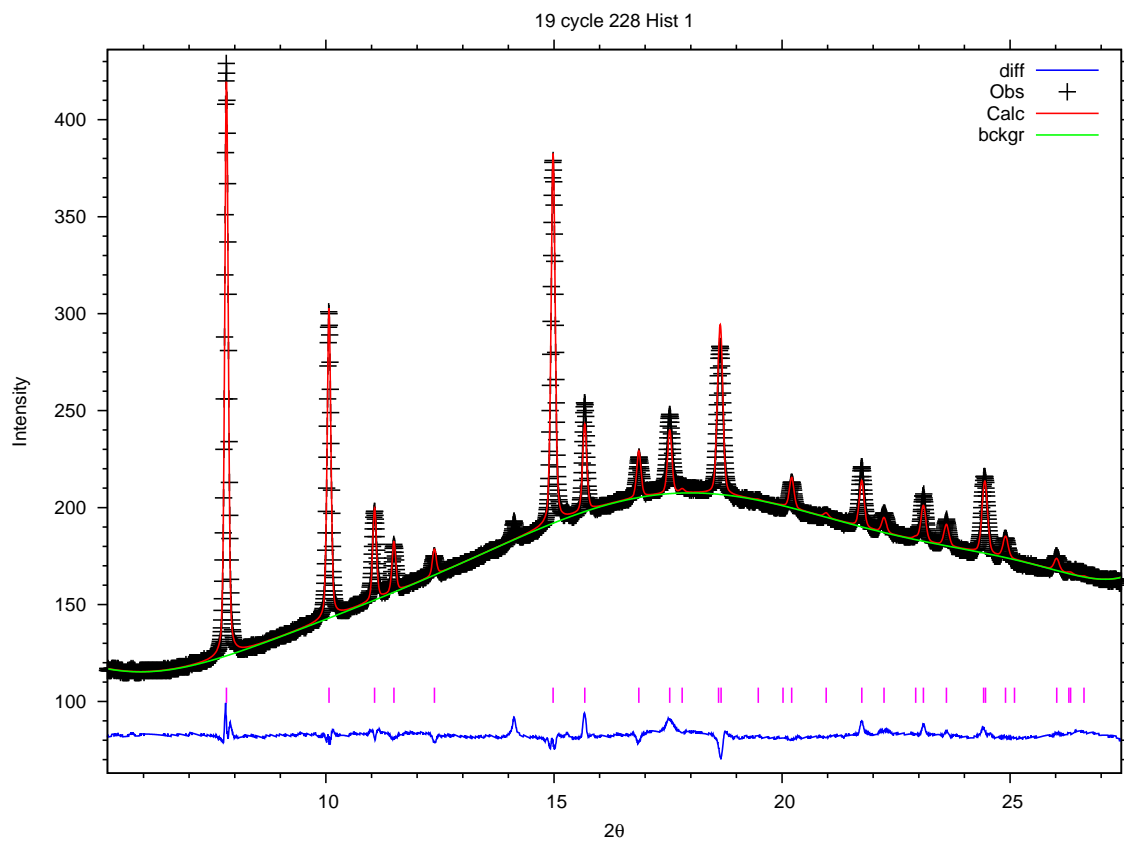


Figure A.1: The Rietveld refinement for the 19 GPa XRD point. Credit: GA Smith, Ashkan Salamat UNLV: XRD experiments.

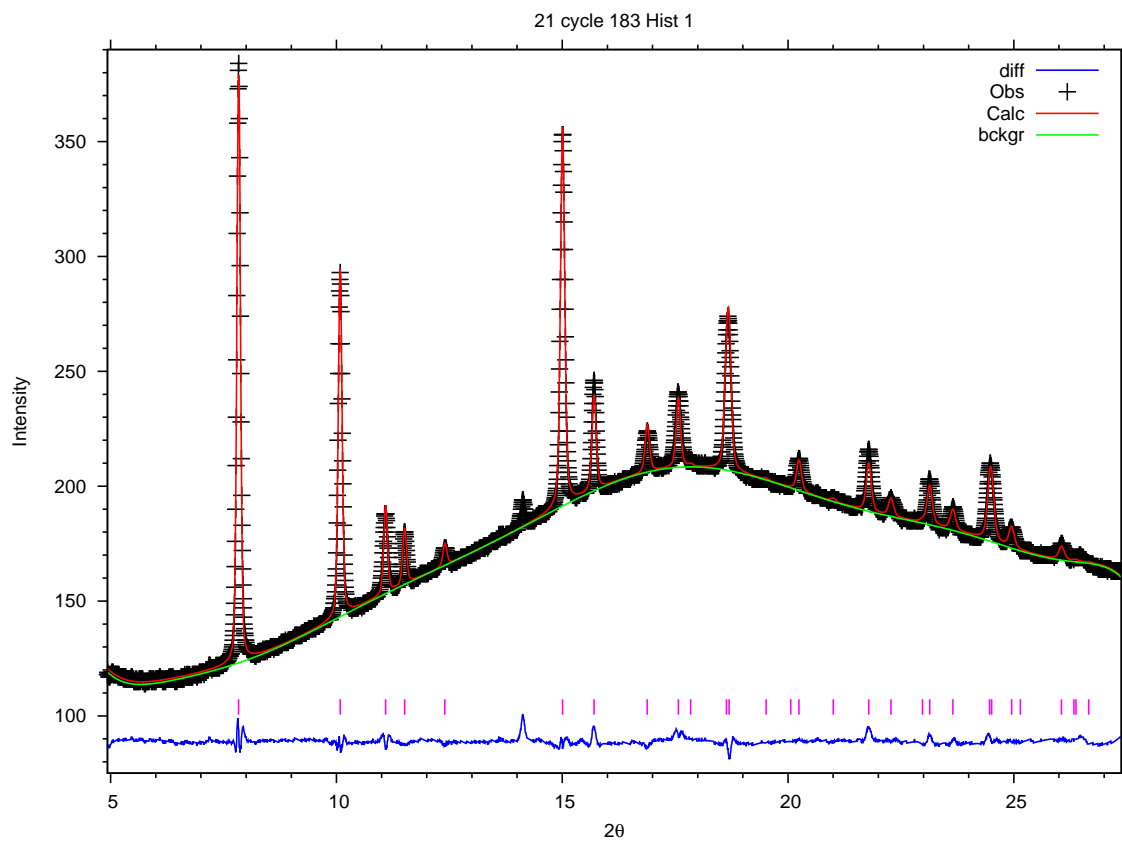


Figure A.2: The Rietveld refinement for the 21 GPa XRD point. Credit: GA Smith, Ashkan Salamat UNLV: XRD experiments.

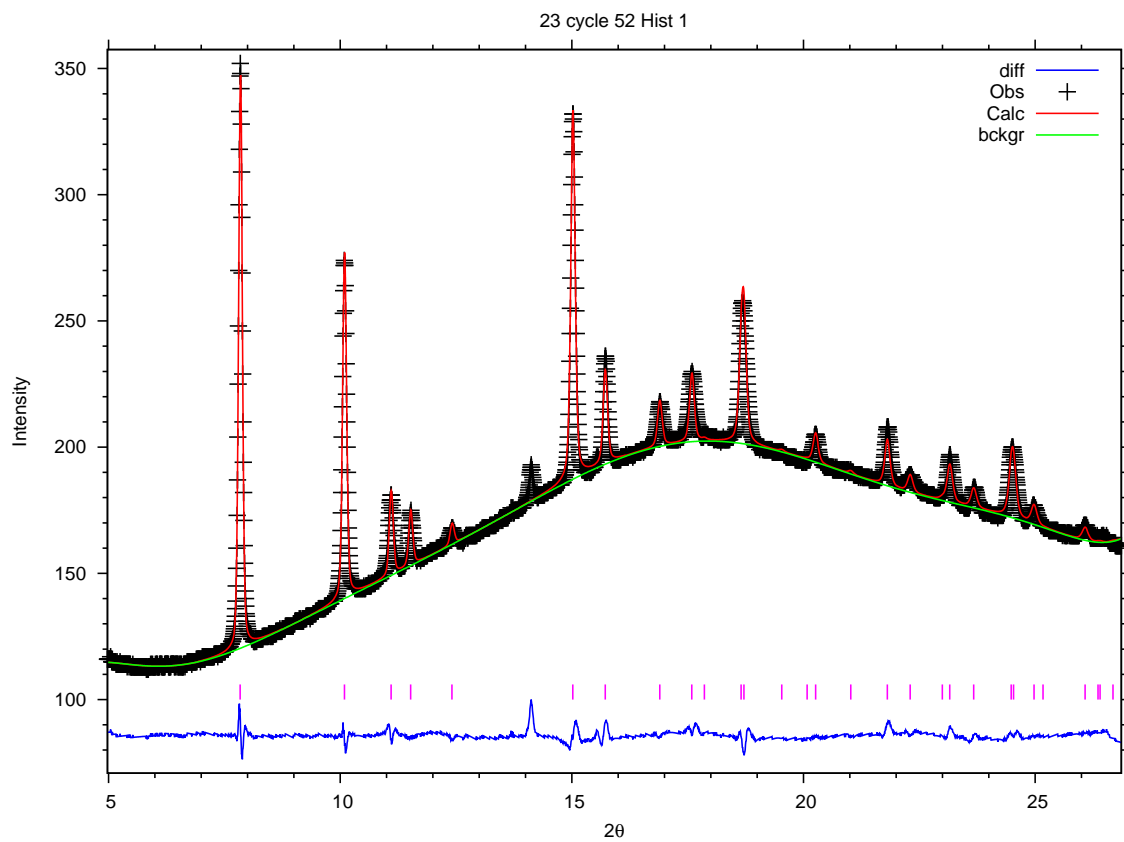


Figure A.3: The Rietveld refinement for the 23 GPa XRD point. Credit: GA Smith, Ashkan Salamat UNLV: XRD experiments.

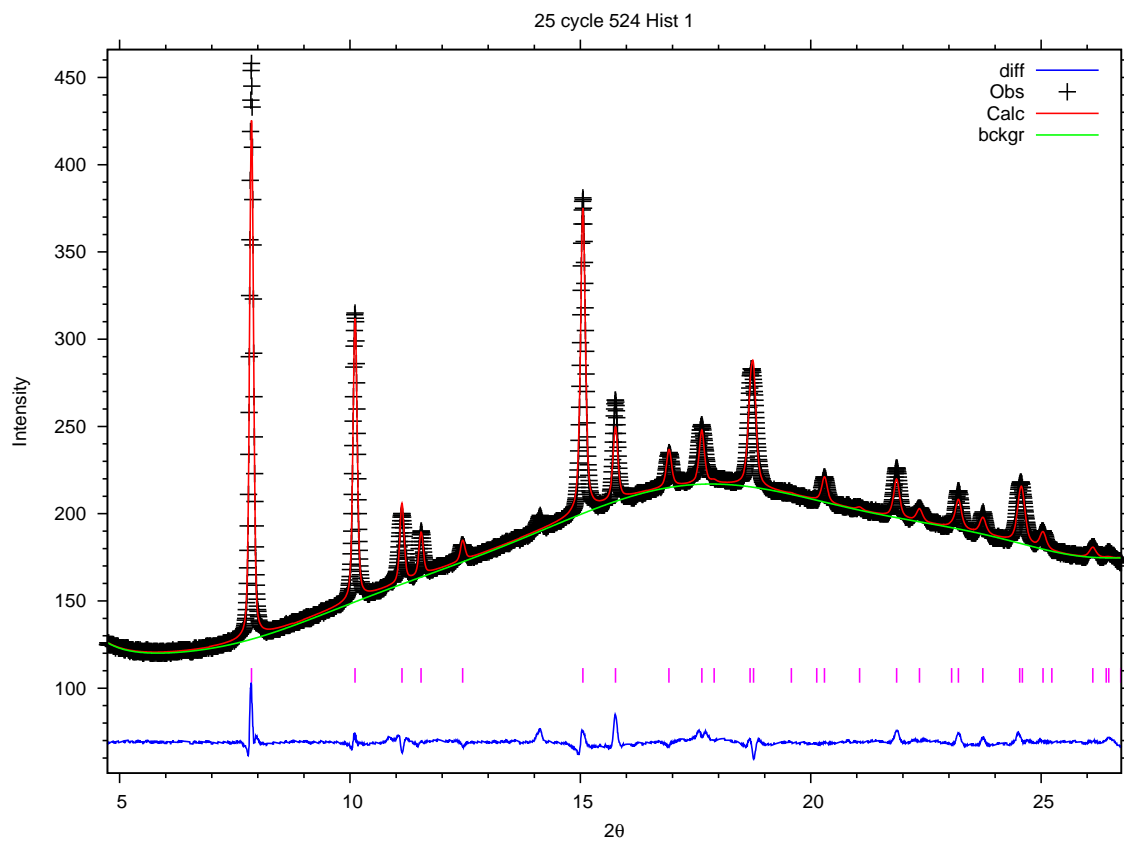


Figure A.4: The Rietveld refinement for the 25 GPa XRD point. Credit: GA Smith, Ashkan Salamat UNLV: XRD experiments.



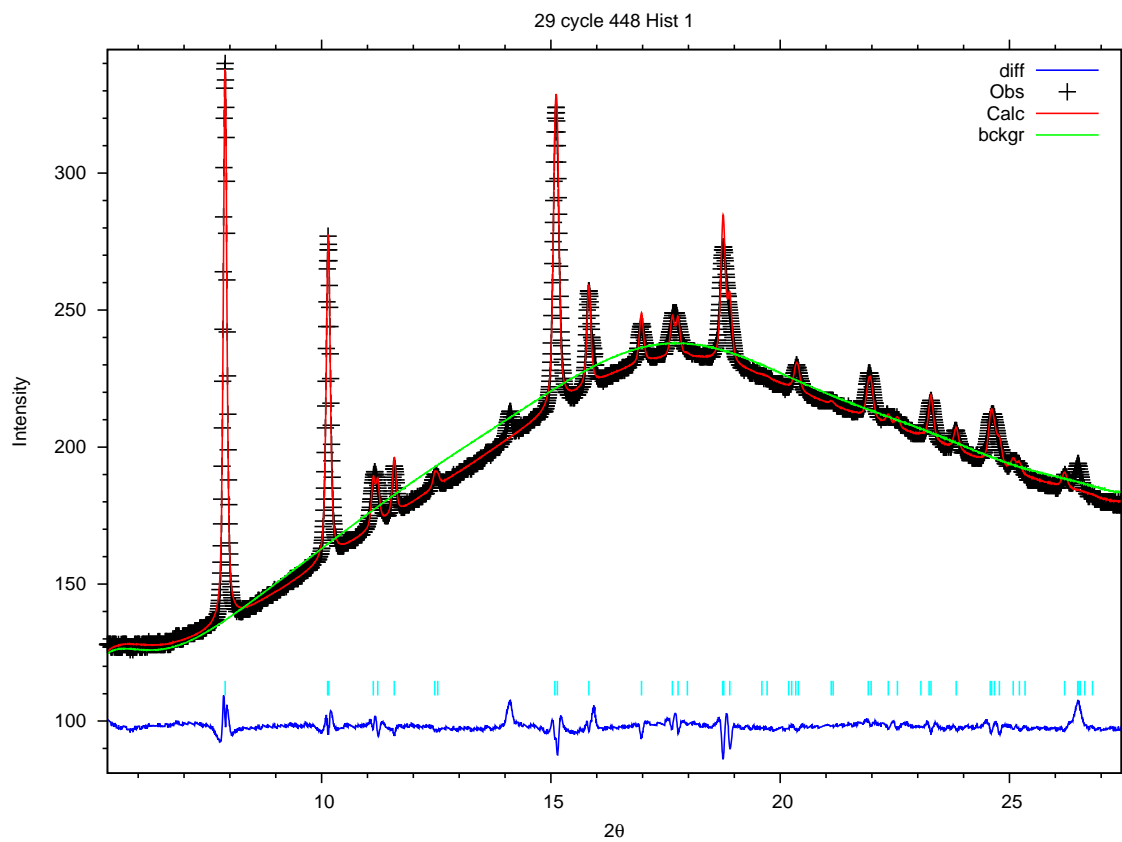


Figure A.5: The Rietveld refinement for the 29 GPa XRD point. Credit: GA Smith, Ashkan Salamat UNLV: XRD experiments.

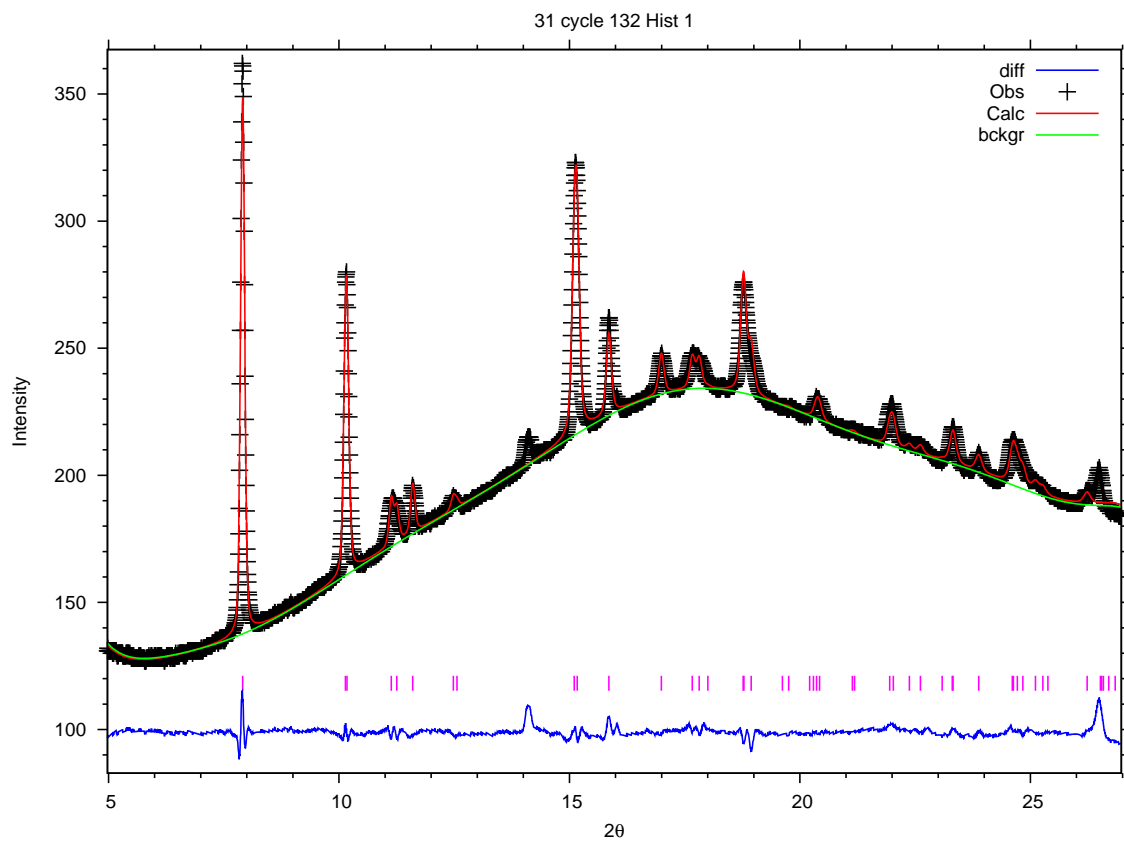


Figure A.6: The Rietveld refinement for the 31 GPa XRD point. Credit: GA Smith, Ashkan Salamat UNLV: XRD experiments.

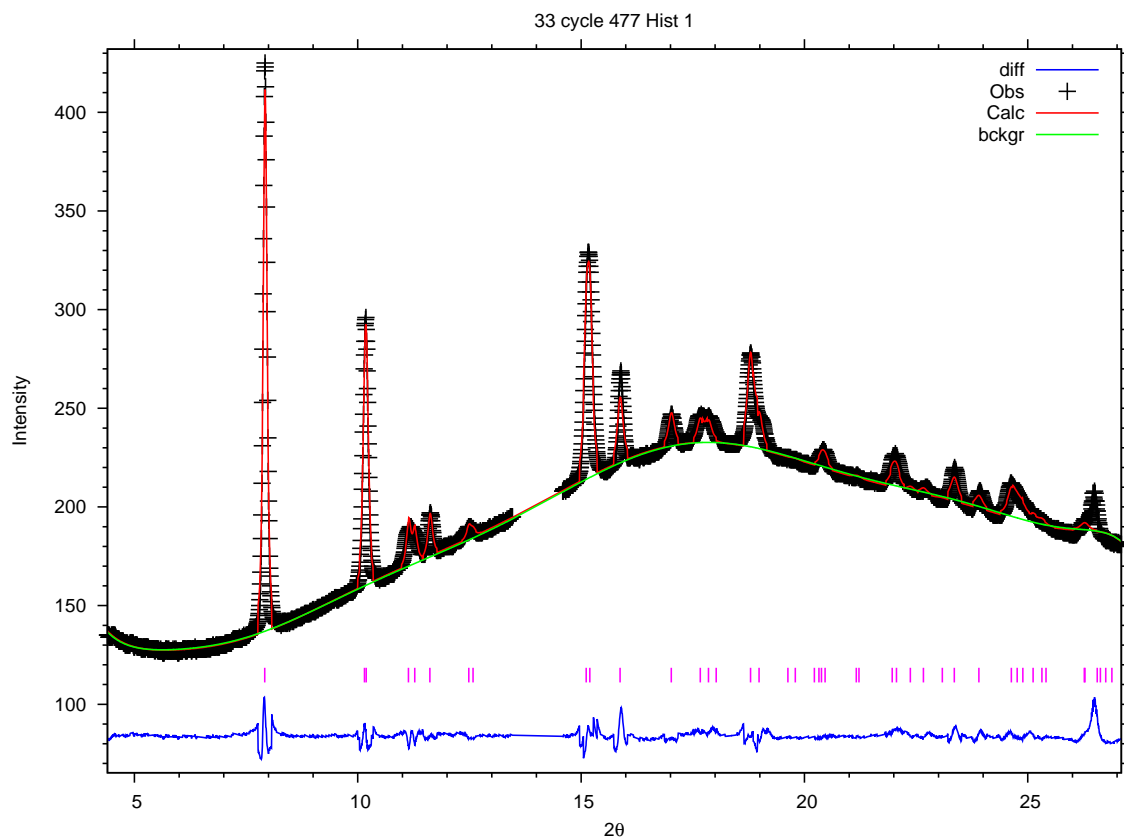


Figure A.7: The Rietveld refinement for the 33 GPa XRD point. Credit: GA Smith, Ashkan Salamat UNLV: XRD experiments.

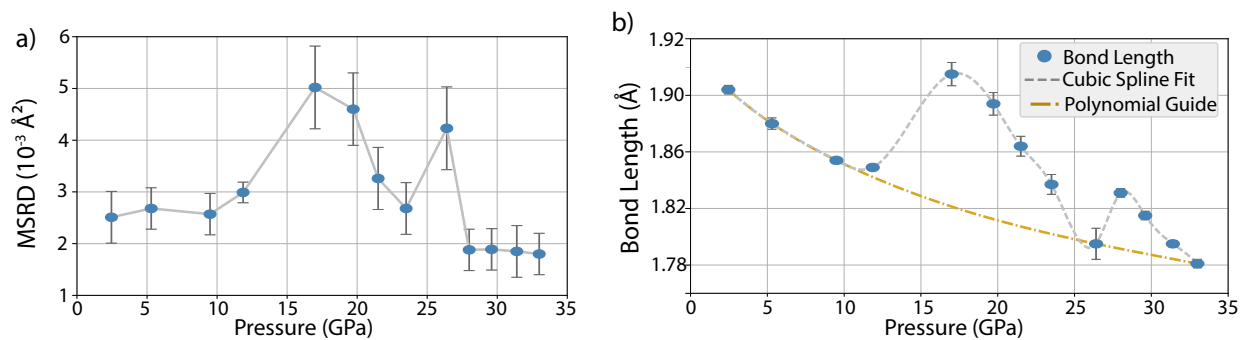


Figure A.8: EXAFS fits of the 1st shell of  $\text{GeO}_2$ . a) the MSR D as determined from fitting the first oxygen octahedral. b) The experimentally determined bond length of the first shell. Credit: GA Smith, Daniel Sneed UNLV: XAS experiments.

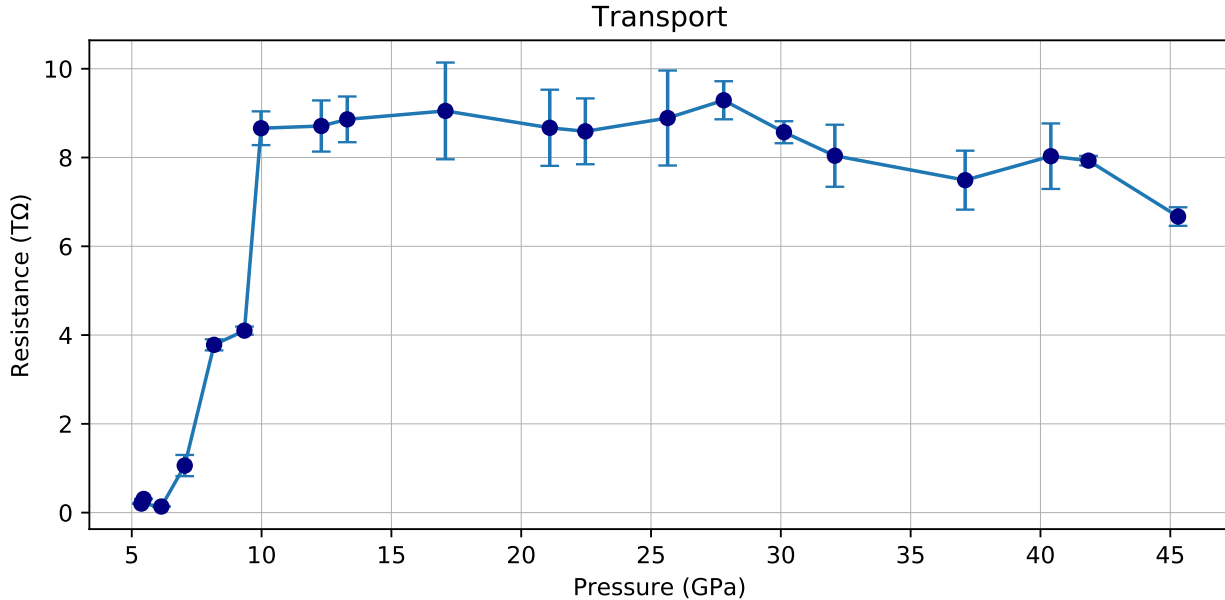


Figure A.9: Transport Data with no laser excitation, Resistance in tera-ohms is plotted against pressure. Around 10 GPa we reach our limit of detection of about 8.5 TΩ and believe all further measurements are unreliable past this pressure. Credit: GA Smith UNLV: High-pressure resistance experiments.

### A.3 TRANSPORT MEASUREMENTS

Experimentally, the most obvious method of observing the postulated anomalous conductivity behavior is using traditional high-pressure electron transport measurements. However, performing these measurements on an ultra-wide bandgap UWBG semiconductor like rutile  $\text{GeO}_2$  is prohibitively difficult due to the nature of the 4.68 eV wide bandgap, but it would be remiss not to attempt such measurements. Transport measurements were conducted using four  $4 \mu\text{m}$  thick platinum probes insulated from a rhenium gasket using  $\text{Al}_2\text{O}_3$  powder, which also served as a PTM for transport measurements. Currents on the order of picoamps were measured by placing the prepared DAC in a Faraday cage and using an optometer in series with the sample.

Figure A.9 shows how the resistance of  $\text{GeO}_2$  responds to the in-situ applied pressure from the DAC. The initial resistance measured for rutile  $\text{GeO}_2$  is 0.31 tera-ohms at 5.5 GPa. A sharp increase of resistance occurs from 5 GPa to 10 GPa where the resistance becomes too

large to measure for our given probe at 8.66 T- $\Omega$ . The increase of Resistance with function of pressure is directly correlated to the expected pressure tunable opening of the bandgap for such oxides from the degree of ionicity increasing with pressure. Despite the predicted drop in band gap in the pre-transition disordered state, as was observed in SnO<sub>2</sub>, we do not see a response. This indicates that if a drop in resistance occurred, the resistance at 30 GPa is still greater than the sensitivity of measurement technique. Photocurrent measures were also performed by shining laser light at  $E_g/2$ , however, results did not produce a measurable reading within the limit of detection of multimeter.

## A.4 THEORY

Presented below are extended calculations.

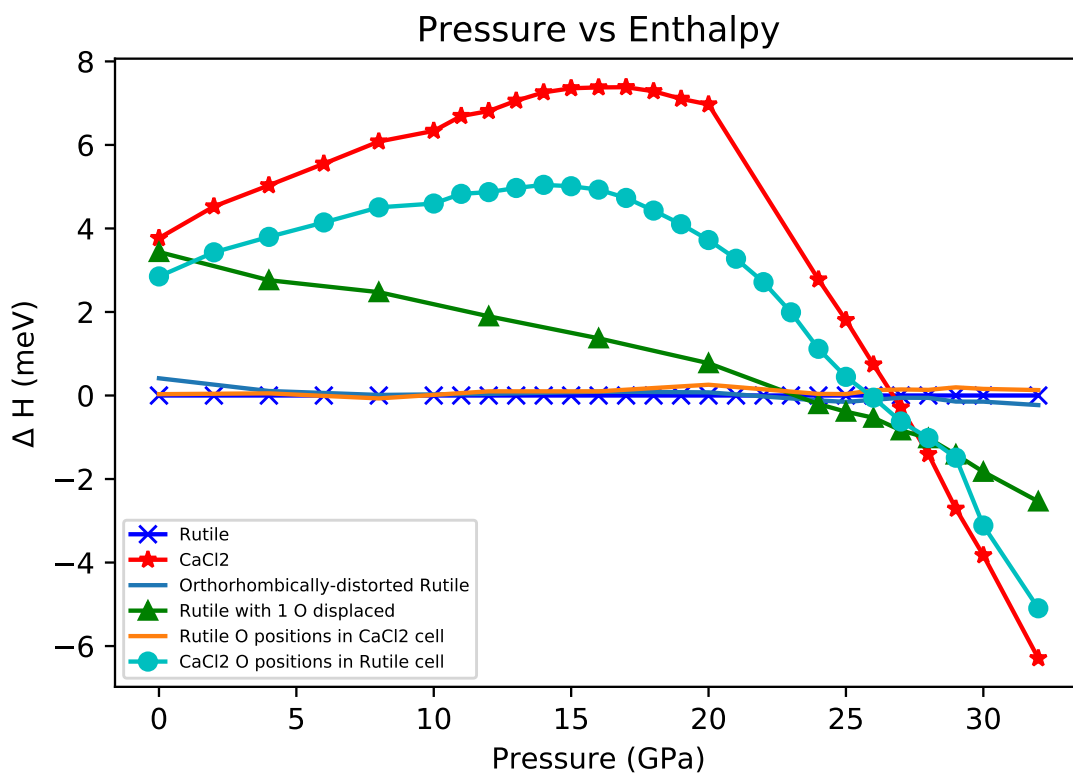


Figure A.10: Enthalpy per  $\text{GeO}_2$  unit cell as a function of pressure for the rutile,  $\text{CaCl}_2$ , manually orthorhombically-distorted rutile, rutile with a single oxygen displaced, and the rutile and  $\text{CaCl}_2$  structures with their oxygen positions swapped. The enthalpies are normalized with respect to the rutile phase. Credit: Daniel Schacher, Keith Lawler UNLV: Theory.

Table A.3: DFT unit cell volumes ( $\text{\AA}^3$ ) and Ge–O bond lengths ( $\text{\AA}$ , both axial and basal) as a function of pressure (GPa) for the rutile phase. Credit: Daniel Schacher, Keith Lawler UNLV: Theory.

Pressure	Volume	Ge–O Axial	Ge–O Basal	Average	Difference
0.0	56.0391	1.9072	1.8823	1.8906	0.0249
4.0	55.2292	1.8924	1.8781	1.8828	0.0144
8.0	54.4953	1.879	1.8721	1.8744	0.0069
12.0	53.8298	1.8679	1.8668	1.8672	0.0011
16.0	53.2049	1.8577	1.8617	1.8604	0.004
20.0	52.6229	1.8483	1.8567	1.8539	0.0084
21.0	52.4823	1.846	1.8554	1.8523	0.0094
22.0	52.3437	1.8438	1.8542	1.8507	0.0104
23.0	52.2071	1.8417	1.853	1.8492	0.0113
24.0	52.0536	1.8397	1.8513	1.8474	0.0117
25.0	51.9250	1.8376	1.8502	1.846	0.0127
26.0	51.7988	1.8355	1.8491	1.8446	0.0136
27.0	51.6752	1.8334	1.848	1.8432	0.0146
28.0	51.5523	1.8315	1.8469	1.8418	0.0154
29.0	51.4351	1.8294	1.846	1.8405	0.0165
30.0	51.3185	1.8275	1.845	1.8391	0.0175
32.0	51.0605	1.8238	1.8423	1.8362	0.0185
34.0	50.8370	1.8199	1.8405	1.8336	0.0206
36.0	50.5916	1.8166	1.8378	1.8307	0.0213
38.0	50.3665	1.8132	1.8356	1.8281	0.0224
40.0	50.1470	1.81	1.8333	1.8256	0.0234

Table A.4: DFT unit cell volumes ( $\text{\AA}^3$ ) and Ge–O bond lengths ( $\text{\AA}$ , both axial and basal) as a function of pressure (GPa) for the  $\text{CaCl}_2$  phase. Credit: Daniel Schacher, Keith Lawler UNLV: Theory.

Pressure	Volume	Ge–O Axial	Ge–O Basal	Average	Difference
0.0	56.0528	1.9076	1.8823	1.8908	0.0253
4.0	55.2261	1.8934	1.877	1.8825	0.0164
8.0	54.4662	1.8808	1.8722	1.8751	0.0086
12.0	53.7637	1.8691	1.8669	1.8677	0.0022
16.0	53.0931	1.8618	1.8616	1.8616	0.0002
20.0	52.4481	1.8523	1.8565	1.8551	0.0042
24.0	51.8909	1.8436	1.8516	1.8489	0.0081
25.0	51.7529	1.8414	1.8505	1.8475	0.0091
26.0	51.6215	1.8394	1.8493	1.846	0.0099
27.0	51.4834	1.8374	1.8479	1.8444	0.0105
28.0	51.3685	1.8356	1.847	1.8432	0.0115
29.0	51.2438	1.8334	1.8459	1.8417	0.0125
30.0	51.1273	1.8315	1.8449	1.8404	0.0134
32.0	50.8701	1.8279	1.8422	1.8375	0.0143
34.0	50.6467	1.824	1.8405	1.835	0.0165
36.0	50.3987	1.8207	1.8378	1.8321	0.0171
38.0	50.1730	1.817	1.8359	1.8296	0.0189
40.0	49.9524	1.8136	1.8338	1.8271	0.0202



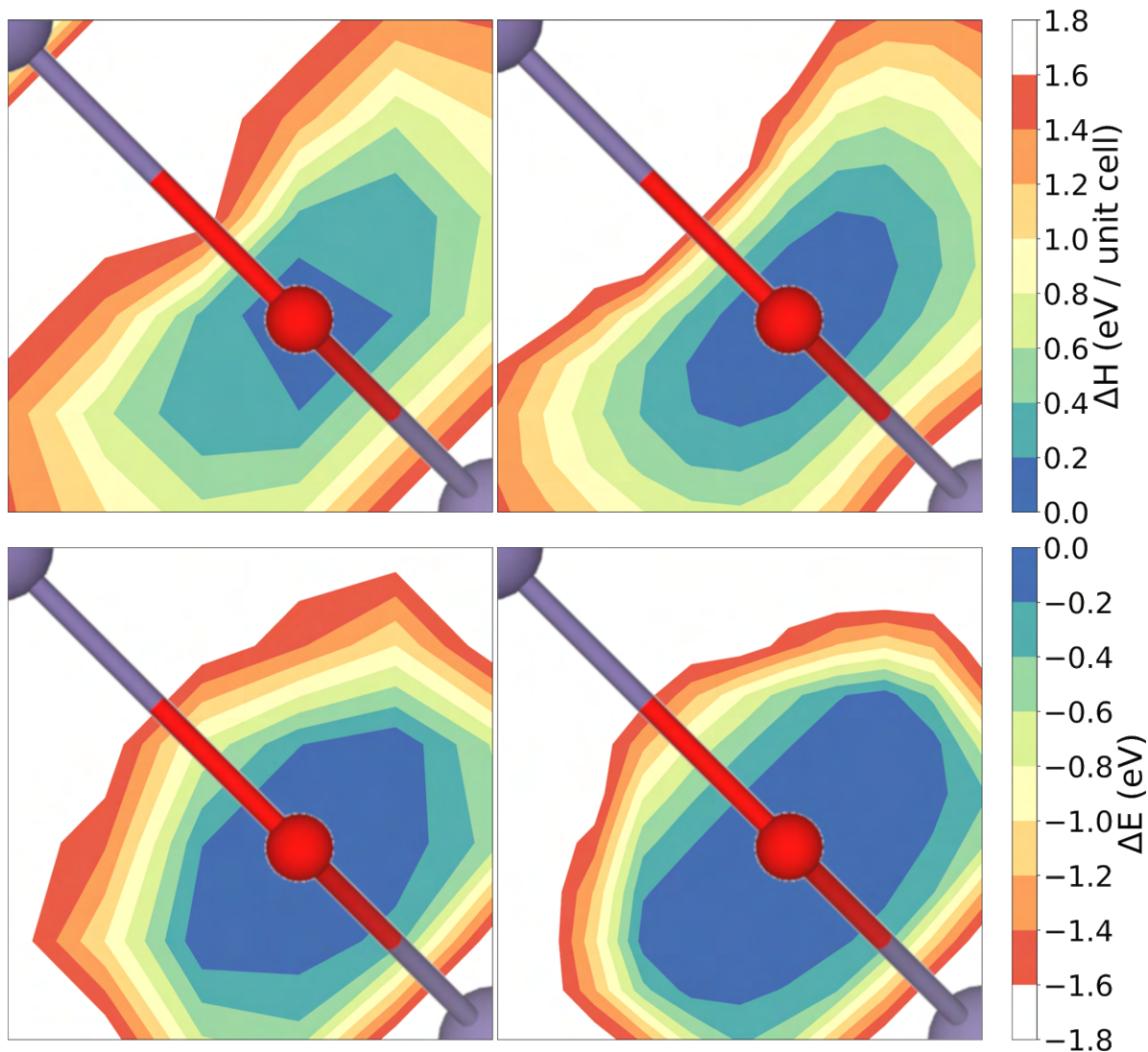


Figure A.11: The response in (top) enthalpy and (bottom) band gap associated with displacing an oxygen in the  $ab$ -plane of a  $2 \times 2 \times 2$  rutile supercell of  $\text{GeO}_2$  at 20 GPa (left) and 25 GPa (right). Credit: Daniel Schacher, Keith Lawler UNLV: Theory.

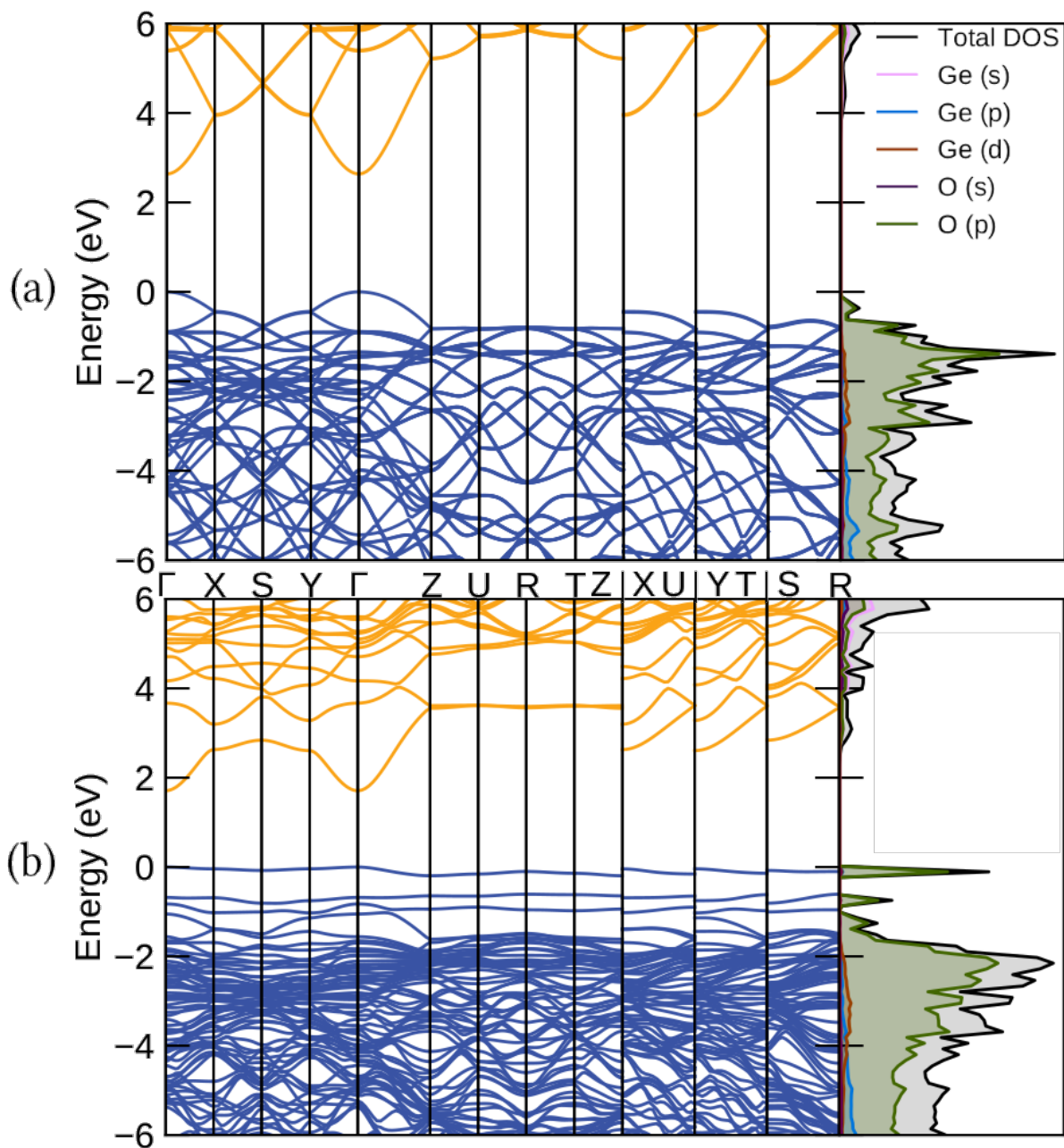


Figure A.12: The band structure and projected density of states for a 25 GPa  $2 \times 2 \times 2$  supercell of (top) pristine rutile  $\text{GeO}_2$  and (bottom) rutile  $\text{GeO}_2$  with a single  $31^\circ$  oxygen displacement. Credit: Daniel Schacher, Keith Lawler UNLV: Theory.

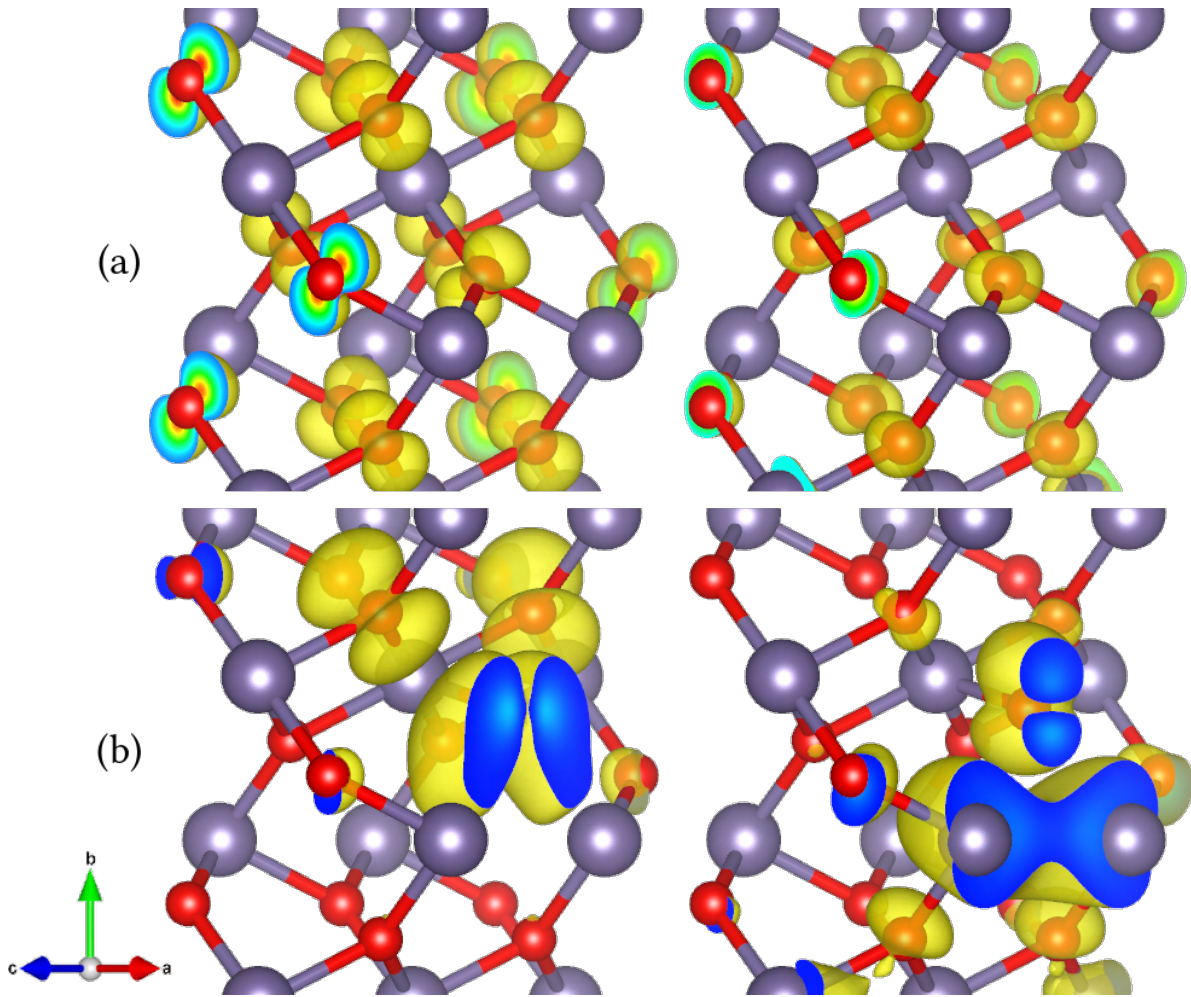


Figure A.13: Band decomposed charge densities for the (top) valence band maximum and (bottom) conduction band minimum for a 25 GPa  $2 \times 2 \times 2$  supercell of (left) pristine rutile  $\text{GeO}_2$  and (right) rutile  $\text{GeO}_2$  with a single  $31^\circ$  oxygen displacement. All isosurfaces are at  $0.001 e/a_0^3$  and show only the relevant portion of the supercell. Credit: Daniel Schacher, Keith Lawler UNLV: Theory.

## APPENDIX B

### SUPPLEMENTARY INFORMATION TO CARBON CONTENT DRIVES HIGH TEMPERATURE SUPERCONDUCTIVITY IN A CARBONACEOUS SULFUR HYDRIDE BELOW 100 GPa

#### B.1 C-S-H SYNTHESIS

We conducted an independent study to that of [3], with the synthesis of 11 crystals of C-S-H carried out at UNLV. Boehler-Almax design diamonds with 80° apertures were used in conjunction with modified BX90 style cells to enable a higher degree of completeness in the acquisition of SC-XRD data. Each cell was prepared using Re foil as a gasket material, which was preindented to a 10th of the culet diameter, confirmed using interferometry, and a sample chamber made by laser micromachining. A sample of a ball-milled mixture of elemental carbon and sulfur with dimensions about 15% of the diamond culet was placed into the sample chamber, as well as a ruby sphere to accurately determine pressures below 10 GPa.[173] Gas-phase H<sub>2</sub> was loaded at 3 kbar.[174] Samples were then pressurized to 3.7–4.0 GPa and excited for several hours using a 514 nm laser with power ranging from 10 and 150 mW depending on sample response. As the sulfur bond is photochemically cleaved using green laser, the sample will begin to appear transparent, after this point sulfur will have a tendency to form the van der Waal crystal. At this point focusing higher powered laser on the carbon sample for several hours, often overnight at the highest available power available, to warm carbon in a liquid hydrogen medium will help react carbon into the CSH crystal. After pressing above the solidification of hydrogen, rapid small crystal formation will grow. At this stage the crystal is still sensitive to higher laser powers and can be manipulated, albeit, they are much less volatile, to help place and form a single crystal. Without unreacted

carbon, leads, or ruby in the chamber, it is often very difficult to place the crystal in an ideal position. After synthesis crystals were pressed to about 10 GPa to ensure stability during Raman. Raman spectroscopy was used to confirm the transformation into CSH *via* the previously reported C-H, S-H, and H-H Raman modes at  $\sim 4$  GPa.[3]

## B.2 EXPERIMENTALLY DETERMINED BIRCH-MURNAGHAN EQUATION OF STATE FITS

Presented below are the fit parameters for the 2<sup>nd</sup>-order Birch-Murnaghan equation of state.

Table B.1: The fit parameters of the 2<sup>nd</sup> Order Birch-Murnaghan equation of state fits. Phase III/IV contributions were determined from fits to both crystals 3 and 4 from Run X2. Credit: GA Smith, UNLV, Ines Collings: EoS analysis.

Run X1	Crystal	$K_0$ (GPa)	$V_0$ ( $\text{\AA}^3$ )
	1	8.39	434.76
	2	10.02	412.80
	3	7.32	448.69
	Phase I	1.32	761.55
	Phase II	11.67	395.96
	All	8.40	433.16
Run X2	Crystal	$K_0$ (GPa)	$V_0$ ( $\text{\AA}^3$ )
	1	13.75	377.29
	2	13.19	377.60
	3	14.50	372.87
	4	13.08	378.77
	Phase I	1.01	791.54
	Phase II	17.31	349.00
	Phase III/IV	21.32	331.31
	All	13.09	380.68
Full Data Set		$K_0$ (GPa)	$V_0$ ( $\text{\AA}^3$ )
	Phase I	6.32	464.21
	Phase II	4.86	504.29
	Phase III/IV	21.32	331.31
	All	11.32	397.54
SH <sub>3</sub>	Crystal	$K_0$ (GPa)	$V_0$ ( $\text{\AA}^3$ )
	all	11.44	399.75

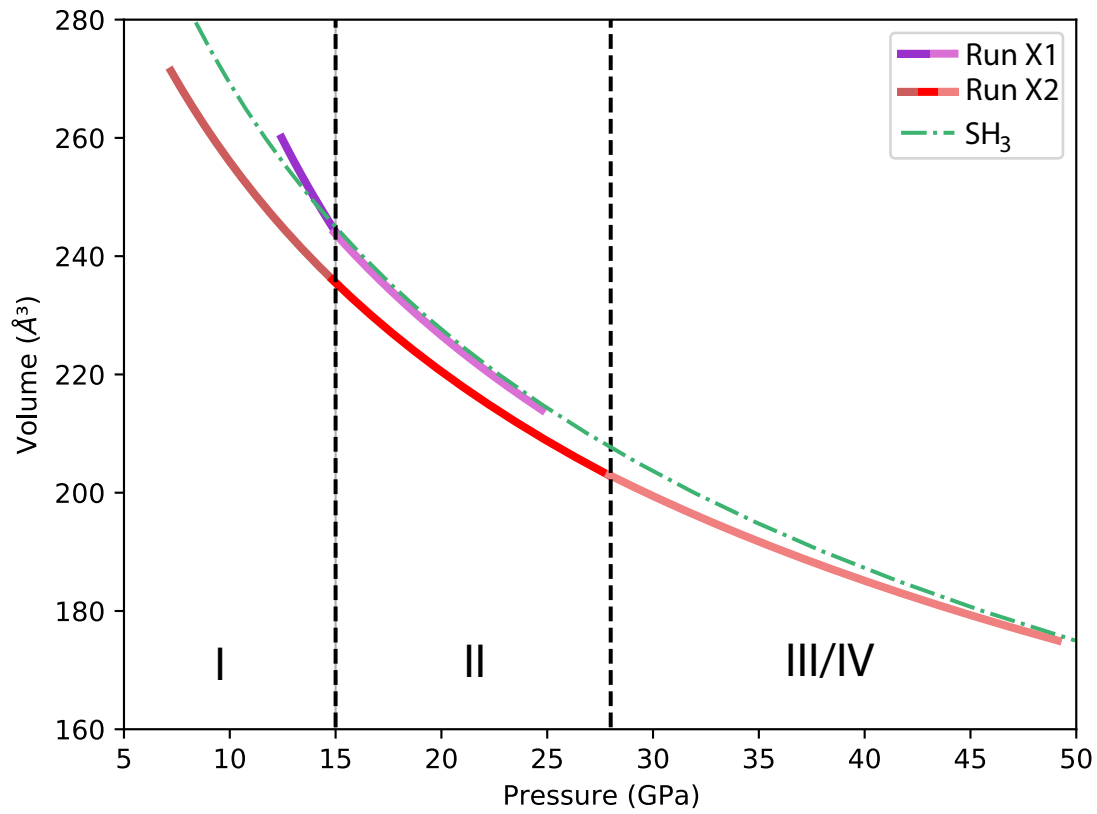


Figure B.1: A plot of the representation of fitted results. Plotted results are presented from first measured point to the either the next phase or highest pressure for a given run. The presented phase boundaries are from the boundaries determined from SC-XRD in this work. Credit: GA Smith, UNLV, Ines Collings: EoS analysis.

### B.3 SC-XRD DETERMINED STRUCTURES

Single-crystal X-ray diffraction experiments were performed at the HPCAT beamline using monochromatic X-rays with the wavelength of 0.3445 Å. The X-ray beam was focused to 2.4 μm by 6.4 μm. Diffraction images were collected using a Pilatus 1M detector detector. The beamline parameters were calibrated with CeO<sub>2</sub> powder and an enstatite single crystal using the programs Dioptas and CrysAlisPro, respectively.[187, 188] Data collections were performed using step scans of 0.5° with 3-5 s exposure over a total ω scan range of ±30° (DAC1) and ±35° (DAC2) about the vertical axis of the DAC. The lattice parameters and the integrated intensities of the Bragg reflections were obtained from the measured images using the program CrysAlisPro.[188] The crystal structures of CSH were solved using direct methods implemented in the SHELXT program.[189] The iterative structure refinements were performed with the SHELXL program[190] built in the ShelXle graphical user interface.[191] Details on the crystal structure refinements are given in Tables SB.6-B.18. Three (CH<sub>4</sub>)<sub>x</sub>(H<sub>2</sub>S)<sub>2-x</sub>H<sub>2</sub> loadings (DAC1, DAC2, and DAC4) used in this study, and a (H<sub>2</sub>S)<sub>2</sub>H<sub>2</sub> loading (DAC3) are shown in Figure SB.2. Figures SB.3-B.9 show the reciprocal space reconstructions for the different crystals in the four loadings. These highlight that the crystal quality can vary, as well as the occurrence of the monoclinic distortion.

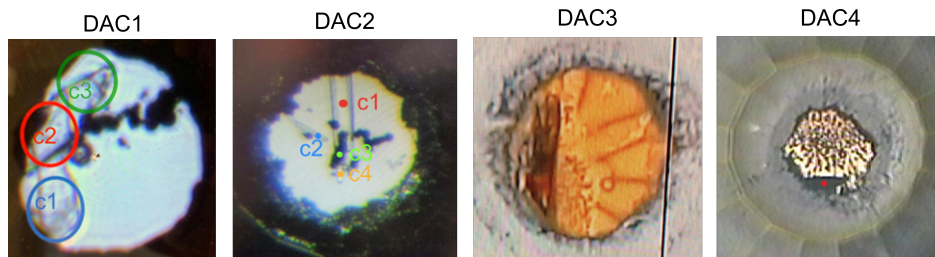


Figure B.2: Diamond-anvil sample chambers for experiments 1-4. Credit: GA Smith, UNLV: Sample preparation.



## B.4 $(\text{CH}_4)_x(\text{H}_2\text{S})_{2-x}\text{H}_2$ DAC1

Table B.2: Crystallographic details of  $(\text{CH}_4)_x(\text{H}_2\text{S})_{2-x}\text{H}_2$  at variable pressure for c1 in DAC1. Credit: Credit: GA Smith, UNLV: Sample preparation; Ines Collings: SC-XRD analysis.

$P$ (GPa)	12.2	14.4	15.0	16.1	17.2	18.8
Crystal System	Tetragonal					
Space Group	$I4/mcm$					
$Z$	8					
$a$ (Å)	6.8228(13)	6.695(2)	6.661(3)	6.613(2)	6.5691(18)	6.516(3)
$c$ (Å)	5.6283(14)	5.552(2)	5.536(3)	5.507(3)	5.481(2)	5.450(3)
$V$ (Å <sup>3</sup> )	262.00(12)	248.91(19)	245.6(2)	240.8(2)	236.50(16)	231.4(2)
<b>Data collection</b>						
No. of reflections measured	234	264	273	267	204	223
unique	87	75	80	78	65	70
unique with $I > 2\sigma$	71	62	66	63	53	57
$R_{\text{int}}$	0.0507	0.0187	0.0182	0.0491	0.0573	0.0606
<b>Refinement</b>						
No. of parameters	10	11	9	9	9	9
No. of restraints	4	4	4	4	4	4
Data/parameter ratio	7.5	6.0	7.8	7.4	6.3	6.8
$R_1 [I > 2\sigma(I)]$	0.0585	0.0484	0.0576	0.046	0.0437	0.0547
$wR_2$ (all data)	0.1847	0.1432	0.1691	0.1237	0.1284	0.1328
$\Delta\rho_{\text{min}}/\Delta\rho_{\text{max}}$ (eÅ <sup>-3</sup> )	0.46/-	0.47/-	0.69/-	0.51/-	0.45/-	0.56/-
	0.63	0.48	0.74	0.56	0.43	0.55

Table B.3: Crystallographic details of  $(\text{CH}_4)_x(\text{H}_2\text{S})_{2-x}\text{H}_2$  at variable pressure for c1 in DAC1.  
 Credit: GA Smith, UNLV: Sample preparation; Ines Collings: SC-XRD analysis.

$P$ (GPa)	20.3	22.4	24.5
Crystal System	Monoclinic		
Space Group	$C2/c$		
$Z$	24		
$a$ (Å)	8.458(2)	8.404(4)	8.316(4)
$b$ (Å)	6.5003(17)	6.452(3)	6.419(3)
$c$ (Å)	12.504(4)	12.409(7)	12.246(9)
$\beta$ (°)	99.58(3)	99.56(5)	99.57(6)
$V$ (Å <sup>3</sup> )	677.8(3)	663.5(6)	644.5(6)
<b>Data collection</b>			
No. of reflections			
measured	708	680	643
unique	486	474	456
unique with $I > 2\sigma$	285	288	243
$R_{\text{int}}$	0.0156	0.019	0.0252
<b>Refinement</b>			
No. of parameters	56	56	57
No. of restraints	11	10	11
Data/parameter ratio	5.3	5.3	4.5
$R_1 [I > 2\sigma(I)]$	0.0552	0.0685	0.0953
$wR_2$ (all data)	0.2147	0.2222	0.3524
$\Delta\rho_{\text{min}}/\Delta\rho_{\text{max}}$ ( $e\text{Å}^{-3}$ )	0.62/-0.53	0.57/-0.54	1.30/-0.75

Table B.4: Crystallographic details of  $(\text{CH}_4)_x(\text{H}_2\text{S})_{2-x}\text{H}_2$  at variable pressure for c2 in DAC1.  
 Credit: GA Smith, UNLV: Sample preparation; Ines Collings: SC-XRD analysis.

$P$ (GPa)	12.2	14.4	15.0	16.1	17.2
Crystal System	Tetragonal				
Space Group	$I4/mcm$				
$Z$	8				
$a$ (Å)	6.8028(9)	6.667(3)	6.639(4)	6.594(5)	6.539(6)
$c$ (Å)	5.6337(10)	5.564(2)	5.543(3)	5.509(3)	5.488(4)
$V$ (Å <sup>3</sup> )	260.72(8)	247.3(3)	244.3(3)	239.5(4)	234.7(5)
<b>Data collection</b>					
No. of reflections					
measured	250	254	253	234	180
unique	96	94	93	91	76
unique with $I > 2\sigma$	80	80	80	75	54
$R_{\text{int}}$	0.0199	0.0544	0.0762	0.009	0.0198
<b>Refinement</b>					
No. of parameters	9	11	9	5	5
No. of restraints	4	3	3	1	1
Data/parameter ratio	9.3	7.5	9.2	15.2	11.0
$R_1 [I > 2\sigma(I)]$	0.0849	0.0424	0.066	0.0837	0.0872
$wR_2$ (all data)	0.1815	0.1146	0.1719	0.2074	0.2862
$\Delta\rho_{\text{min}}/\Delta\rho_{\text{max}}$ (eÅ <sup>-3</sup> )	0.90/-0.94	0.50/-0.49	0.90/-0.65	1.60/-1.07	0.65/-0.71

Table B.5: Crystallographic details of  $(\text{CH}_4)_x(\text{H}_2\text{S})_{2-x}\text{H}_2$  at variable pressure for c2 in DAC1.  
 Credit: GA Smith, UNLV: Sample preparation; Ines Collings: SC-XRD analysis.

$P$ (GPa)	18.8	20.3	22.4	24.5
Crystal System	Monoclinic			
Space Group	$C2/c$			
$Z$	24			
$a$ (Å)	8.567(8)	8.500(8)	8.417(7)	8.311(11)
$b$ (Å)	6.531(4)	6.495(3)	6.457(3)	6.393(5)
$c$ (Å)	12.512(8)	12.410(7)	12.354(9)	12.303(12)
$\beta$ (°)	99.52(8)	99.50(7)	99.54(8)	99.44(11)
$V$ (Å <sup>3</sup> )	690.3(9)	675.8(8)	662.0(8)	644.9(12)
<b>Data collection</b>				
No. of reflections				
measured	710	681	685	672
unique	431	425	433	435
unique with $I > 2\sigma$	289	262	276	232
$R_{\text{int}}$	0.0676	0.0238	0.0667	0.03
<b>Refinement</b>				
No. of parameters	53	35	28	28
No. of restraints	10	0	0	0
Data/parameter ratio	5.6	7.5	9.9	8.3
$R_1 [I > 2\sigma(I)]$	0.1129	0.0849	0.0886	0.0856
$wR_2$ (all data)	0.4069	0.2639	0.2933	0.2744
$\Delta\rho_{\text{min}}/\Delta\rho_{\text{max}}$ ( $e\text{Å}^{-3}$ )	2.07/-1.04	0.95/-0.79	0.95/-0.81	1.23/-0.73

Table B.6: Crystallographic details of  $(\text{CH}_4)_x(\text{H}_2\text{S})_{2-x}\text{H}_2$  at variable pressure for c3 in DAC1. Credit: GA Smith, UNLV: Sample preparation; Ines Collings: SC-XRD analysis.

$P$ (GPa)	12.2	14.4	15.0	16.1	17.2
Crystal System	Tetragonal				
Space Group	$I4/mcm$				
$Z$	8				
$a$ (Å)	6.8236(10)	6.6883(13)	6.658(3)	6.618(3)	6.575(2)
$c$ (Å)	5.6430(9)	5.5276(9)	5.5008(14)	5.4500(14)	5.4358(14)
$V$ (Å <sup>3</sup> )	262.75(9)	247.27(10)	243.9(2)	238.7(2)	235.01(17)
<b>Data collection</b>					
No. of reflections					
measured	261	253	226	206	167
unique	97	93	91	76	71
unique with $I > 2\sigma$	84	79	77	58	49
$R_{\text{int}}$	0.0148	0.0835	0.0555	0.1006	0.0306
<b>Refinement</b>					
No. of parameters	10	9	8	8	9
No. of restraints	4	4	4	4	4
Data/parameter ratio	8.4	8.8	9.6	7.3	5.4
$R_1 [I > 2\sigma(I)]$	0.0262	0.0525	0.0569	0.0717	0.1105
$wR_2$ (all data)	0.0758	0.1365	0.1487	0.2116	0.3815
$\Delta\rho_{\text{min}}/\Delta\rho_{\text{max}}$ (eÅ <sup>-3</sup> )	0.24/−0.22	0.67/−0.78	0.53/−0.69	0.57/−0.47	0.88/−1.35

Table B.7: Crystallographic details of  $(\text{CH}_4)_x(\text{H}_2\text{S})_{2-x}\text{H}_2$  at variable pressure for c3 in DAC1. Credit: GA Smith, UNLV: Sample preparation; Ines Collings: SC-XRD analysis.

$P$ (GPa)	18.8	20.3	22.4	24.5
Crystal System	Monoclinic			
Space Group	$C2/c$			
$Z$	24			
$a$ (Å)	8.457(3)	8.394(3)	8.337(3)	8.257(3)
$b$ (Å)	6.5590(14)	6.5180(19)	6.4877(12)	6.4271(17)
$c$ (Å)	12.562(4)	12.458(5)	12.317(4)	12.194(5)
$\beta$ (°)	98.81(4)	98.81(5)	98.72(3)	98.69(4)
$V$ (Å <sup>3</sup> )	688.7(4)	673.6(4)	658.5(3)	639.7(4)
<b>Data collection</b>				
No. of reflections				
measured	678	646	635	618
unique	432	415	411	401
unique with $I > 2\sigma$	315	272	256	251
$R_{\text{int}}$	0.0475	0.0720	0.0914	0.1087
<b>Refinement</b>				
No. of parameters	50	50	46	50
No. of restraints	9	9	9	9
Data/parameter ratio	6.3	5.4	5.6	5.0
$R_1 [I > 2\sigma(I)]$	0.0788	0.0871	0.0919	0.0885
$wR_2$ (all data)	0.2875	0.3033	0.2932	0.2795
$\Delta\rho_{\text{min}}/\Delta\rho_{\text{max}}$ (eÅ <sup>-3</sup> )	0.65/−0.90	0.69/−0.78	0.66/−0.55	0.85/−0.69

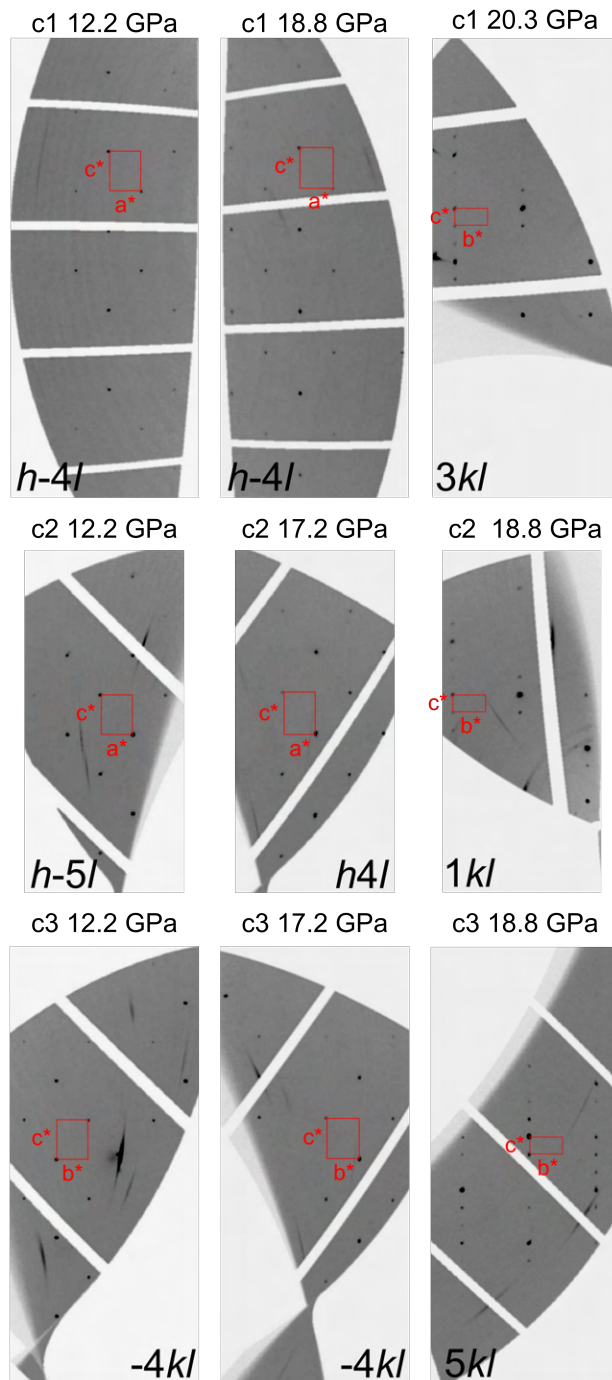


Figure B.3: Selected reciprocal space reconstructions for crystals 1 to 3 of the  $(\text{CH}_4)_x(\text{H}_2\text{S})_{2-x}\text{H}_2$  loading in DAC1. The monoclinic phase is observed for all crystals at 19-20 GPa. Credit: GA Smith, UNLV: Sample preparation; Ines Collings: SC-XRD analysis.

B.5  $(\text{CH}_4)_x(\text{H}_2\text{S})_{2-x}\text{H}_2$  DAC2

Table B.8: Crystallographic details of  $(\text{CH}_4)_x(\text{H}_2\text{S})_{2-x}\text{H}_2$  at variable pressure for c1 in DAC2. Credit: GA Smith, UNLV: Sample preparation; Ines Collings: SC-XRD analysis.

$P$ (GPa)	8	9	13	18	26	29
Crystal System	Tetragonal					
Space Group	$I4/mcm$					
$Z$	8					
$a$ (Å)	7.099(7)	6.863(10)	6.654(10)	6.480(6)	6.35(3)	6.275(6)
$c$ (Å)	5.859(2)	5.734(7)	5.566(7)	5.400(3)	5.189(10)	5.238(3)
$V$ (Å <sup>3</sup> )	295.3(6)	270.1(9)	246.4(8)	226.7(4)	209(2)	206.3(4)
<b>Data collection</b>						
No. of reflections measured	360	351	302	279	281	266
unique	114	108	90	87	81	78
unique with $I > 2\sigma$	52	57	52	58	43	44
$R_{\text{int}}$	0.0432	0.0375	0.1805	0.033	0.1433	0.0507
<b>Refinement</b>						
No. of parameters	6	3	4	7	4	4
No. of restraints	0	0	0	0	0	0
Data/parameter ratio	8.7	19.0	13.0	8.3	10.8	11.0
$R_1 [I > 2\sigma(I)]$	0.1285	0.1249	0.1031	0.1221	0.1618	0.1149
$wR_2$ (all data)	0.3585	0.329	0.2744	0.2851	0.3582	0.2914
$\Delta\rho_{\text{min}}/\Delta\rho_{\text{max}}$ (eÅ <sup>-3</sup> )	0.81/-	1.07/-	1.03/-	1.02/-	1.22/-	0.72/-
	1.48	0.62	0.54	0.89	0.70	0.58



Table B.9: Crystallographic details of  $(\text{CH}_4)_x(\text{H}_2\text{S})_{2-x}\text{H}_2$  at variable pressure for c1 in DAC2. Credit: GA Smith, UNLV: Sample preparation; Ines Collings: SC-XRD analysis.

$P$ (GPa)	32	37	38	40	45	49
Crystal System	Tetragonal					
Space Group	$I4/mcm$					
$Z$	8					
$a$ ( $\text{\AA}$ )	6.221(5)	6.124(3)	6.094(3)	6.072(2)	5.976(5)	6.022(10)
$c$ ( $\text{\AA}$ )	5.179(2)	5.135(2)	5.1148(16)	5.0961(11)	5.011(5)	5.011(8)
$V$ ( $\text{\AA}^3$ )	200.4(3)	192.6(2)	189.94(18)	187.91(15)	179.0(3)	181.7(7)
<b>Data collection</b>						
No. of reflections measured	270	251	256	214	240	218
unique	80	74	73	70	82	83
unique with $I > 2\sigma$	54	64	64	60	31	25
$R_{\text{int}}$	0.0344	0.0177	0.0242	0.0667	0.1459	0.1798
<b>Refinement</b>						
No. of parameters	4	3	3	4	7	3
No. of restraints	0	0	0	0	0	0
Data/parameter ratio	13.5	21.3	21.3	15.0	4.4	8.3
$R_1 [I > 2\sigma(I)]$	0.1105	0.0922	0.1146	0.087	0.1518	0.1768
$wR_2$ (all data)	0.2716	0.2288	0.2657	0.1962	0.3636	0.4235
$\Delta\rho_{\text{min}}/\Delta\rho_{\text{max}}$ ( $e\text{\AA}^{-3}$ )	0.98/-	1.29/-	1.28/-	0.66/-	1.05/-	1.36/-
	0.98	0.87	0.87	0.93	0.82	0.73

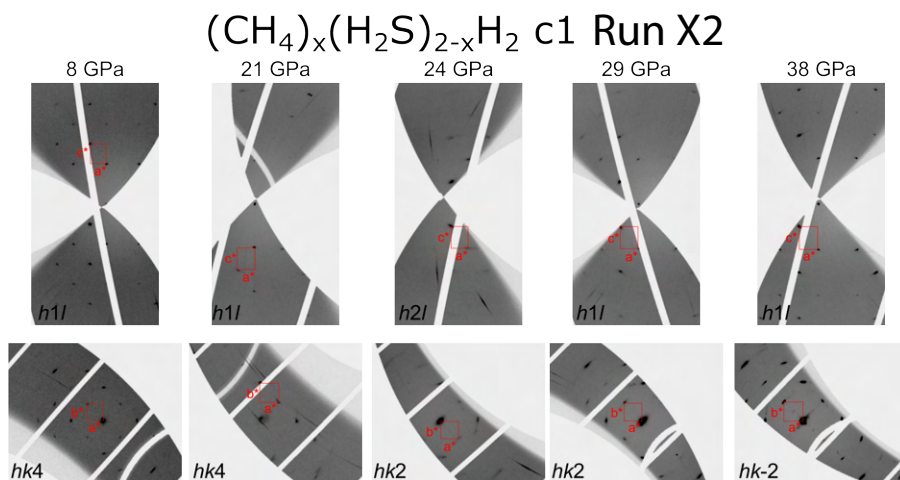


Figure B.4: Selected reciprocal space reconstructions for crystal 1 of the  $(\text{CH}_4)_x(\text{H}_2\text{S})_{2-x}\text{H}_2$  loading in DAC2. No monoclinic distortion is observed in this crystal. The diffraction spots have a large mosaicity in the  $\mathbf{ab}$ -plane. Credit: GA Smith, UNLV: Sample preparation; Ines Collings: SC-XRD analysis.

Table B.10: Crystallographic details of  $(\text{CH}_4)_x(\text{H}_2\text{S})_{2-x}\text{H}_2$  at variable pressure for c2 in DAC2. Credit: GA Smith, UNLV: Sample preparation; Ines Collings: SC-XRD analysis.

$P$ (GPa)	8	9	18	29	32
Crystal System	Tetragonal				
Space Group	$I4/mcm$				
$Z$	8				
$a$ (Å)	7.0808(18)	6.8963(14)	6.4685(10)	6.2150(9)	6.1810(10)
$c$ (Å)	5.8513(16)	5.6994(13)	5.3946(9)	5.2094(7)	5.1719(6)
$V$ (Å <sup>3</sup> )	293.37(17)	271.06(13)	225.72(8)	201.22(6)	197.59(7)
<b>Data collection</b>					
No. of reflections					
measured	430	362	229	264	263
unique	164	151	120	106	101
unique with $I > 2\sigma$	99	117	66	77	66
$R_{\text{int}}$	0.0392	0.0263	0.0802	0.1359	0.0348
<b>Refinement</b>					
No. of parameters	4	11	3	3	4
No. of restraints	0	2	0	0	0
Data/parameter ratio	24.8	10.6	22	25.7	16.5
$R_1$ [ $I > 2\sigma(I)$ ]	0.0489	0.0470	0.1195	0.1066	0.0625
$wR_2$ (all data)	0.1444	0.1144	0.3279	0.3065	0.1822
$\Delta\rho_{\text{min}}/\Delta\rho_{\text{max}}$ (eÅ <sup>-3</sup> )	0.51/−0.48	0.50/−0.40	1.5/−1.9	1.4/−1.8	1.1/−1.4

Table B.11: Crystallographic details of  $(\text{CH}_4)_x(\text{H}_2\text{S})_{2-x}\text{H}_2$  at variable pressure for c2 in DAC2. Credit: GA Smith, UNLV: Sample preparation; Ines Collings: SC-XRD analysis.

$P$ (GPa)	24	26
Crystal System	Monoclinic	
Space Group	$C2/c$	
$Z$	24	
$a$ (Å)	8.243(3)	8.180(4)
$b$ (Å)	6.3158(6)	6.2688(9)
$c$ (Å)	12.2764(15)	12.226(2)
$\beta$ (°)	99.205(19)	99.26(3)
$V$ (Å <sup>3</sup> )	630.9(2)	618.8(3)
<b>Data collection</b>		
No. of reflections		
measured	980	947
unique	582	567
unique with $I > 2\sigma$	379	300
$R_{\text{int}}$	0.1888	0.0813
<b>Refinement</b>		
No. of parameters	13	53
No. of restraints	0	10
Data/parameter ratio	29	7.1
$R_1 [I > 2\sigma(I)]$	0.1629	0.0675
$wR_2$ (all data)	0.4371	0.2292
$\Delta\rho_{\text{min}}/\Delta\rho_{\text{max}}$ (eÅ <sup>-3</sup> )	2.0/-1.7	0.62/-0.68

Table B.12: Crystallographic details of  $(\text{CH}_4)_x(\text{H}_2\text{S})_{2-x}\text{H}_2$  at variable pressure for c2 in DAC2. Credit: GA Smith, UNLV: Sample preparation; Ines Collings: SC-XRD analysis.

$P$ (GPa)	37	38	40	45	49
Crystal System	Tetragonal				
Space Group	X $I4/mcm$				
$Z$	8				
$a$ (Å)	6.088(2)	6.068(2)	6.0509(19)	5.981(2)	5.974(3)
$c$ (Å)	5.109(2)	5.089(2)	5.077(2)	5.007(2)	4.975(5)
$V$ (Å <sup>3</sup> )	189.35(16)	187.39(15)	185.88(14)	179.14(14)	177.5(2)
<b>Data collection</b>					
No. of reflections					
measured	240	239	233	223	175
unique	101	101	98	93	81
unique with $I > 2\sigma$	64	63	56	75	51
$R_{\text{int}}$	0.0774	0.0737	0.1139	0.0289	0.176
<b>Refinement</b>					
No. of parameters	3	3	12	11	
No. of restraints	0	0	0	0	
Data/parameter ratio	21.3	21.0	4.7	6.8	
$R_1 [I > 2\sigma(I)]$	0.1183	0.0887	0.1289	0.0834	
$wR_2$ (all data)	0.2863	0.2153	0.2643	0.1983	
$\Delta\rho_{\text{min}}/\Delta\rho_{\text{max}}$ (eÅ <sup>-3</sup> )	1.706/-	1.228/-	0.951/-	1.486/-	
	1.33	1.095	1.193	0.975	

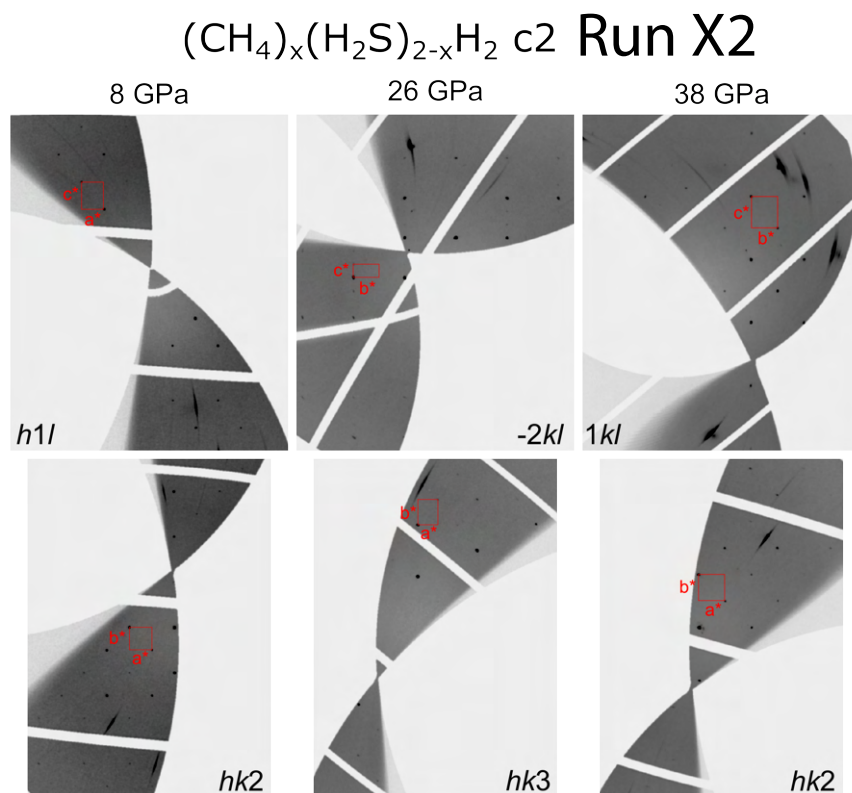


Figure B.5: Selected reciprocal space reconstructions for crystal 2 of the  $(\text{CH}_4)_x(\text{H}_2\text{S})_{2-x}\text{H}_2$  loading in DAC2. The monoclinic distortion is observed at pressure points 24 and 26 GPa. Credit: GA Smith, UNLV: Sample preparation; Ines Collings: SC-XRD analysis.

Table B.13: Crystallographic details of  $(\text{CH}_4)_x(\text{H}_2\text{S})_{2-x}\text{H}_2$  at variable pressure for c3 in DAC2. Credit: GA Smith, UNLV: Sample preparation; Ines Collings: SC-XRD analysis.

$P$ (GPa)	8	9	24	26	37
Crystal System	Tetragonal				
Space Group	$I4/mcm$				
$Z$	8				
$a$ (Å)	7.079(4)	6.8889(10)	6.321(8)	6.297(3)	6.122(10)
$c$ (Å)	5.850(2)	5.7016(8)	5.299(3)	5.260(2)	5.126(5)
$V$ (Å <sup>3</sup> )	293.1(4)	270.58(9)	211.7(5)	208.6(2)	192.1(7)
<b>Data collection</b>					
No. of reflections					
measured	393	371	290	285	259
unique	108	101	82	83	75
unique with $I > 2\sigma$	63	72	47	61	16
$R_{\text{int}}$	0.0585	0.0268	0.0403	0.1174	0.3467
<b>Refinement</b>					
No. of parameters	4	4	5	3	4
No. of restraints	0	0	1	0	0
Data/parameter ratio	15.8	18	9.4	20.3	4
$R_1 [I > 2\sigma(I)]$	0.1297	0.048	0.0719	0.0915	0.1309
$wR_2$ (all data)	0.2888	0.1371	0.1972	0.2333	0.4019
$\Delta\rho_{\text{min}}/\Delta\rho_{\text{max}}$ (eÅ <sup>-3</sup> )	0.63/-0.79	0.46/-0.35	0.54/-0.40	1.29/-0.73	0.56/-0.36

Table B.14: Crystallographic details of  $(\text{CH}_4)_x(\text{H}_2\text{S})_{2-x}\text{H}_2$  at variable pressure for c3 in DAC2. Credit: GA Smith, UNLV: Sample preparation; Ines Collings: SC-XRD analysis.

$P$ (GPa)	18	29	32
Crystal System	Monoclinic		
Space Group	$C2/c$		
$Z$	24		
$a$ (Å)	8.388(4)	8.152(5)	8.108(2)
$b$ (Å)	6.498(5)	6.287(3)	6.251(2)
$c$ (Å)	12.501(5)	12.141(7)	12.055(4)
$\beta$ (°)	98.73(5)	99.00(6)	98.98(3)
$V$ (Å <sup>3</sup> )	673.4(6)	614.6(6)	603.5(3)
<b>Data collection</b>			
No. of reflections measured	1012	886	873
unique	633	578	564
unique with $I > 2\sigma$	267	301	329
$R_{\text{int}}$	0.1225	0.0584	0.1262
<b>Refinement</b>			
No. of parameters	13	13	13
No. of restraints	0	0	0
Data/parameter ratio	21	23	25
$R_1 [I > 2\sigma(I)]$	0.0919	0.1044	0.1348
$wR_2$ (all data)	0.2914	0.4093	0.4148
$\Delta\rho_{\text{min}}/\Delta\rho_{\text{max}}$ (eÅ <sup>-3</sup> )	0.89/-0.98	2.07/-1.73	2.09/-1.35

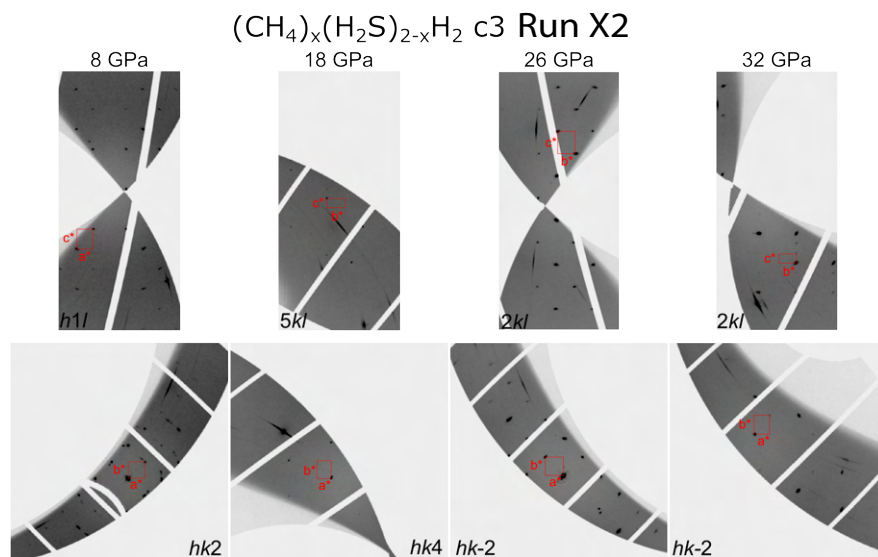


Figure B.6: Selected reciprocal space reconstructions for crystal 3 of the  $(\text{CH}_4)_x(\text{H}_2\text{S})_{2-x}\text{H}_2$  loading in DAC2. The monoclinic distortion is observed at 18 GPa. The few reflections observed at 18 GPa is due to crystal alignment issues, which was fixed by re-defining its position after 24 GPa. Weak reflections of the monoclinic distortion are observed for pressure points 29 and 32 GPa. Credit: GA Smith, UNLV: Sample preparation; Ines Collings: SC-XRD analysis.



Table B.15: Crystallographic details of  $(\text{CH}_4)_x(\text{H}_2\text{S})_{2-x}\text{H}_2$  at variable pressure for c4 in DAC2. Credit: GA Smith, UNLV: Sample preparation; Ines Collings: SC-XRD analysis.

$P$ (GPa)	8	9	24	26	29
Crystal System	Tetragonal				
Space Group	$I4/mcm$				
$Z$	8				
$a$ (Å)	7.085(5)	6.893(2)	6.333(2)	6.25(3)	6.258(2)
$c$ (Å)	5.853(3)	5.6925(15)	5.2304(11)	5.19(3)	5.1553(12)
$V$ (Å <sup>3</sup> )	293.8(4)	270.46(19)	209.79(15)	203(3)	201.90(16)
<b>Data collection</b>					
No. of reflections					
measured	374	368	259	288	281
unique	111	108	80	85	86
unique with $I > 2\sigma$	68	80	63	9	48
$R_{\text{int}}$	0.0706	0.0301	0.0308	0.8049	0.078
<b>Refinement</b>					
No. of parameters	4	8	3	3	4
No. of restraints	0	0	0	0	0
Data/parameter ratio	17	10	21	3	12
$R_1 [I > 2\sigma(I)]$	0.0456	0.0543	0.0963	0.2788	0.1384
$wR_2$ (all data)	0.161	0.1322	0.3053	0.7549	0.4008
$\Delta\rho_{\text{min}}/\Delta\rho_{\text{max}}$ (eÅ <sup>-3</sup> )	0.48/-0.42	0.46/-0.42	1.02/-1.55	0.74/-0.63	1.64/-1.31

Table B.16: Crystallographic details of  $(\text{CH}_4)_x(\text{H}_2\text{S})_{2-x}\text{H}_2$  at variable pressure for c4 in DAC2. Credit: GA Smith, UNLV: Sample preparation; Ines Collings: SC-XRD analysis.

$P$ (GPa)	32	37	38	40	45	49
Crystal System	Tetragonal					
Space Group	$I4/mcm$					
$Z$	8					
$a$ (Å)	6.215(3)	6.1094(16)	6.0887(19)	6.062(4)	6.0106(13)	5.9885(13)
$c$ (Å)	5.1128(15)	5.0392(12)	5.0182(14)	5.010(3)	4.9539(10)	4.9343(9)
$V$ (Å <sup>3</sup> )	197.5(2)	188.09(11)	186.04(13)	184.1(3)	178.97(9)	176.95(8)
<b>Data collection</b>						
No. of reflections						
measured	277	276	269	253	232	181
unique	83	81	81	79	75	64
unique with $I > 2\sigma$	46	52	47	25	56	59
$R_{\text{int}}$	0.0714	0.068	0.0811	0.3762	0.0376	0.0146
<b>Refinement</b>						
No. of parameters	4	4	4	3	8	11
No. of restraints	0	0	0	0	0	5
Data/parameter ratio	11.5	13	11.8	8.3	7	5.4
$R_1 [I > 2\sigma(I)]$	0.1323	0.0821	0.0724	0.254	0.06	0.0321
$wR_2$ (all data)	0.4102	0.2151	0.1853	0.5699	0.1558	0.0855
$\Delta\rho_{\text{min}}/\Delta\rho_{\text{max}}$ (eÅ <sup>-3</sup> )	1.37/-	1.30/-	0.98/-	1.86/-	0.66/-	0.54/-
	1.27	1.70	0.93	1.85	0.78	0.43

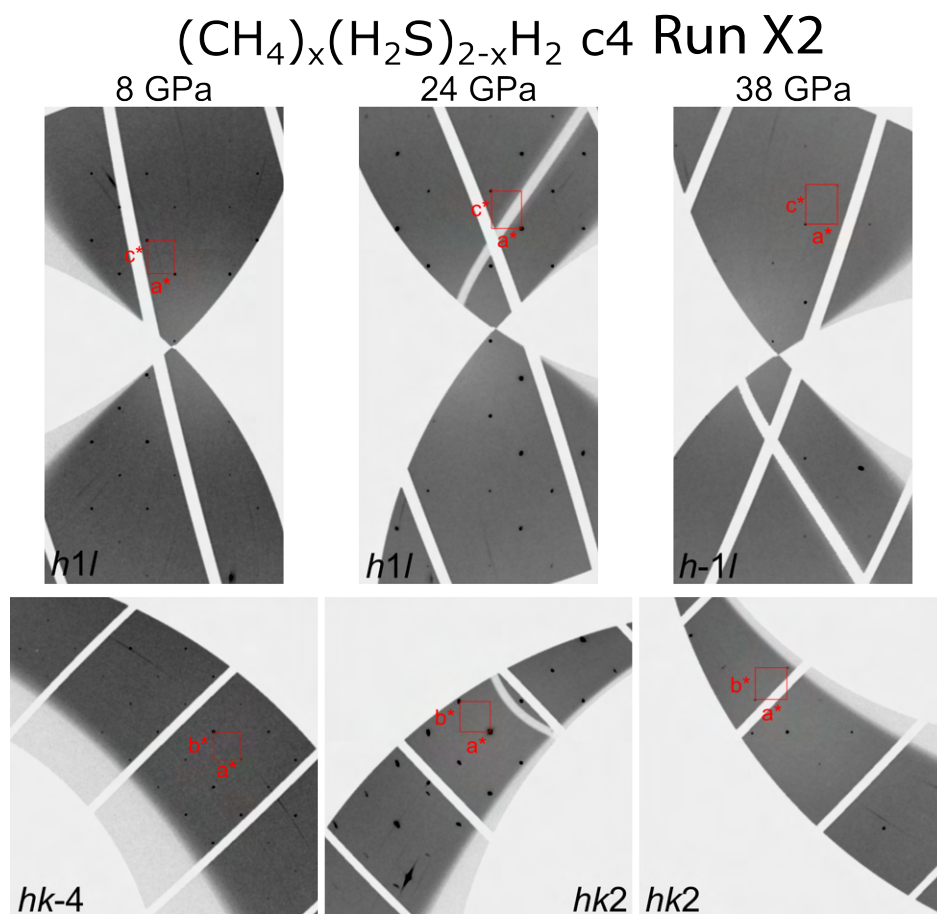


Figure B.7: Selected reciprocal space reconstructions for crystal 4 of the  $(\text{CH}_4)_x(\text{H}_2\text{S})_{2-x}\text{H}_2$  loading in DAC2. No monoclinic distortion is observed at 24 GPa. Crystal alignment issues means that there are no data above 9 GPa up till 24 GPa. At 24 GPa, the position of c4 was re-defined. Credit: GA Smith, UNLV: Sample preparation; Ines Collings: SC-XRD analysis.

## B.6 (H<sub>2</sub>S)<sub>2</sub>H<sub>2</sub> DAC3

Table B.17: Crystallographic details of the (H<sub>2</sub>S)<sub>2</sub>H<sub>2</sub> loading in DAC3. The hydrogens bonded to S were not included in the refinement. Credit: GA Smith, UNLV: Sample preparation; Ines Collings: SC-XRD analysis.

<i>P</i> (GPa)	8.1	15.3	23.1	30.0	39.7	48.1
Crystal System	Tetragonal					
Space Group	<i>I4/mcm</i>					
<i>Z</i>	8					
<i>a</i> (Å)	7.035(3)	6.6313(10)	6.42(2)	6.282(5)	6.102(5)	6.018(7)
<i>c</i> (Å)	5.830(3)	5.5173(13)	5.39(3)	5.149(7)	4.987(10)	4.938(10)
<i>V</i> (Å <sup>3</sup> )	288.5(3)	242.62(9)	221.8(19)	203.2(4)	185.7(5)	178.8(5)
<b>Data collection</b>						
No. of reflections						
measured	328	271	248	205	186	184
unique	140	118	105	96	90	90
unique with <i>I</i> > 2σ	88	99	39	71	57	61
<i>R</i> <sub>int</sub>	0.0219	0.0493	0.0480	0.1022	0.1477	0.1535
<b>Refinement</b>						
No. of parameters	7	7	5	4		
No. of restraints	1	1	1	1		
Data/parameter ratio	12.6	14.1	7.8	17.8		
<i>R</i> <sub>1</sub> [ <i>I</i> > 2σ( <i>I</i> )]	0.0766	0.0479	0.1105	0.2603		
<i>wR</i> <sub>2</sub> (all data)	0.1924	0.1280	0.3451	0.5617		
Δρ <sub>min</sub> /Δρ <sub>max</sub> (eÅ <sup>-3</sup> )	0.55/−0.530.58/−0.650.95/−0.574.1/−2.2					

Table B.18: Crystallographic details of the  $(\text{H}_2\text{S})_2\text{H}_2$  loading in DAC3 at 23 GPa at position 2. No hydrogen were included in the refinement. Credit: GA Smith, UNLV: Sample preparation; Ines Collings: SC-XRD analysis.

$P$ (GPa)	23.1
Crystal System	Monoclinic
Space Group	$C2/c$
$Z$	24
$a$ (Å)	8.321(6)
$b$ (Å)	6.4115(11)
$c$ (Å)	12.410(3)
$\beta$ (°)	98.70(5)
$V$ (Å <sup>3</sup> )	654.4(5)
<b>Data collection</b>	
No. of reflections	
measured	801
unique	545
unique with $I > 2\sigma$	373
$R_{\text{int}}$	0.1166
<b>Refinement</b>	
No. of parameters	14
No. of restraints	0
Data/parameter ratio	26.6
$R_1 [I > 2\sigma(I)]$	0.1453
$wR_2$ (all data)	0.3814
$\Delta\rho_{\text{min}}/\Delta\rho_{\text{max}}$ (eÅ <sup>-3</sup> )	1.4/−0.77

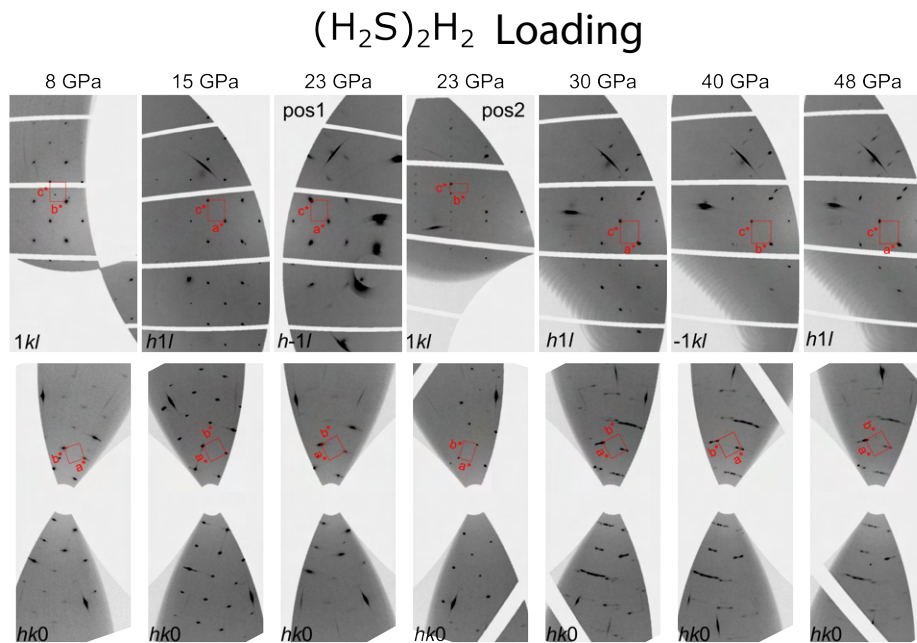


Figure B.8: Reciprocal space reconstructions for (H<sub>2</sub>S)<sub>2</sub>H<sub>2</sub> loading in DAC3. The 23 GPa pressure point has two reconstructions in different positions of the crystal. The *C*2/*c* phase is observed for position 2 at 23 GPa. The data quality significantly reduced at 30 GPa and above, where twinning and high mosaicity in the (**ab**)-plane are observed. Credit: GA Smith, UNLV: Sample preparation; Ines Collings: SC-XRD analysis.

## B.7 $(\text{CH}_4)_x(\text{H}_2\text{S})_{2-x}\text{H}_2$ DAC4

Table B.19: Crystallographic details of the  $(\text{CH}_4)_x(\text{H}_2\text{S})_{2-x}\text{H}_2$  loading in DAC4 at 90 GPa.  
Credit: GA Smith, UNLV: Sample preparation; Ines Collings: SC-XRD analysis.

$P$ (GPa)	90
Crystal System	Tetragonal
Space Group	$I4/mcm$
$Z$	8
$a$ (Å)	5.577(4)
$c$ (Å)	4.586(4)
$V$ (Å <sup>3</sup> )	142.6(2)
<b>Data collection</b>	
No. of reflections	
measured	62
unique	36
unique with $I > 2\sigma$	34
$R_{\text{int}}$	0.0163
<b>Refinement</b>	
No. of parameters	4
No. of restraints	0
Data/parameter ratio	9
$R_1 [I > 2\sigma(I)]$	0.1576
$wR_2$ (all data)	0.3904
$\Delta\rho_{\text{min}}/\Delta\rho_{\text{max}}$ (eÅ <sup>-3</sup> )	2.2/-1.78

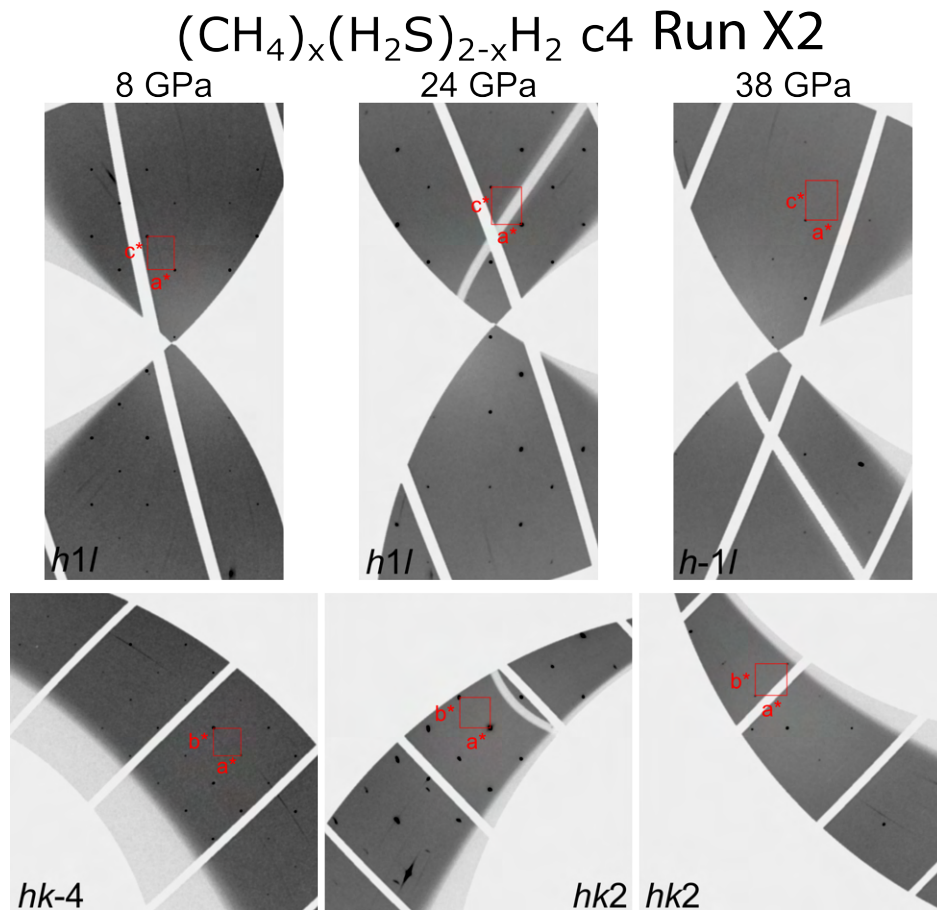


Figure B.9: Reciprocal space reconstructions for  $(\text{CH}_4)_x(\text{H}_2\text{S})_{2-x}\text{H}_2$  loading in DAC4 at 90 GPa. Two twin domains are present, and each twin has additional weaker reflections visible in the diagonal of the  $\mathbf{ab}$ -plane, which could be modelled using an incommensurate modulation  $\mathbf{q}^*$  vector as  $0.241(5) \ 0.237(5) \ 0(0.005)$ . Credit: GA Smith, UNLV; Sample preparation; Ines Collings: SC-XRD analysis.



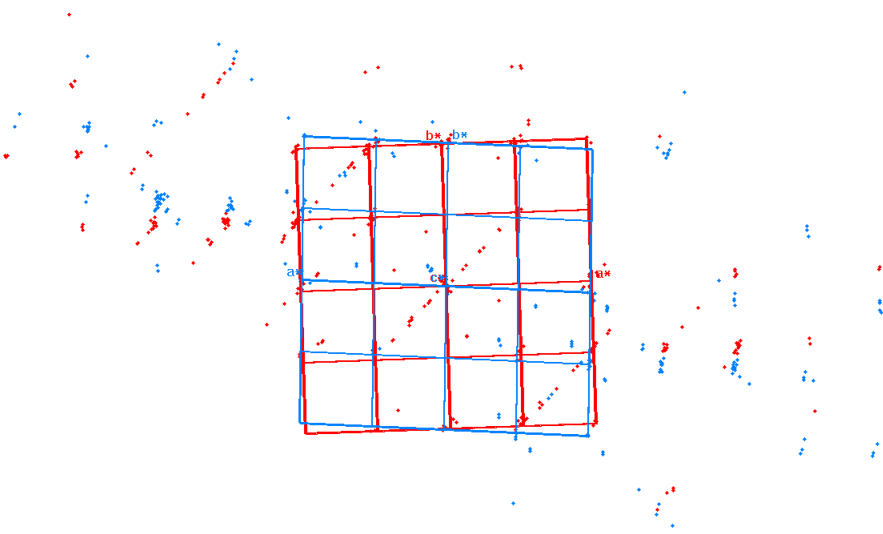


Figure B.10: Reflections from the two twin domains (red and blue) with the incommensurate peaks from each domain. Credit: Ines Collings: SC-XRD Analysis. Credit: GA Smith, UNLV: Sample preparation; Ines Collings: SC-XRD analysis.

## B.8 HYDROGEN POSITIONS

The positions of the hydrogens were located from the difference Fourier maps for the single-crystal data collections with the best integration statistics. Figure B.11 shows the steps in the refinement when the H positions were added. We note that the positive electron density in Figure B.11(a) is located at the center of the H<sub>2</sub> bonding. Indeed molecular dynamics simulations indicate that the H<sub>2</sub> molecule is freely rotating about the central 4*c* Wykoff site. In Figure B.11(b), the distance between the S atom and the positive electron density is at 1.35 Å, which matches well with the expected S–H bonding distance. Figure B.11(c) illustrates that the occupancy of the H position bonded to S is not fully occupied, and the next refinement step with a halved H occupancy results in a better residual  $F_o - F_c$  map. Addition of the remaining H positions does not result in significant changes in the  $R$  factors, although the difference map does improve (Figure B.11(g,h)).

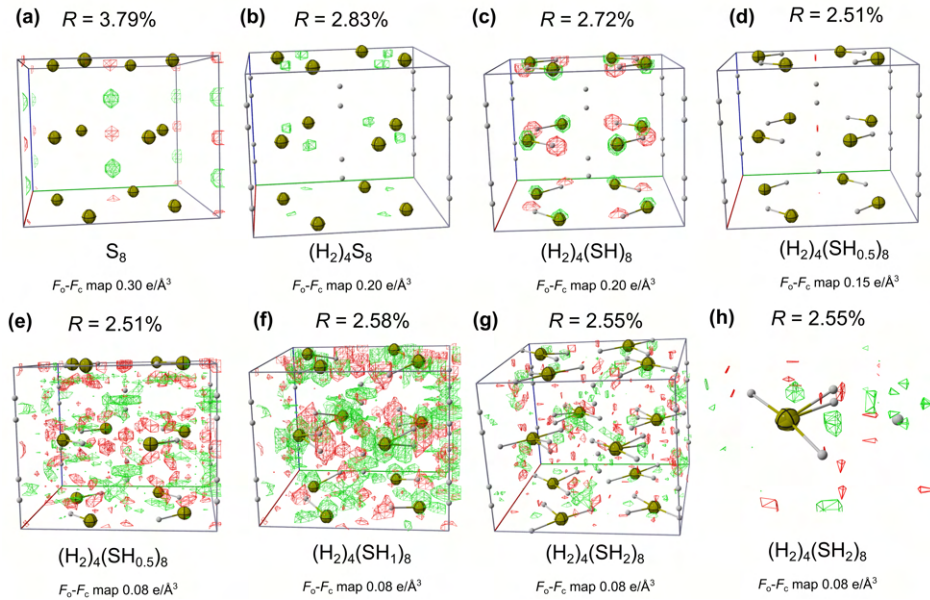


Figure B.11: Figures illustrating how the hydrogen positions were allocated starting from  $S_8$  for c3 at 12.2 GPa. The difference Fourier maps ( $F_o - F_c$ ) are shown at the levels indicated below each figure. Credit: GA Smith, UNLV: Sample preparation; Ines Collings: SC-XRD analysis.

The same procedure described above was applied to c1 at the pressure point 14.4 GPa (Figure B.12). The difference Fourier maps are shown for each addition of H, which is initially incorporated as fully occupied. The following step involved halving the H occupancy bonded to S.

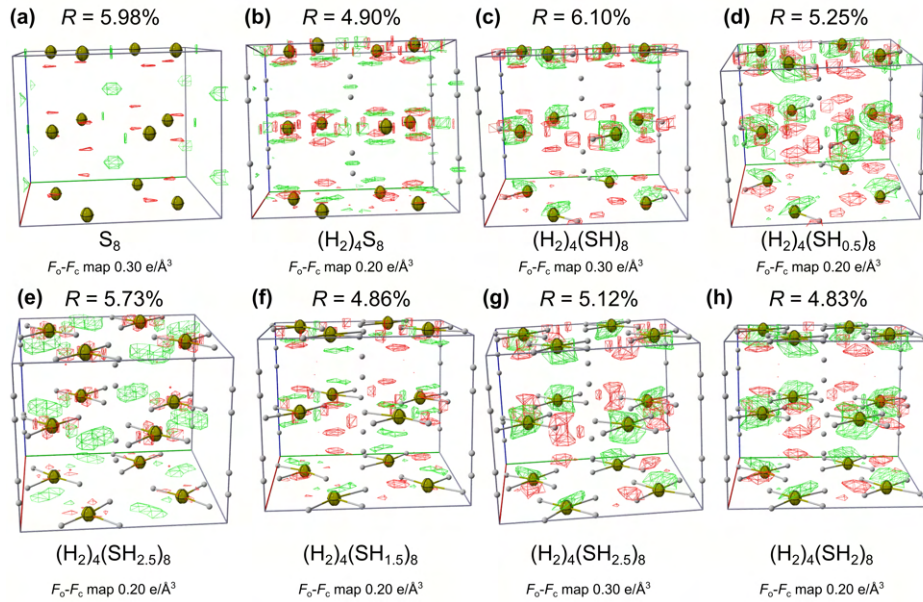


Figure B.12: Figures illustrating how the hydrogen positions were allocated starting from  $S_8$  for c1 at 14.3 GPa. The difference Fourier maps ( $F_o - F_c$ ) are shown at the levels indicated below each figure. Credit: GA Smith, UNLV: Sample preparation; Ines Collings: SC-XRD analysis.

Table B.20:  $\Delta T/T_C$  Values for runs T1 and T2. Values were calculated by normalizing Resistance over the superconducting transition and taking values between 90% and 10% of the transition. Also provided are the resistance values used to normalize each measurement. Credit: Dias Group, University of Rochester: Resistance measurements; GA Smith:  $\Delta T/T_C$  analysis.

Run	P (GPa)	$\Delta T$ (K)	Resistance ( $\Omega$ )	Tc (K)	DT/TC
T1	89	12	1.574	170	0.0706
	92	10.8	0.802	174	0.0621
	95	14.8	0.867	188	0.0787
	97	7.2	0.743	191	0.0377
T2	93	39.2	2.866	176	0.223
	98	44.4	2.759	188	0.236

## B.9 EXTENDED TRANSPORT DATA

Presented below are the  $T_C$  measurements for the Run T2 performed in this work

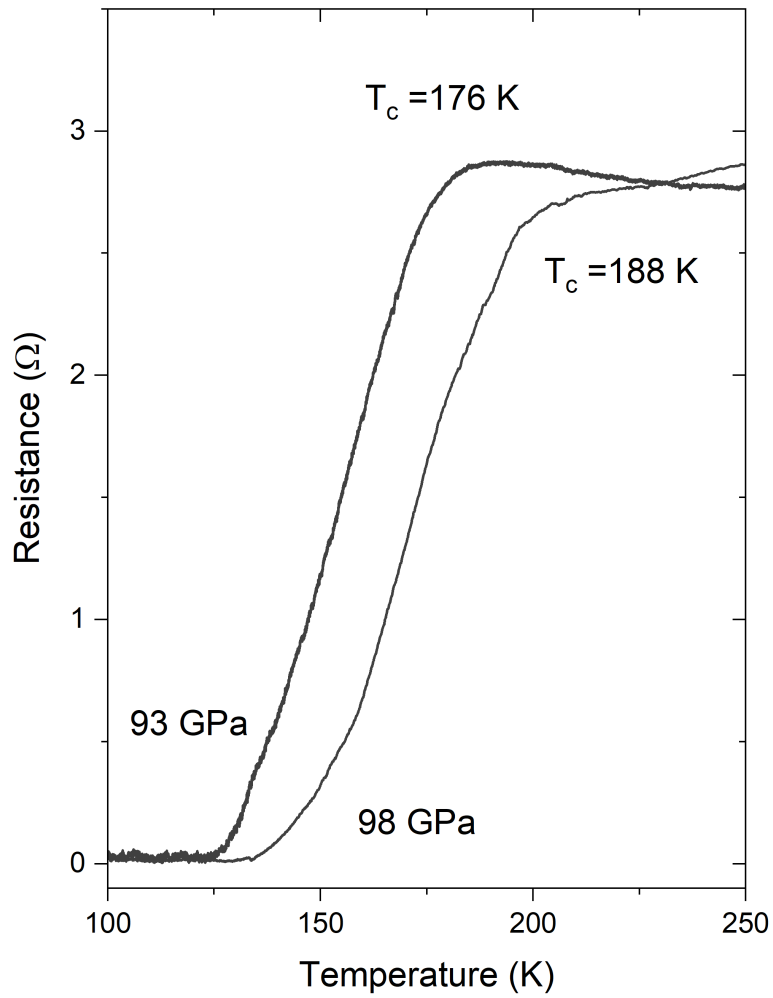


Figure B.13: Resistance response with temperatures for run 2 of the transport data. Credit: Dias Group, University of Rochester: Resistance measurements.

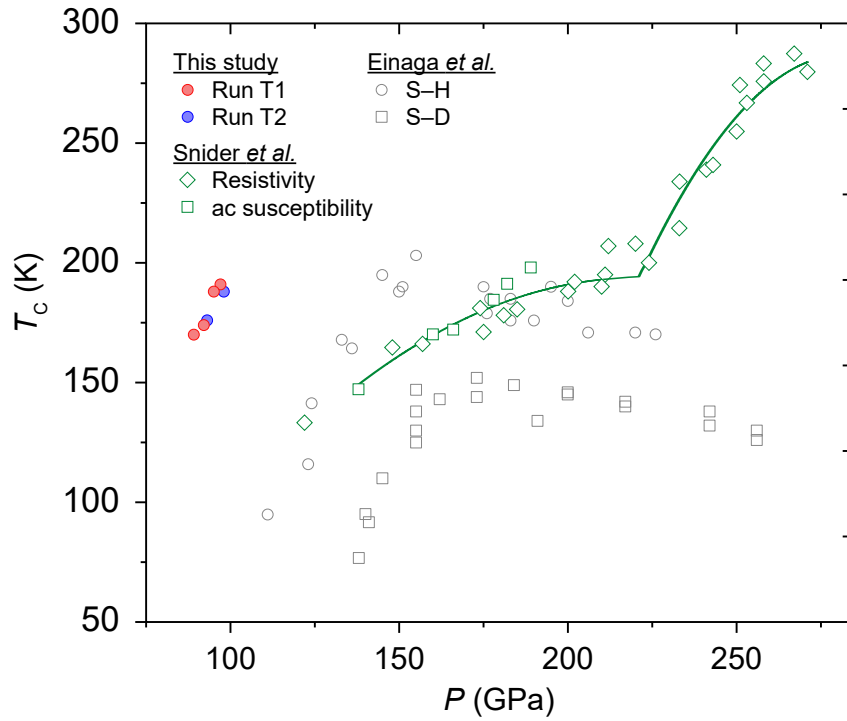


Figure B.14: A comparison of the critical temperatures presented in this work with C-S-H from [3] and SH<sub>3</sub> from [175] Credit: Dean Smith, UNLV: design.

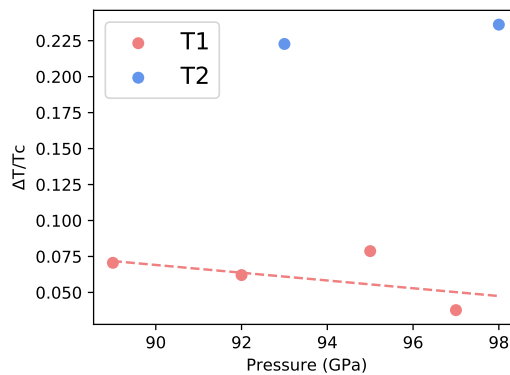


Figure B.15: The  $\Delta T/T_c$  values for runs T1 and T2 with pressure. Run T1 displays a much narrower transition than T2, which has a near three times broader transition. A least-squares trendline was added to the T1 data as a guide to the eye. Credit: Dias Group, University of Rochester: Resistance measurements; GA Smith:  $\Delta T/T_c$  analysis.

## B.10 SIMULATIONS

Plane-wave density functional theory (PW-DFT) *ab initio* simulations were performed with the Vienna *ab initio* simulation package (VASP) version 5.4.4 using the vdW-DF2 non-local correlation functional.[179] The simulations used an evenly spaced  $\Gamma$ -centered k-point grid with  $0.2 \text{ \AA}^{-1}$  resolution.[192] As the system is potentially metallic, the Brillouin zone was integrated using Gaussian smearing with a width of 0.15 eV. The basis set cutoff energy was 800 eV using the projector augmented wave (PAW) [193] pseudo-potentials formulated for PBE based GW simulations (version 5.4) with valence configurations of  $3s^23p^4$  for S,  $2s^22p^2$  for C, and the "hard"  $1s$  for H (ie. H\_h\_GW). The self-consistent field simulations were converged to 1E-6 eV and forces in optimizations were converged to  $1\text{E-}3 \text{ eV \AA}^{-1}$ . Optimizations of the atomic positions were performed with the lattices and sulfur positions fixed at their experimentally determined values unless otherwise noted.

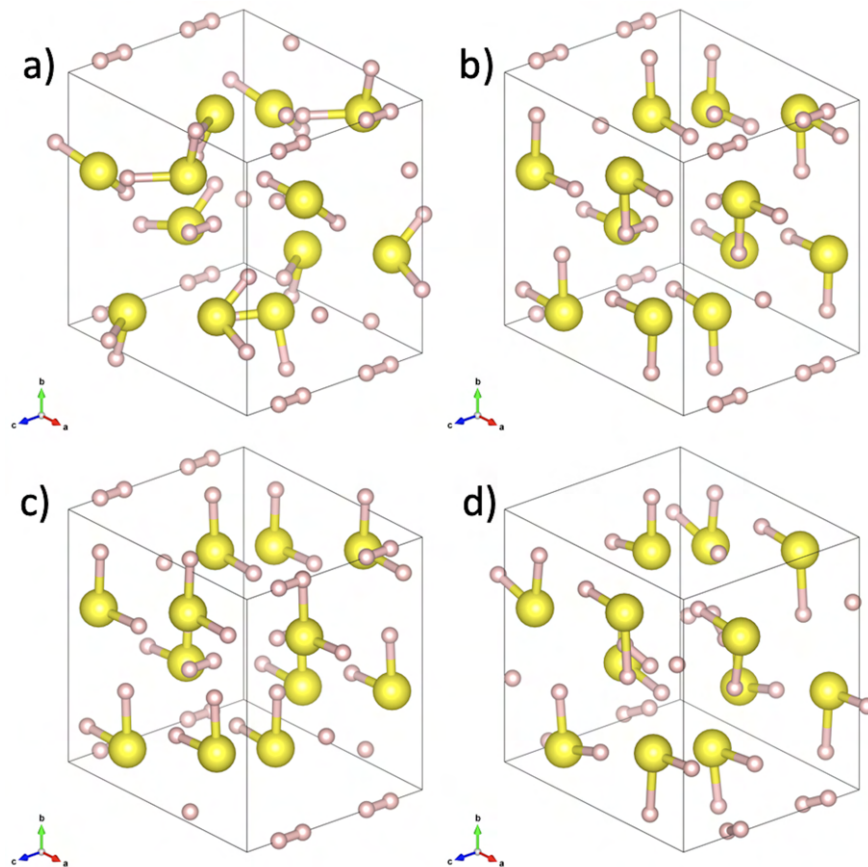


Figure B.16: 4 possible arrangements of the  $\text{H}_2\text{S}$  units within the refined 50 GPa  $I4/mcm$  structure with the lattice and S positions fixed at their refined positions (Fig. 3c of the main text), and using the H positions of the (a)  $P1$  structure of [160] or (b-d) constructed from the partial occupancies refined here. Each (b-d) structure was constrained to obey the ice rules and is an example of a class of arrangements with (b) being rings of stacked pinwheels pointed the same direction, (c) being linear chains in [100] with each molecular unit pointed the same direction, and (d) being linear chains along [001] with each molecular unit pointed the same direction. Credit: Keith Lawler, UNLV: Theory.



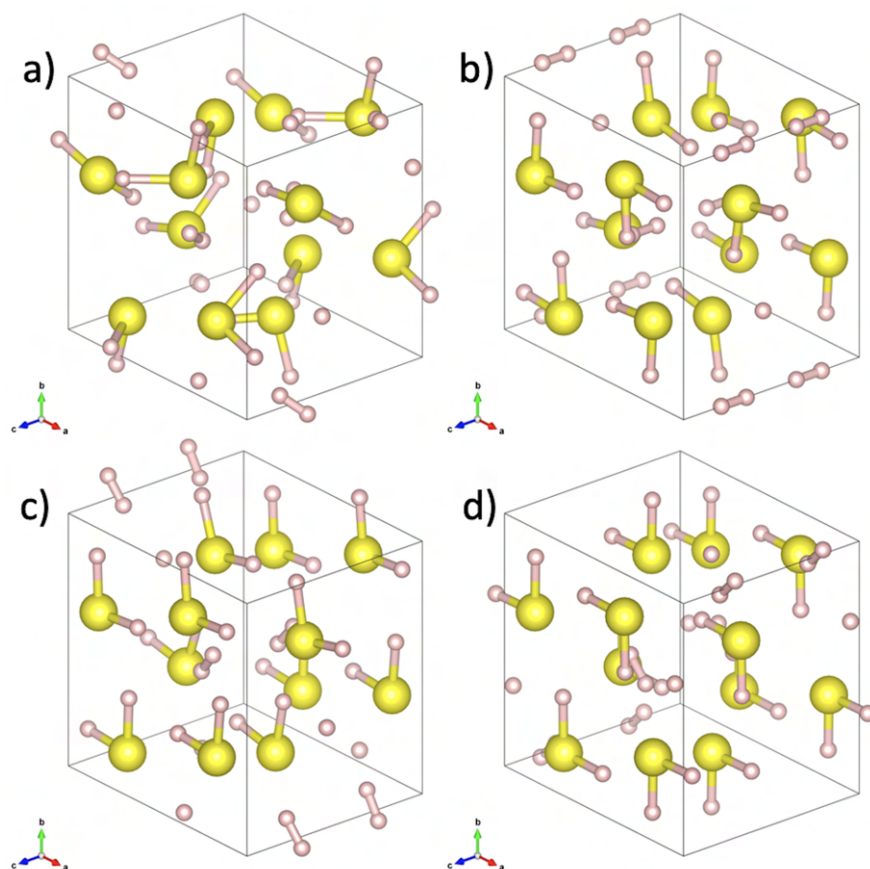


Figure B.17: The optimized versions of the 50 GPa  $I4/mcm$  (keeping the lattice and S positions fixed at their refined positions) structures shown in Fig. SB.16; the (a-d) numbering is the same. Note the  $\text{H}_2\text{S}$  molecular units in (b-d) remained planar following the optimization. The relative enthalpies are: (a) 0.000 eV, (b) 6.433 eV, (c) 5.057 eV, and (d) 4.605 eV. (d) is the most stable planar structure evaluated here. Credit: Keith Lawler, UNLV: Theory.

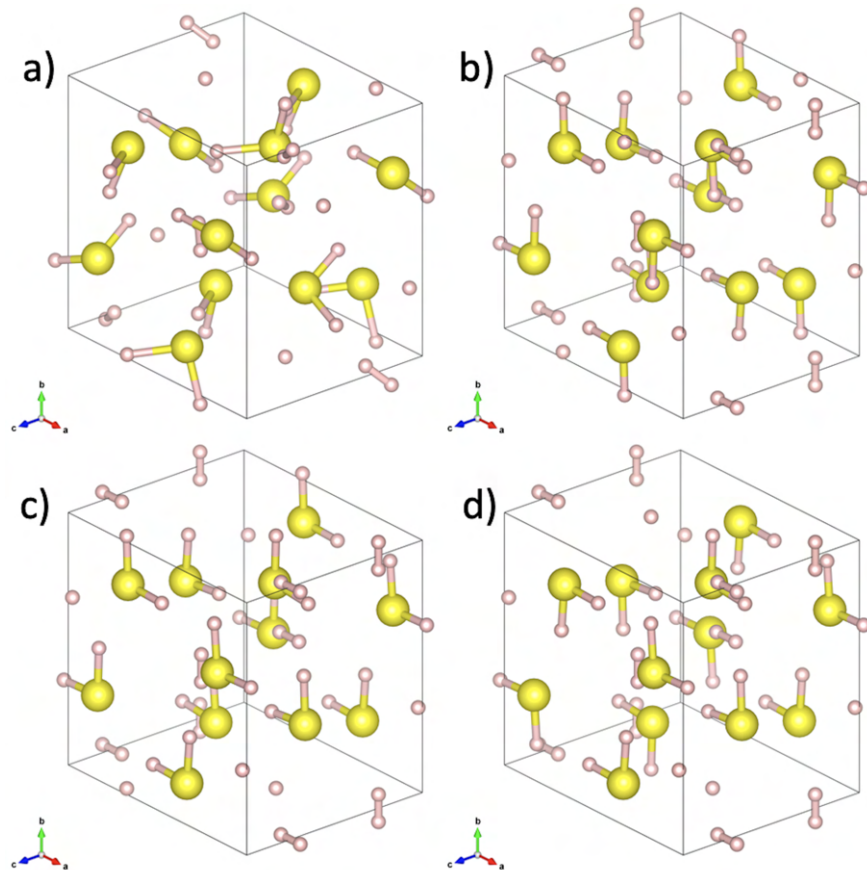


Figure B.18: 4 possible arrangements of the H<sub>2</sub>S units within the refined 9 GPa  $I4/mcm$  structure with the lattice and S positions fixed at their refined positions (Fig. 3a of the main text) and using the same H arrangements and (a-d) numbering as in Fig. SB.16. Credit: Keith Lawler, UNLV: Theory.

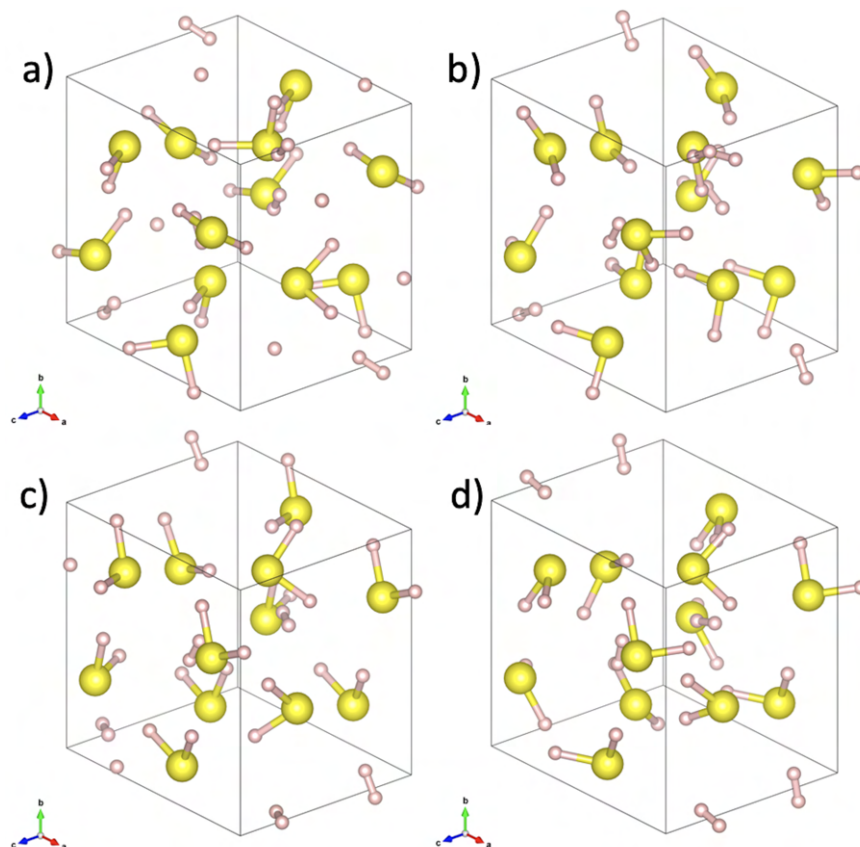


Figure B.19: The optimized versions of the 9 GPa  $I4/mcm$  (keeping the lattice and S positions fixed at their refined positions) structures shown in Fig. SB.18. The (a-d) numbering is the same. Note that some of the  $H_2S$  molecular units in each of (b-d) shifted away from being planar following the optimization. The relative enthalpies are: (a) 0.000 eV, (b) 1.136 eV, (c) 0.438 eV, and (d) 0.504 eV. Credit: Keith Lawler, UNLV: Theory.

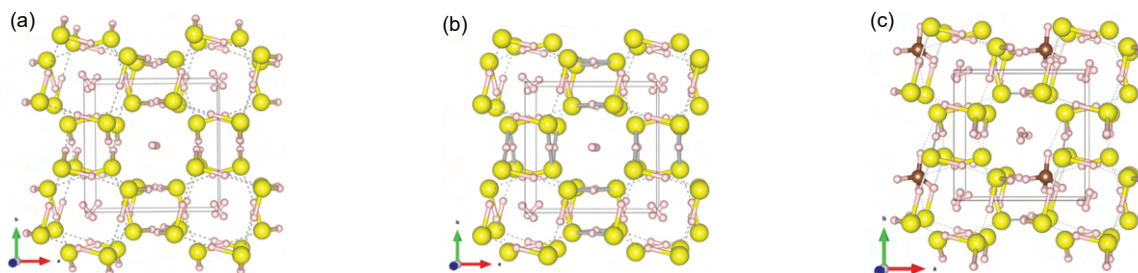

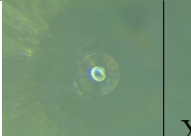
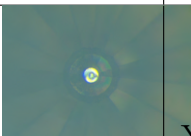
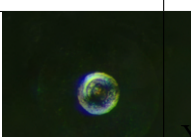


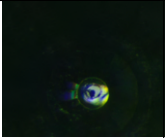
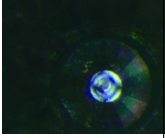
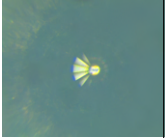


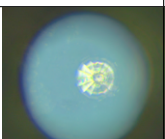
Figure B.20: (a) Lowest enthalpy DFT orientation of 50 GPa  $I4/mcm$   $(H_2S)_2H_2$  found here using the experimental unit cell and S positions. (b) The same configuration as (a) using the 90 GPa SC-XRD determined unit cell and S positions. (c) A higher enthalpy,  $\Delta H = 267$  meV per unit cell not vibrationally corrected, solution than Figure 3(e) in the main text but with  $H_2S$  molecular orientation more akin to what was found in (b). In (a-d), bicolor cylinders represent bonds ( $\le 1.43 \text{ \AA}$ ), silver single color cylinders represent H atoms shared between two heavy atoms (1.43-1.53  $\text{\AA}$ ), and dashed lines represent hydrogen bonds (1.53-2.0  $\text{\AA}$ ). Credit: Keith Lawler, UNLV: Theory.

## APPENDIX C


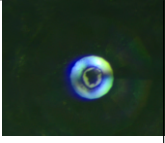
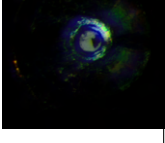
### SUPPLEMENTARY INFORMATION TO STOICHIOMETRIC DETERMINATION OF CLATHRATE-LIKE YTTRIUM HYDRIDES AT MEGABAR CONDITIONS

#### C.1 CELL LIST

Picture	Name	Sample	Pressures (GPa)	Phase	Laser heating	Run
	KES1	YH <sub>x</sub>	50-78	YH <sub>3</sub>	10 GPa	XES Run 1
	KES2	YH <sub>x</sub>	130	YH <sub>3</sub>	10, 130 GPa	XES Run 1
	KES3	YH <sub>x</sub>	11-83	YH <sub>3</sub>	10 GPa	XES Run 1
	KES4	YH <sub>x</sub>	10-49	YH <sub>2</sub>	None	XES Run 1

	KES5	$YH_x$	61-70	$YH_3$	10 GPa	XES Run 1
	KES6	Y metal	20-58	Y metal	None	XES Run 1
	PXES2	Y Metal	160	Y metal	160 Gpa	XES Run 2
	PXES4	$YH_x$	145	$YH_3$	10, 145 GPa	XES Run 2
	TF1	$YH_x$	194	$YH_3$	10, 194 GPa	XES Run 2
	M4	$YH_x$	147	$YH_4$	10, 147 GPa	XES Run 2

333

	SF8	$\text{YH}_x$	40	$\text{YH}_3$	10, 40 GPa	XES Run 2
	KES2	$\text{YH}_x$	7 - 28	$\text{YH}_2$ and $\text{YH}_3$	7 GPa	XES Run 2
	KES3	$\text{YH}_x$	22	$\text{YH}_3$	XFEL heating at 22 Gpa	XES Run 2

13 Cells were prepared for this experiment, included is a table describing their pressure conditions and heating. Credit: GA Smith, UNLV: DAC preparation.

## C.2 X-RAY SPECTROSCOPY

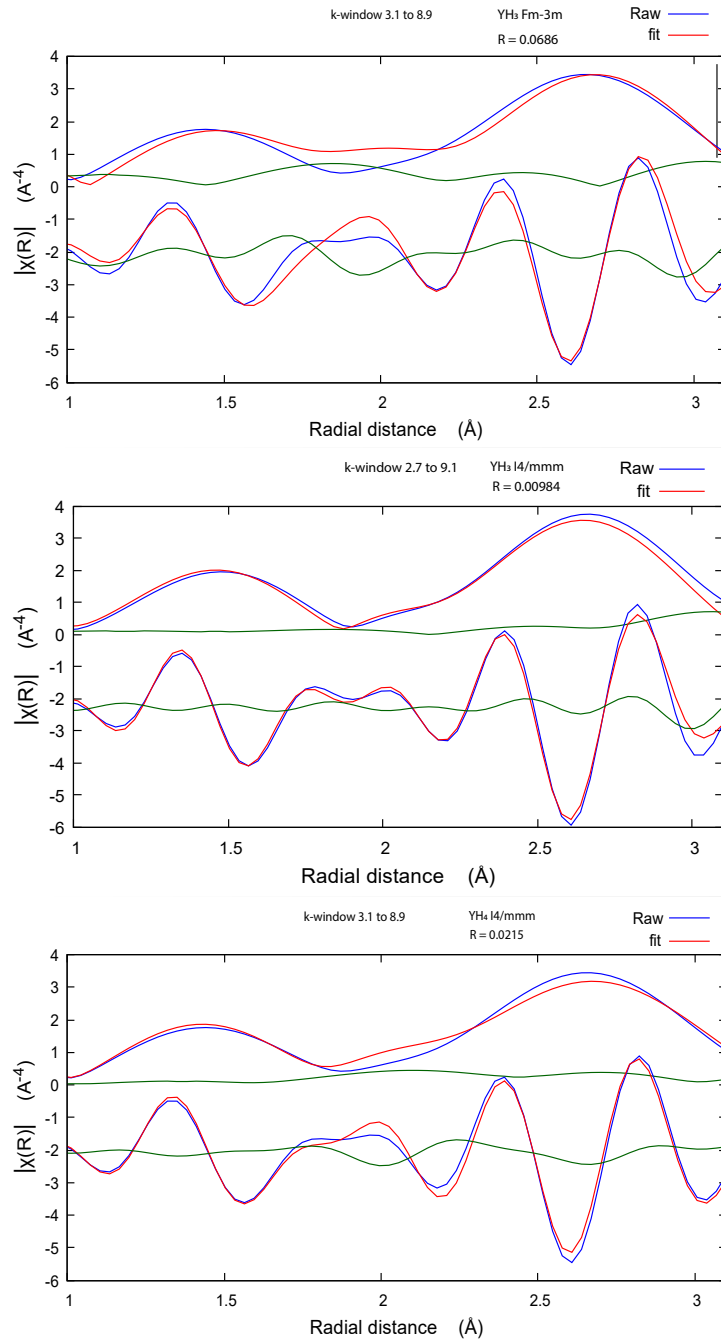


Figure C.1: A comparison of the EXAFS fits for the  $I4/mmm$   $\text{YH}_4$ ,  $I4/mmm$   $\text{YH}_3$ , and  $Fm\bar{3}m$ . The tetragonally distorted  $\text{YH}_3$  exhibits the lowest fit error. GA Smith, UNLV: XAS experiments.

XES was collected at ID20 at the ESRF. Scans were done using at 17.2 KeV using a van Hamos spectrometer. Normalized and background subtracted valence to core region of the XES spectra are presented below for experimental  $\text{YH}_2$ ,  $\text{YH}_3$ , and  $\text{YH}_4$

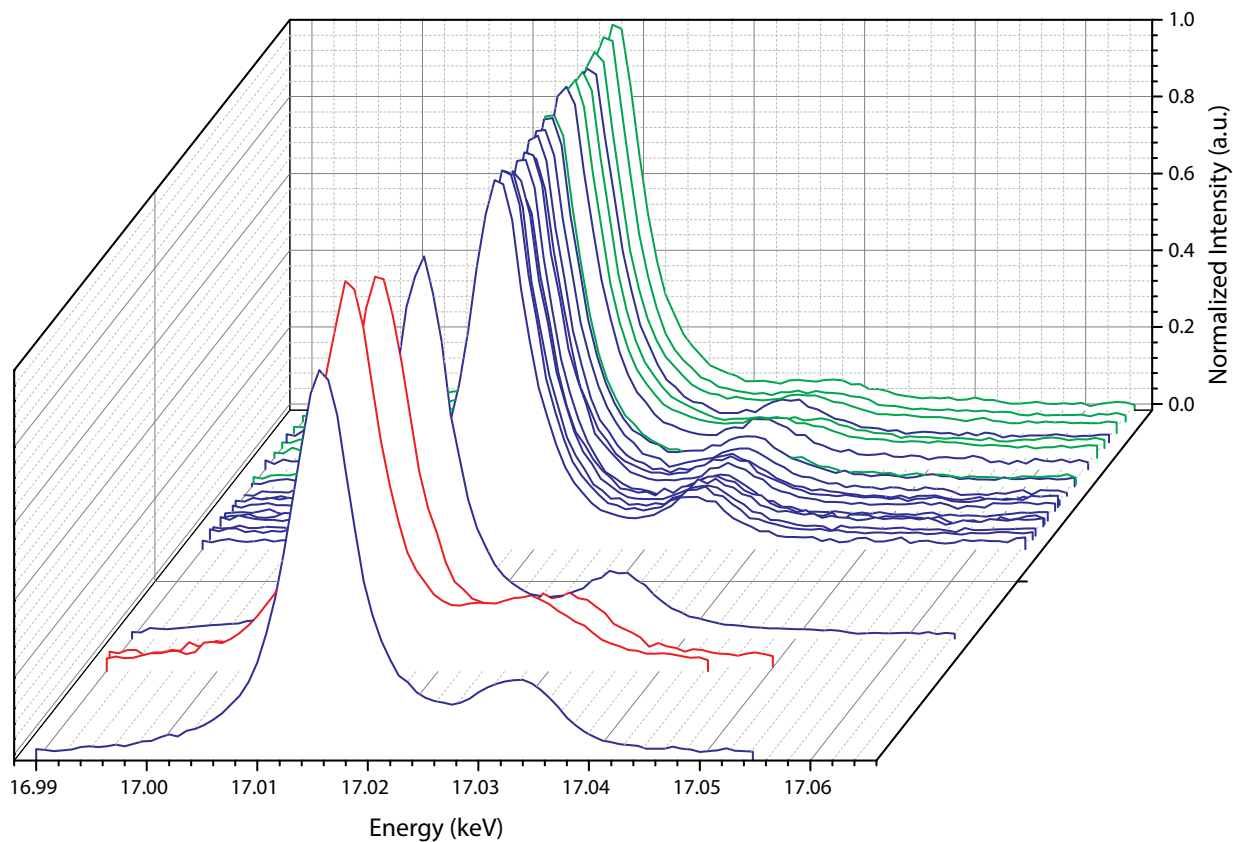


Figure C.2: A waterfall plot of the experimentally collected and reduced spectra. In this plot,  $\text{YH}_2$ ,  $\text{YH}_3$ , and  $\text{YH}_4$  are green, blue, and red respectively. Credit: GA Smith, UNLV: XES experiments.



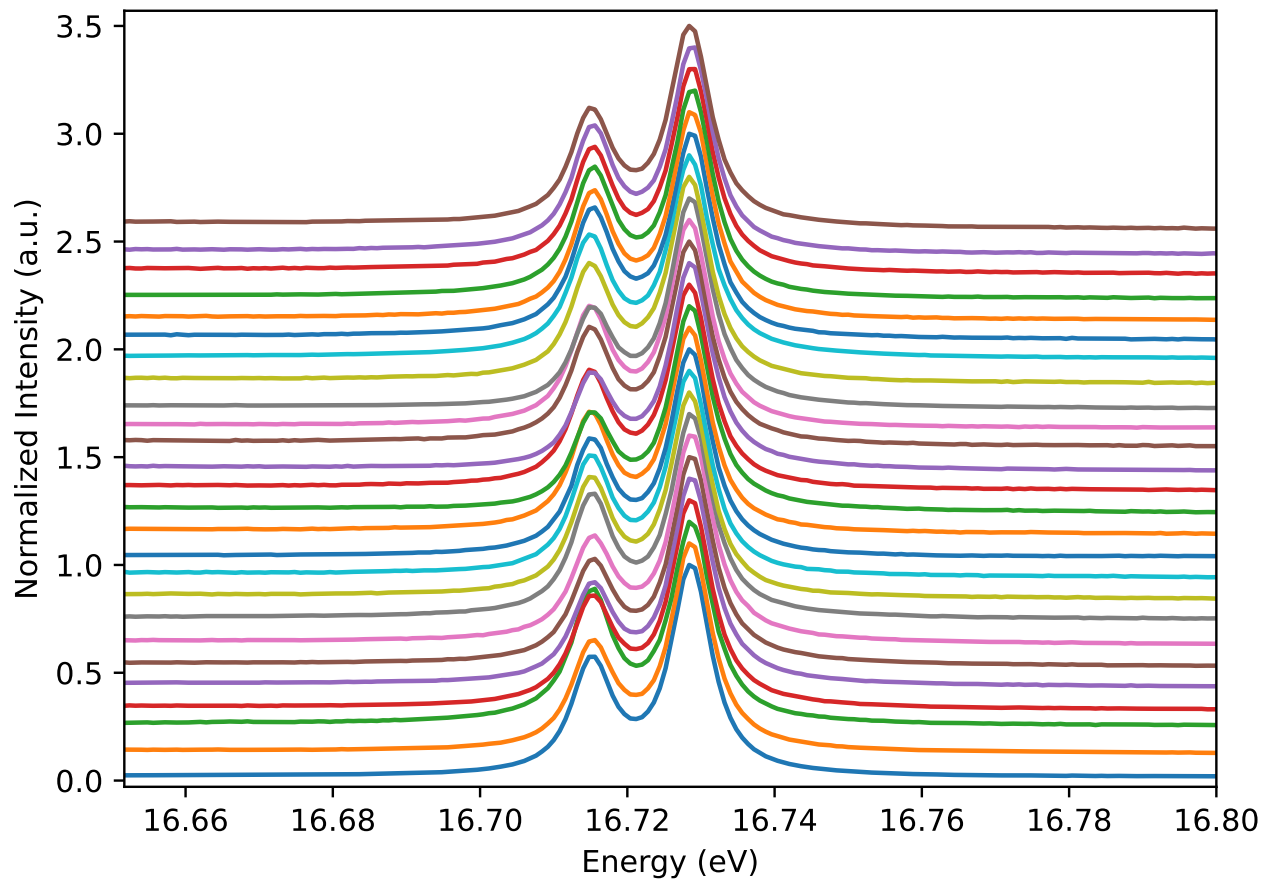


Figure C.3: A plot showing all collected  $K\beta_1$  and  $K\beta_3$  spectra of Y metal and  $YH_x$  samples between ambient and 2 Mbar. There is no apparent change. Between each figure is a 0.1 offset for comparison. Credit: GA Smith, UNLV: XES experiments.

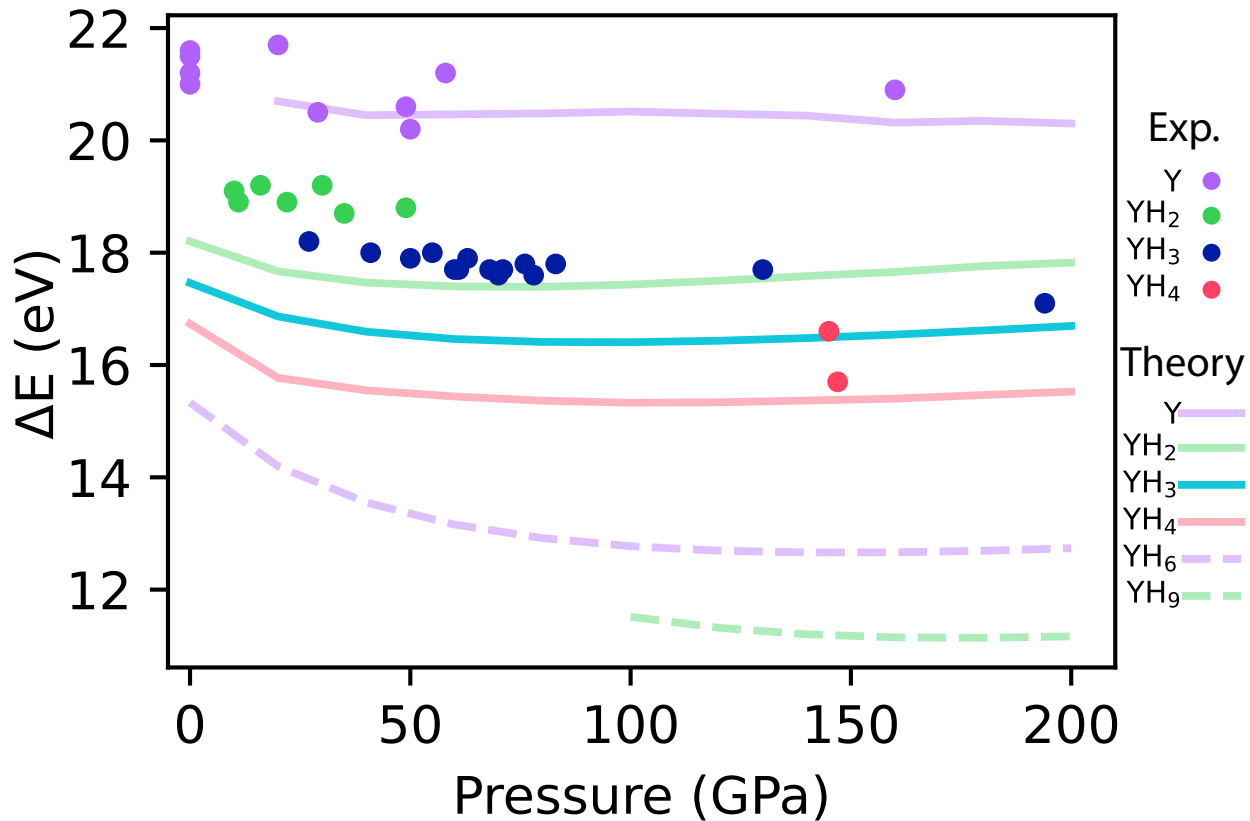


Figure C.4: The energy difference presented in Fig. 4.2 without the systematic 7.5% stretching in energy of theory. Credit: GA Smith, UNLV; XES experiments.

## BIBLIOGRAPHY

- [1] N. W. Ashcroft. “Metallic Hydrogen: A High-Temperature Superconductor?” In: *Physical Review Letters* 21.26 (1968), pp. 1748–1749. DOI: 10.1103/PhysRevLett.21.1748.
- [2] Ranga P. Dias and Isaac F. Silvera. “Observation of the Wigner-Huntington transition to metallic hydrogen”. In: *Science* 355.6326 (2017), pp. 715–718. DOI: 10.1126/science.aal1579.
- [3] Elliot Snider et al. “RETRACTED ARTICLE: Room-temperature superconductivity in a carbonaceous sulfur hydride”. en. In: *Nature* 586.78297829 (2020), pp. 373–377. ISSN: 1476-4687. DOI: 10.1038/s41586-020-2801-z.
- [4] Elliot Snider et al. “Synthesis of Yttrium Superhydride Superconductor with a Transition Temperature up to 262 K by Catalytic Hydrogenation at High Pressures”. In: *Physical Review Letters* 126.11 (2021), p. 117003. DOI: 10.1103/PhysRevLett.126.117003.
- [5] Maddury Somayazulu et al. “Evidence for Superconductivity above 260 K in Lanthanum Superhydride at Megabar Pressures”. In: *Physical Review Letters* 122.2 (2019), p. 027001. DOI: 10.1103/PhysRevLett.122.027001.
- [6] Nathan Dasenbrock-Gammon et al. “Evidence of near-ambient superconductivity in a N-doped lutetium hydride”. en. In: *Nature* 615.79517951 (2023), pp. 244–250. ISSN: 1476-4687. DOI: 10.1038/s41586-023-05742-0.
- [7] G. Alexander Smith et al. “Prevalence of pretransition disordering in the rutile-to- $\text{CaCl}_2$  phase transition of  $\text{GeO}_2$ ”. In: *Physical Review B* 104.13 (2021), p. 134107. DOI: 10.1103/PhysRevB.104.134107.

- [8] G. Alexander Smith et al. “Carbon content drives high temperature superconductivity in a carbonaceous sulfur hydride below 100 GPa”. en. In: *Chemical Communications* 58.65 (2022), pp. 9064–9067. ISSN: 1364-548X. DOI: 10.1039/D2CC03170A.
- [9] H Kamerlingh Onnes. “Contributions to the knowledge of the  $\psi$  surface of van der Waals. XI. A gas that sinks in a liquid”. In: *KNAW, Proceedings*. Vol. 9. 1906, pp. 459–460.
- [10] H Kamerlingh Onnes. “The superconductivity of mercury”. In: *Comm. Phys. Lab. Univ. Leiden* 122 (1911), p. 124.
- [11] Leon N Cooper. “Bound electron pairs in a degenerate Fermi gas”. In: *Physical Review* 104.4 (1956), p. 1189.
- [12] John Bardeen, Leon N Cooper, and J Robert Schrieffer. “Microscopic theory of superconductivity”. In: *Physical Review* 106.1 (1957), p. 162.
- [13] John Bardeen, Leon N Cooper, and John Robert Schrieffer. “Theory of superconductivity”. In: *Physical review* 108.5 (1957), p. 1175.
- [14] DK Finnemore, TF Stromberg, and CA Swenson. “Superconducting properties of high-purity niobium”. In: *Physical Review* 149.1 (1966), p. 231.
- [15] E Revolinsky, GA Spiering, and DJ Beerntsen. “Superconductivity in the niobium-selenium system”. In: *Journal of Physics and Chemistry of Solids* 26.6 (1965), pp. 1029–1034.
- [16] JG Daunt and JW Cobble. “Superconductivity of Technetium”. In: *Physical Review* 92.2 (1953), p. 507.
- [17] ST Sekula, RH Kernohan, and GR Love. “Superconducting properties of technetium”. In: *Physical Review* 155.2 (1967), p. 364.

- [18] R. J. Cava et al. “Superconductivity at 60 K in  $\text{La}_{2-x}\text{Sr}_x\text{CaCu}_2\text{O}_6$ : the simplest double-layer cuprate”. en. In: *Nature* 345.62766276 (1990), pp. 602–604. ISSN: 1476-4687. DOI: 10.1038/345602a0.
- [19] C. W. Chu et al. “Superconductivity at 52.5 K in the Lanthanum-Barium-Copper-Oxide System”. In: *Science* 235.4788 (1987), pp. 567–569. DOI: 10.1126/science.235.4788.567.
- [20] Emanuel I. Cooper, Edward A. Giess, and Arunava Gupta. “Bismuth strontium calcium copper oxide high- $T_c$  superconducting films from nitrate precursors”. en. In: *Materials Letters* 7.1 (1988), pp. 5–8. ISSN: 0167-577X. DOI: 10.1016/0167-577X(88)90069-9.
- [21] R. M. Hazen et al. “100-K superconducting phases in the Tl-Ca-Ba-Cu-O system”. In: *Physical Review Letters* 60.16 (1988), pp. 1657–1660. DOI: 10.1103/PhysRevLett.60.1657.
- [22] Henry Krakauer and Warren E. Pickett. “Effect of bismuth on high- $T_c$  cuprate superconductors: Electronic structure of  $\text{Bi}_2\text{Sr}_2\text{CaCu}_2\text{O}_8$ ”. In: *Physical Review Letters* 60.16 (1988), pp. 1665–1667. DOI: 10.1103/PhysRevLett.60.1665.
- [23] Yuejin Guo, Jean-Marc Langlois, and William A. Goddard. “Electronic Structure and Valence-Bond Band Structure of Cuprate Superconducting Materials”. In: *Science* 239.4842 (1988), pp. 896–899. DOI: 10.1126/science.239.4842.896.
- [24] D. W. Murphy et al. “New superconducting cuprate perovskites”. In: *Physical Review Letters* 58.18 (1987), pp. 1888–1890. DOI: 10.1103/PhysRevLett.58.1888.
- [25] A. Manthiram et al. “The influence of oxygen variation on the crystal structure and phase composition of the superconductor yttrium barium copper oxide ( $\text{YBa}_2\text{Cu}_3\text{O}_{7-x}$ )”. In: *Journal of the American Chemical Society* 109.22 (1987), pp. 6667–6669.

- [26] Nicolas Kowalski et al. “Oxygen hole content, charge-transfer gap, covalency, and cuprate superconductivity”. In: *Proceedings of the National Academy of Sciences* 118.40 (2021), e2106476118. DOI: 10.1073/pnas.2106476118.
- [27] Shane M. O’Mahony et al. “On the electron pairing mechanism of copper-oxide high temperature superconductivity”. In: *Proceedings of the National Academy of Sciences* 119.37 (2022), e2207449119. DOI: 10.1073/pnas.2207449119.
- [28] L. Gao. “Superconductivity up to 164 K in  $\text{HgBa}_2\text{Ca}_{m-1}\text{Cu}_m\text{O}_{2m+2}$  ( $m=1, 2,$  and  $3$ ) under quasihydrostatic pressures”. In: *Physical Review B* 50.6 (1994), pp. 4260–4263. DOI: 10.1103/PhysRevB.50.4260.
- [29] A. Schilling et al. “Superconductivity above 130 K in the Hg-Ba-Ca-Cu-O system”. en. In: *Nature* 363.64246424 (1993), pp. 56–58. ISSN: 1476-4687. DOI: 10.1038/363056a0.
- [30] A. P. Drozdov et al. “Conventional superconductivity at 203 kelvin at high pressures in the sulfur hydride system”. en. In: *Nature* 525.75677567 (2015), pp. 73–76. ISSN: 1476-4687. DOI: 10.1038/nature14964.
- [31] E. Wigner and H. B. Huntington. “On the Possibility of a Metallic Modification of Hydrogen”. In: *The Journal of Chemical Physics* 3.12 (1935), pp. 764–770. ISSN: 0021-9606. DOI: 10.1063/1.1749590.
- [32] R. Peierls. “On the Theory of the Diamagnetism of Conduction Electrons”. In: *Selected Scientific Papers of Sir Rudolf Peierls*. Vol. Volume 19. World Scientific Series in 20th Century Physics. Imperial College Press and World Scientific Publishing Co., 1997, pp. 97–120. ISBN: 978-981-02-2692-3. DOI: 10.1142/9789812795779\_0010. URL: [https://www.worldscientific.com/doi/abs/10.1142/9789812795779\\_0010](https://www.worldscientific.com/doi/abs/10.1142/9789812795779_0010).
- [33] M. I. Eremets et al. “Semimetallic molecular hydrogen at pressure above 350 GPa”. en. In: *Nature Physics* 15.1212 (2019), pp. 1246–1249. ISSN: 1745-2481. DOI: 10.1038/s41567-019-0646-x.

- [34] Lorenzo Monacelli et al. “Black metal hydrogen above 360 GPa driven by proton quantum fluctuations”. In: *Nature Physics* 17.1 (2021), pp. 63–67.
- [35] Paul Loubeyre, Florent Occelli, and Paul Dumas. “Synchrotron infrared spectroscopic evidence of the probable transition to metal hydrogen”. In: *Nature* 577.7792 (2020), pp. 631–635.
- [36] N. W. Ashcroft and N. D. Mermin. *Solid State Physics*. Holt-Saunders, 1976.
- [37] Charles Kittel. *Introduction to Solid State Physics*. 8th ed. Wiley, 2004. ISBN: 9780471415268.
- [38] David J Griffiths. *Introduction to electrodynamics*. Pearson, 2013.
- [39] J. D. Jackson. *Classical Electrodynamics*. Third. New York: Wiley, 1998.
- [40] Michael Tinkham. *Introduction to Superconductivity*. 2nd ed. Dover Publications, June 2004. ISBN: 0486435032. URL: <http://www.worldcat.org/isbn/0486435032>.
- [41] Wolfgang Pauli. “On the connexion between the completion of electron groups in an atom with the complex structure of spectra”. In: *Zeitschrift für Physik* 31 (1925), p. 765.
- [42] H. Q. Yuan et al. “*S*-Wave Spin-Triplet Order in Superconductors without Inversion Symmetry:  $\text{Li}_2\text{Pd}_3\text{B}$  and  $\text{Li}_2\text{Pt}_3\text{B}$ ”. In: *Physical Review Letters* 97.1 (2006), p. 017006. DOI: 10.1103/PhysRevLett.97.017006.
- [43] Qiangqiang Gu et al. “Directly visualizing the sign change of d-wave superconducting gap in  $\text{Bi}_2\text{Sr}_2\text{CaCu}_2\text{O}_{8+\delta}$  by phase-referenced quasiparticle interference”. en. In: *Nature Communications* 10.11 (2019), p. 1603. ISSN: 2041-1723. DOI: 10.1038/s41467-019-09340-5.
- [44] E. F. Talantsev et al. “p-wave superconductivity in iron-based superconductors”. en. In: *Scientific Reports* 9.11 (2019), p. 14245. ISSN: 2045-2322. DOI: 10.1038/s41598-019-50687-y.

- [45] AB Migdal. “Interaction between electrons and lattice vibrations in a normal metal”. In: *Sov. Phys. JETP* 7.6 (1958), pp. 996–1001.
- [46] GM Eliashberg. “Temperature Green’s function for electrons in a superconductor”. In: *Sov. Phys. JETP* 12.5 (1961), pp. 1000–1002.
- [47] P. B. Allen and R. C. Dynes. “Transition temperature of strong-coupled superconductors reanalyzed”. In: *Physical Review B* 12.3 (1975), pp. 905–922. DOI: 10.1103/PhysRevB.12.905.
- [48] P. Morel and P. W. Anderson. “Calculation of the Superconducting State Parameters with Retarded Electron-Phonon Interaction”. In: *Physical Review* 125.4 (1962), pp. 1263–1271. DOI: 10.1103/PhysRev.125.1263.
- [49] CE Weir et al. “Infrared studies in the 1-to 15-micron region to 30,000 atmospheres”. In: *Journal of research of the National Bureau of Standards. Section A, Physics and chemistry* 63.1 (1959), p. 55.
- [50] Leo Merrill and William A. Bassett. “Miniature diamond anvil pressure cell for single crystal x-ray diffraction studies”. In: *Review of Scientific Instruments* 45.2 (1974), pp. 290–294. ISSN: 0034-6748. DOI: 10.1063/1.1686607.
- [51] Russel J Hemley and HK Mao. “Optical studies of hydrogen above 200 Gigapascals: Evidence for metallization by band overlap”. In: *Science* 244.4911 (1989), pp. 1462–1465.
- [52] RL Mills et al. “Procedure for loading diamond cells with high-pressure gas”. In: *Review of Scientific Instruments* 51.7 (1980), pp. 891–895.
- [53] HK Mao et al. “Static compression of iron to 300 GPa and Fe<sub>0.8</sub>Ni<sub>0.2</sub> alloy to 260 GPa: Implications for composition of the core”. In: *Journal of Geophysical Research: Solid Earth* 95.B13 (1990), pp. 21737–21742.
- [54] Aiyasami Jayaraman. “Diamond anvil cell and high-pressure physical investigations”. In: *Reviews of Modern Physics* 55.1 (1983), p. 65.



- [55] Bianca Haberl, Malcolm Guthrie, and Reinhard Boehler. “Advancing neutron diffraction for accurate structural measurement of light elements at megabar pressures”. en. In: *Scientific Reports* 13.11 (2023), p. 4741. ISSN: 2045-2322. DOI: 10.1038/s41598-023-31295-3.
- [56] N. W. Ashcroft. “Hydrogen Dominant Metallic Alloys: High Temperature Superconductors?” In: *Physical Review Letters* 92.18 (2004), p. 187002. DOI: 10.1103/PhysRevLett.92.187002.
- [57] Hui Wang et al. “Superconductive sodalite-like clathrate calcium hydride at high pressures”. In: *Proceedings of the National Academy of Sciences* 109.17 (2012), pp. 6463–6466. DOI: 10.1073/pnas.1118168109.
- [58] Yinwei Li et al. “Pressure-stabilized superconductive yttrium hydrides”. In: *Scientific Reports* 5.1 (2015), pp. 1–8.
- [59] Hanyu Liu et al. “Potential high-Tc superconducting lanthanum and yttrium hydrides at high pressure”. In: *Proceedings of the National Academy of Sciences* 114.27 (2017), pp. 6990–6995. DOI: 10.1073/pnas.1704505114.
- [60] Feng Peng et al. “Hydrogen Clathrate Structures in Rare Earth Hydrides at High Pressures: Possible Route to Room-Temperature Superconductivity”. In: *Physical Review Letters* 119.10 (2017), p. 107001. DOI: 10.1103/PhysRevLett.119.107001.
- [61] Eva Zurek et al. “A little bit of lithium does a lot for hydrogen”. In: *Proceedings of the National Academy of Sciences* 106.42 (2009), pp. 17640–17643. DOI: 10.1073/pnas.0908262106.
- [62] Dmitry V. Semenov et al. “Superconductivity at 161 K in thorium hydride ThH<sub>10</sub>: Synthesis and properties”. en. In: *Materials Today* 33 (2020), pp. 36–44. ISSN: 1369-7021. DOI: 10.1016/j.mattod.2019.10.005.

- [63] Liang Ma et al. “High-Temperature Superconducting Phase in Clathrate Calcium Hydride  $\text{CaH}_6$  up to 215 K at a Pressure of 172 GPa”. In: *Physical Review Letters* 128.16 (2022), p. 167001. DOI: 10.1103/PhysRevLett.128.167001.
- [64] Israel Osmond et al. “Clean-limit superconductivity in  $Im\bar{3}m$   $\text{H}_3\text{S}$  synthesized from sulfur and hydrogen donor ammonia borane”. In: *Physical Review B* 105.22 (2022), p. L220502. DOI: 10.1103/PhysRevB.105.L220502.
- [65] V. L. Ginzburg and L. D. Landau. “On the theory of superconductivity”. In: *Zh. Eksp. Teor. Fiz.* 20 (1950), pp. 1064–1082.
- [66] Elliot Snider et al. *Retraction Note: Room-temperature superconductivity in a carbonaceous sulfur hydride*. 2022. URL: <https://www.nature.com/articles/s41586-022-05294-9>.
- [67] Panpan Kong et al. “Superconductivity up to 243 K in the yttrium-hydrogen system under high pressure”. en. In: *Nature Communications* 12.11 (2021), p. 5075. ISSN: 2041-1723. DOI: 10.1038/s41467-021-25372-2.
- [68] Dmitrii V. Semenov et al. “Superconductivity at 253 K in lanthanum-yttrium ternary hydrides”. en. In: *Materials Today* 48 (2021), pp. 18–328. ISSN: 1369-7021. DOI: 10.1016/j.mattod.2021.03.025.
- [69] S Villa-Cortés et al. “The Isotope Effect and Critical Magnetic Fields of Superconducting  $\text{YH}_6$ : A Migdal-Eliashberg Theory Approach”. In: *arXiv preprint arXiv:2302.12988* (2023).
- [70] Cristina Buzea and Kevin Robbie. “Assembling the puzzle of superconducting elements: a review”. en. In: *Superconductor Science and Technology* 18.1 (2004), R1. ISSN: 0953-2048. DOI: 10.1088/0953-2048/18/1/R01.
- [71] Jun Nagamatsu et al. “Superconductivity at 39 K in magnesium diboride”. In: *nature* 410.6824 (2001), pp. 63–64.

- [72] GW Webb, F Marsiglio, and JE Hirsch. “Superconductivity in the elements, alloys and simple compounds”. In: *Physica C: Superconductivity and its applications* 514 (2015), pp. 17–27.
- [73] Nikolay Plakida. *High-temperature cuprate superconductors: Experiment, theory, and applications*. Vol. 166. Springer Science & Business Media, 2010.
- [74] BW Batterman and CS Barrett. “Crystal structure of superconducting  $V_3Si$ ”. In: *Physical Review Letters* 13.13 (1964), p. 390.
- [75] Yundi Quan, Soham S. Ghosh, and Warren E. Pickett. “Compressed hydrides as metallic hydrogen superconductors”. In: *Physical Review B* 100.18 (2019), p. 184505. DOI: 10.1103/PhysRevB.100.184505.
- [76] CA (USA) Lawrence Berkeley Lab. *X-ray data booklet Revision*. LBL-PUB-490-Rev. United States, 1986, p. 154. URL: [http://inis.iaea.org/search/search.aspx?orig\\_q=RN:18000214](http://inis.iaea.org/search/search.aspx?orig_q=RN:18000214).
- [77] John S. C. Kearney et al. “Pressure-Tuneable Visible-Range Band Gap in the Ionic Spinel Tin Nitride”. en. In: *Angewandte Chemie International Edition* 57.36 (2018), pp. 11623–11628. ISSN: 1521-3773. DOI: 10.1002/anie.201805038.
- [78] Zachary M. Geballe et al. “Synthesis and Stability of Lanthanum Superhydrides”. en. In: *Angewandte Chemie* 130.3 (2018), pp. 696–700. ISSN: 1521-3757. DOI: 10.1002/ange.201709970.
- [79] Yanlu Li et al. “Optical Properties of the High-Pressure Phases of  $SnO_2$ : First-Principles Calculation”. In: *The Journal of Physical Chemistry A* 114.2 (2010), pp. 1052–1059. DOI: 10.1021/jp909021r.
- [80] W. Kohn and L. J. Sham. “Self-Consistent Equations Including Exchange and Correlation Effects”. In: *Phys. Rev.* 140 (4A 1965), A1133–A1138. DOI: 10.1103/PhysRev.140.A1133. URL: <https://link.aps.org/doi/10.1103/PhysRev.140.A1133>.

- [81] Riccardo Sabatini, Tommaso Gorni, and Stefano de Gironcoli. “Nonlocal van der Waals density functional made simple and efficient”. In: *Phys. Rev. B* 87 (4 2013), p. 041108. DOI: 10.1103/PhysRevB.87.041108. URL: <https://link.aps.org/doi/10.1103/PhysRevB.87.041108>.
- [82] Jianwei Sun, Adrienn Ruzsinszky, and John P. Perdew. “Strongly Constrained and Appropriately Normed Semilocal Density Functional”. In: *Phys. Rev. Lett.* 115 (3 2015), p. 036402. DOI: 10.1103/PhysRevLett.115.036402. URL: <https://link.aps.org/doi/10.1103/PhysRevLett.115.036402>.
- [83] Haowei Peng et al. “Versatile van der Waals Density Functional Based on a Meta-Generalized Gradient Approximation”. In: *Phys. Rev. X* 6 (4 2016), p. 041005. DOI: 10.1103/PhysRevX.6.041005. URL: <https://link.aps.org/doi/10.1103/PhysRevX.6.041005>.
- [84] B. Hammer, L. B. Hansen, and J. K. Nørskov. “Improved adsorption energetics within density-functional theory using revised Perdew-Burke-Ernzerhof functionals”. In: *Physical Review B* 59.11 (1999), pp. 7413–7421. DOI: 10.1103/PhysRevB.59.7413.
- [85] John Vinson. “Advances in the OCEAN-3 spectroscopy package”. en. In: *Physical Chemistry Chemical Physics* 24.21 (2022), pp. 12787–12803. ISSN: 1463-9084. DOI: 10.1039/D2CP01030E.
- [86] Dean Smith et al. “Anomalous Conductivity in the Rutile Structure Driven by Local Disorder”. In: *The Journal of Physical Chemistry Letters* 10.18 (2019), pp. 5351–5356. DOI: 10.1021/acs.jpcllett.9b01633. URL: <https://doi.org/10.1021/acs.jpcllett.9b01633>.
- [87] Elena Bykova et al. “Structure and composition of C-S-H compounds up to 143 GPa”. In: *Physical Review B* 103.14 (2021), p. L140105. DOI: 10.1103/PhysRevB.103.L140105.
- [88] LE Crandall et al. “Equation of state of C<sub>2</sub> shock compressed to 1 TPa”. In: *Physical Review Letters* 125.16 (2020), p. 165701.

- [89] A Fernandez-Pañella et al. “Shock compression of liquid deuterium up to 1 TPa”. In: *Physical Review Letters* 122.25 (2019), p. 255702.
- [90] Seth Root et al. “Argon equation of state data to 1 TPa: Shock compression experiments and simulations”. In: *Physical Review B* 106.17 (2022), p. 174114.
- [91] Leonid Dubrovinsky et al. “Materials synthesis at terapascal static pressures”. en. In: *Nature* 605.79097909 (2022), pp. 274–278. ISSN: 1476-4687. DOI: 10.1038/s41586-022-04550-2.
- [92] Jasmine K. Hinton et al. “Response of the mode Grüneisen parameters with anisotropic compression: A pressure and temperature dependent Raman study of  $\beta$ -Sn”. In: *Physical Review B* 102.18 (2020), p. 184112. DOI: 10.1103/PhysRevB.102.184112.
- [93] Johannes M. Kaa et al. “Structural and electron spin state changes in an x-ray heated iron carbonate system at the Earth’s lower mantle pressures”. In: *Physical Review Research* 4.3 (2022), p. 033042. DOI: 10.1103/PhysRevResearch.4.033042.
- [94] G. Spiekermann et al. “Persistent Octahedral Coordination in Amorphous  $\text{GeO}_2$  Up to 100 GPa by  $K\beta$  X-Ray Emission Spectroscopy”. In: *Physical Review X* 9.1 (2019), p. 011025. DOI: 10.1103/PhysRevX.9.011025.
- [95] S Tse John et al. “X-ray Raman spectroscopic study of water in the condensed phases”. In: *Physical review letters* 100.9 (2008), p. 095502.
- [96] Alba SJ Méndez et al. “A resistively-heated dynamic diamond anvil cell (RHdDAC) for fast compression x-ray diffraction experiments at high temperatures”. In: *Review of scientific instruments* 91.7 (2020), p. 073906.
- [97] Daniel Metzner et al. “Experimental and Theoretical Determination of the Effective Penetration Depth of Ultrafast Laser Radiation in Stainless Steel”. en. In: *Lasers in Manufacturing and Materials Processing* 7.4 (2020), pp. 478–495. ISSN: 2196-7237. DOI: 10.1007/s40516-020-00129-9.

- [98] Dean Smith et al. “A CO<sub>2</sub> laser heating system for in situ high pressure-temperature experiments at HPCAT”. In: *Review of Scientific Instruments* 89.8 (2018). ISSN: 10897623. DOI: 10.1063/1.5040508.
- [99] Sylvain Petitgirard et al. “Strategies for in situ laser heating in the diamond anvil cell at an X-ray diffraction beamline”. In: *Journal of Synchrotron Radiation* 21.1 (2014). Publisher: International Union of Crystallography ISBN: 1600577513027, pp. 89–96. ISSN: 09090495. DOI: 10.1107/S1600577513027434.
- [100] J. Als-Nielsen and D. McMorrow. *Elements of Modern X-Ray Physics*. New York: Wiley, 2000.
- [101] William Henry Bragg and William Lawrence Bragg. “The reflection of X-rays by crystals”. In: *Proceedings of the Royal Society of London. Series A, Containing Papers of a Mathematical and Physical Character* 88.605 (1913), pp. 428–438.
- [102] J. Franck and E. G. Dymond. “Elementary processes of photochemical reactions”. In: *Transactions of the Faraday Society* 21.February (1926), pp. 536–542. ISSN: 0014-7672. DOI: 10.1039/TF9262100536.
- [103] Edward Condon. “A Theory of Intensity Distribution in Band Systems”. In: *Physical Review* 28.6 (1926), pp. 1182–1201. DOI: 10.1103/PhysRev.28.1182.
- [104] Edward U. Condon. “Nuclear Motions Associated with Electron Transitions in Diatomic Molecules”. In: *Physical Review* 32.6 (1928), pp. 858–872. DOI: 10.1103/PhysRev.32.858.
- [105] Peter William Atkins. *Physical Chemistry*. Fourth. New York: W. H. Freeman and Company, 1990.
- [106] M. Born and R. Oppenheimer. “On the quantum theory of molecules”. In: *Quantum Chemistry*. Vol. Volume 8. World Scientific Series in 20th Century Chemistry. World Scientific, 2000, pp. 1–24. ISBN: 978-981-02-2771-5. DOI: 10.1142/9789812795762\_0001. URL: [https://www.worldscientific.com/doi/abs/10.1142/9789812795762\\_0001](https://www.worldscientific.com/doi/abs/10.1142/9789812795762_0001).

- [107] Takashi Tokushima. “Developments of a Liquid Flow Cell for Soft x-ray Spectroscopy and Observations of Water Molecules in Liquid Solutions”. In: *Molecular Science* 9.1 (2015), A0077. DOI: 10.3175/molsci.9.A0077.
- [108] Scott Calvin. *Xafs for everyone*. CRC Press, 2013.
- [109] Grant Bunker. *Introduction to XAFS: A practical guide to X-ray absorption fine structure spectroscopy*. Cambridge University Press, 2010.
- [110] O Fuchs et al. “Isotope and temperature effects in liquid water probed by X-ray absorption and resonant X-ray emission spectroscopy”. In: *Physical review letters* 100.2 (2008), p. 027801.
- [111] FMF De Groot et al. “Oxygen 1s x-ray-absorption edges of transition-metal oxides”. In: *Physical Review B* 40.8 (1989), p. 5715.
- [112] Bruce Ravel et al. “Nonresonant valence-to-core X-ray emission spectroscopy of niobium”. In: *Physical Review B* 97.12 (2018), p. 125139.
- [113] Uwe Bergmann and Pieter Glatzel. “X-ray emission spectroscopy”. In: *Photosynthesis research* 102 (2009), pp. 255–266.
- [114] Manne Siegbahn. *The Spectroscopy of X-rays*. Vol. 10. Oxford University Press, H. Milford, 1925.
- [115] R Jenkins et al. “IUPAC-nomenclature system for x-ray spectroscopy”. In: *X-Ray Spectrometry* 20.3 (1991), pp. 149–155.
- [116] Frédéric Datchi et al. “Structure and compressibility of the high-pressure molecular phase II of carbon dioxide”. In: *Phys. Rev. B* 89 (14 2014), p. 144101. DOI: 10.1103/PhysRevB.89.144101.
- [117] V.P Prakapenka et al. “High pressure induced phase transformation of SiO<sub>2</sub> and GeO<sub>2</sub>: difference and similarity”. In: *Journal of Physics and Chemistry of Solids* 65.8 (2004), pp. 1537 –1545. ISSN: 0022-3697. DOI: <https://doi.org/10.1016/j.jpcs.2003.12.019>.

- [118] J. Haines et al. “Structural evolution of rutile-type and  $\text{CaCl}_2$ -type germanium dioxide at high pressure”. In: *Physics and Chemistry of Minerals* 27.8 (2000), pp. 575–582. DOI: 10.1007/s002690000092.
- [119] J. Haines and J. M. Léger. “X-ray diffraction study of the phase transitions and structural evolution of tin dioxide at high pressure: Relationships between structure types and implications for other rutile-type dioxides”. In: *Phys. Rev. B* 55 (17 1997), pp. 11144–11154. DOI: 10.1103/PhysRevB.55.11144.
- [120] J Haines, J M Léger, and O Schulte. “The high-pressure phase transition sequence from the rutile-type through to the cotunnite-type structure in  $\text{PbP}_2$ ”. In: *Journal of Physics: Condensed Matter* 8.11 (1996), pp. 1631–1646. DOI: 10.1088/0953-8984/8/11/009.
- [121] Johannes Buchen et al. “Equation of State of Polycrystalline Stishovite Across the Tetragonal-Orthorhombic Phase Transition”. In: *Journal of Geophysical Research: Solid Earth* 123.9 (2018), pp. 7347–7360. DOI: <https://doi.org/10.1029/2018JB015835>. URL: <https://agupubs.onlinelibrary.wiley.com/doi/abs/10.1029/2018JB015835>.
- [122] Atsushi Togo, Fumiyasu Oba, and Isao Tanaka. “First-principles calculations of the ferroelastic transition between rutile-type and  $\text{CaCl}_2$ -type  $\text{SiO}_2$  at high pressures”. In: *Phys. Rev. B* 78 (13 2008), p. 134106. DOI: 10.1103/PhysRevB.78.134106. URL: <https://link.aps.org/doi/10.1103/PhysRevB.78.134106>.
- [123] A. E. Ringwood and Merren Seabrook. “High-pressure phase transformations in germanate pyroxenes and related compounds”. In: *Journal of Geophysical Research (1896-1977)* 68.15 (1963), pp. 4601–4609. DOI: <https://doi.org/10.1029/JZ068i015p04601>. URL: <https://agupubs.onlinelibrary.wiley.com/doi/abs/10.1029/JZ068i015p04601>.
- [124] A.E. Ringwood. “Phase transformations and their bearing on the constitution and dynamics of the mantle”. In: *Geochimica et Cosmochimica Acta* 55.8 (1991), pp. 2083–2110. DOI: [https://doi.org/10.1016/0016-7037\(91\)90090-R](https://doi.org/10.1016/0016-7037(91)90090-R).



- [125] J. Y. Tsao et al. “Ultrawide-Bandgap Semiconductors: Research Opportunities and Challenges”. In: *Advanced Electronic Materials* 4.1 (2018), p. 1600501. DOI: 10.1002/aelm.201600501.
- [126] M. Stapelbroek and B.D. Evans. “Exciton structure in the u.v.-absorption edge of tetragonal GeO<sub>2</sub>”. In: *Solid State Communications* 25.11 (1978), pp. 959–962. ISSN: 0038-1098. DOI: [https://doi.org/10.1016/0038-1098\(78\)90311-3](https://doi.org/10.1016/0038-1098(78)90311-3). URL: <http://www.sciencedirect.com/science/article/pii/0038109878903113>.
- [127] Kelsey A. Mengle, Sieun Chae, and Emmanouil Kioupakis. “Quasiparticle band structure and optical properties of rutile GeO<sub>2</sub>, an ultra-wide-band-gap semiconductor”. In: *Journal of Applied Physics* 126.8 (2019), p. 085703. DOI: 10.1063/1.5111318.
- [128] Joo-Yeon Shin et al. “Fundamental Characteristics of Deep-UV Light-Emitting Diodes and Their Application To Control Foodborne Pathogens”. In: *Applied and Environmental Microbiology* 82.1 (2016). Ed. by C. A. Elkins, pp. 2–10. DOI: 10.1128/AEM.01186-15.
- [129] S. R. M. da Silva et al. “Oxygen transport and GeO<sub>2</sub> stability during thermal oxidation of Ge”. In: *Applied Physics Letters* 100.19 (2012), p. 191907. DOI: 10.1063/1.4712619.
- [130] Yoshiki Kamata. “High-k/Ge MOSFETs for future nanoelectronics”. In: *Materials Today* 11.1 (2008), pp. 30–38. ISSN: 1369-7021. DOI: [https://doi.org/10.1016/S1369-7021\(07\)70350-4](https://doi.org/10.1016/S1369-7021(07)70350-4). URL: <http://www.sciencedirect.com/science/article/pii/S1369702107703504>.
- [131] S. Chae et al. “Rutile GeO<sub>2</sub>: An ultrawide-band-gap semiconductor with ambipolar doping”. In: *Applied Physics Letters* 114.10 (2019), p. 102104. DOI: 10.1063/1.5088370. URL: <https://doi.org/10.1063/1.5088370>.
- [132] Denis Andrault et al. “Equation of state of stishovite to lower mantle pressures”. In: *American Mineralogist* 88.2-3 (Feb. 2003), pp. 301–307. DOI: 10.2138/am-2003-2-307.

- [133] Agnes Dewaele et al. “Compression curves of transition metals in the Mbar range: Experiments and projector augmented-wave calculations”. In: *Phys. Rev. B* 78 (10 2008), p. 104102. DOI: 10.1103/PhysRevB.78.104102. URL: <https://link.aps.org/doi/10.1103/PhysRevB.78.104102>.
- [134] B. Ravel and M. Newville. “*ATHENA, ARTEMIS, HEPHAESTUS*: data analysis for X-ray absorption spectroscopy using *IFEFFIT*”. In: *Journal of Synchrotron Radiation* 12.4 (2005), pp. 537–541. DOI: 10.1107/S0909049505012719. URL: <https://doi.org/10.1107/S0909049505012719>.
- [135] John J. Rehr et al. “Ab initio theory and calculations of X-ray spectra”. In: *Comptes Rendus Physique* 10.6 (2009). Theoretical spectroscopy, pp. 548–559. ISSN: 1631-0705. DOI: <https://doi.org/10.1016/j.crhy.2008.08.004>. URL: <https://www.sciencedirect.com/science/article/pii/S1631070508001084>.
- [136] J. G. Brandenburg et al. “Benchmark tests of a strongly constrained semilocal functional with a long-range dispersion correction”. In: *Phys. Rev. B* 94 (11 2016), p. 115144. DOI: 10.1103/PhysRevB.94.115144. URL: <https://link.aps.org/doi/10.1103/PhysRevB.94.115144>.
- [137] Stefan Grimme et al. “A consistent and accurate ab initio parametrization of density functional dispersion correction (DFT-D) for the 94 elements H-Pu”. In: *The Journal of Chemical Physics* 132.15 (2010), p. 154104. DOI: 10.1063/1.3382344.
- [138] Lars Goerigk and Stefan Grimme. “A thorough benchmark of density functional methods for general main group thermochemistry, kinetics, and noncovalent interactions”. In: *Phys. Chem. Chem. Phys.* 13 (14 2011), pp. 6670–6688. DOI: 10.1039/C0CP02984J. URL: <http://dx.doi.org/10.1039/C0CP02984J>.
- [139] James D. Pack and Hendrik J. Monkhorst. “Special points for Brillouin-zone integrations”—a reply”. In: *Phys. Rev. B* 16 (4 1977), pp. 1748–1749. DOI: 10.1103/PhysRevB.16.1748. URL: <https://link.aps.org/doi/10.1103/PhysRevB.16.1748>.

- [140] Peter E. Blöchl, O. Jepsen, and O. K. Andersen. “Improved tetrahedron method for Brillouin-zone integrations”. In: *Phys. Rev. B* 49 (23 1994), pp. 16223–16233. DOI: 10.1103/PhysRevB.49.16223. URL: <https://link.aps.org/doi/10.1103/PhysRevB.49.16223>.
- [141] P. E. Blöchl. “Projector augmented-wave method”. In: *Phys. Rev. B* 50 (24 1994), pp. 17953–17979. DOI: 10.1103/PhysRevB.50.17953. URL: <https://link.aps.org/doi/10.1103/PhysRevB.50.17953>.
- [142] Kurt Lejaeghere et al. “Reproducibility in density functional theory calculations of solids”. In: *Science* 351.6280 (2016). DOI: 10.1126/science.aad3000.
- [143] Alex M. Ganose, Adam J. Jackson, and David O. Scanlon. “sumo: Command-line tools for plotting and analysis of periodic \*ab initio\* calculations”. In: *Journal of Open Source Software* 3.28 (2018), p. 717. DOI: 10.21105/joss.00717. URL: <https://doi.org/10.21105/joss.00717>.
- [144] Agnes Dewaele and Paul Loubeyre. “Pressurizing conditions in helium pressure-transmitting medium”. In: *High Pressure Research* 27.4 (2007), pp. 419–429. DOI: 10.1080/08957950701659627.
- [145] Beatriz Cordero et al. “Covalent radii revisited”. In: *Dalton Trans.* (21 2008), pp. 2832–2838. DOI: 10.1039/B801115J.
- [146] Paolo Fornasini, Francesca Monti, and Andrea Sanson. “On the cumulant analysis of EXAFS in crystalline solids”. In: *Journal of Synchrotron Radiation* 8.6 (2001), pp. 1214–1220. DOI: 10.1107/S0909049501014923.
- [147] Richard H. Bube. *Electrons In Solids: An Introductory Survey*. Second. Cambridge, Massachusetts: Academic Press, 1988. ISBN: 0121385523. DOI: 10.1016/b978-0-12-138552-1.x5001-9.
- [148] O. W. Johnson, W. D. Ohlsen, and Paul I. Kingsbury. “Defects in Rutile. III. Optical and Electrical Properties of Impurities and Charge Carriers”. In: *Phys. Rev.* 175 (3

- 1968), pp. 1102–1109. DOI: 10.1103/PhysRev.175.1102. URL: <https://link.aps.org/doi/10.1103/PhysRev.175.1102>.
- [149] N. Aaron Deskins and Michel Dupuis. “Electron transport via polaron hopping in bulk TiO<sub>2</sub>: A density functional theory characterization”. In: *Phys. Rev. B* 75 (19 2007), p. 195212. DOI: 10.1103/PhysRevB.75.195212. URL: <https://link.aps.org/doi/10.1103/PhysRevB.75.195212>.
- [150] Yuta Aoki and Susumu Saito. “Impurities Effects on the Electronic Structure of Titanium Dioxide”. In: *Journal of Physics: Conference Series* 302.1 (2011), p. 012034. DOI: 10.1088/1742-6596/302/1/012034. URL: <https://iopscience.iop.org/article/10.1088/1742-6596/302/1/012034/meta>.
- [151] Li-Bin Mo et al. “Hydrogen Impurity Defects in Rutile TiO<sub>2</sub>”. In: *Scientific Reports* 5.1 (2015), p. 17634. DOI: 10.1038/srep17634. URL: [www.nature.com/scientificreportshttp://www.nature.com/articles/srep17634](http://www.nature.com/scientificreportshttp://www.nature.com/articles/srep17634).
- [152] Michele Reticcioli et al. “Small Polarons in Transition Metal Oxides”. In: *Handbook of Materials Modeling: Applications: Current and Emerging Materials*. Ed. by Wanda Andreoni and Sidney Yip. Cham: Springer International Publishing, 2019, pp. 1–39. ISBN: 978-3-319-50257-1. DOI: 10.1007/978-3-319-50257-1\_52-1. URL: [https://doi.org/10.1007/978-3-319-50257-1\\_52-1](https://doi.org/10.1007/978-3-319-50257-1_52-1).
- [153] Lili Zhang et al. “Dynamics of Photoexcited Small Polarons in Transition-Metal Oxides”. In: *The Journal of Physical Chemistry Letters* 12.9 (2021), pp. 2191–2198. DOI: 10.1021/acs.jpcclett.1c00003. URL: <https://pubs.acs.org/doi/full/10.1021/acs.jpcclett.1c00003><https://pubs.acs.org/doi/10.1021/acs.jpcclett.1c00003>.
- [154] J. Schnakenberg. “Polaronic Impurity Hopping Conduction”. In: *physica status solidi (b)* 28.2 (1968), pp. 623–633. DOI: <https://doi.org/10.1002/pssb.19680280220>. URL: <https://onlinelibrary.wiley.com/doi/abs/10.1002/pssb.19680280220>.

- [155] Sergei Baranovskii and Oleg Rubel. “Charge Transport in Disordered Materials”. In: *Springer Handbook of Electronic and Photonic Materials*. Ed. by Safa Kasap and Peter Capper. Cham: Springer International Publishing, 2017, pp. 1–1. ISBN: 978-3-319-48933-9. DOI: 10.1007/978-3-319-48933-9\_9. URL: [https://doi.org/10.1007/978-3-319-48933-9\\_9](https://doi.org/10.1007/978-3-319-48933-9_9).
- [156] C. F. Richardson and N. W. Ashcroft. “High Temperature Superconductivity in Metallic Hydrogen: Electron-Electron Enhancements”. In: *Phys. Rev. Lett.* 78 (1 1997), pp. 118–121. DOI: 10.1103/PhysRevLett.78.118. URL: <https://link.aps.org/doi/10.1103/PhysRevLett.78.118>.
- [157] Chris J. Pickard, Ion Errea, and Mikhail I. Erements. “Superconducting Hydrides Under Pressure”. In: *Annu. Rev. Conden. Mater. Phys.* 11.1 (2020), pp. 57–76. DOI: 10.1146/annurev-conmatphys-031218-013413. URL: <https://doi.org/10.1146/annurev-conmatphys-031218-013413>.
- [158] Francesco Belli et al. “Strong correlation between electronic bonding network and critical temperature in hydrogen-based superconductors”. In: *Nature Commun.* 12.1 (2021), p. 5381. ISSN: 2041-1723. DOI: 10.1038/s41467-021-25687-0. URL: <https://www.nature.com/articles/s41467-021-25687-0>.
- [159] A. P. Drozdov et al. “Conventional superconductivity at 203 kelvin at high pressures in the sulfur hydride system”. In: *Nature* 525.7567 (2015), pp. 73–76. DOI: 10.1038/nature14964.
- [160] Defang Duan et al. “Pressure-induced metallization of dense (H<sub>2</sub>S)<sub>2</sub>H<sub>2</sub> with high-T<sub>c</sub> superconductivity”. In: *Sci. Rep.* 4.1 (2014), p. 6968. DOI: 10.1038/srep06968.
- [161] Ion Errea et al. “Quantum hydrogen-bond symmetrization in the superconducting hydrogen sulfide system”. In: *Nature* 532 (2016), pp. 81–84. DOI: 10.1038/nature17175.

- [162] Alexander F. Goncharov et al. “Synthesis and structure of carbon-doped H<sub>3</sub>S compounds at high pressure”. In: *J. Appl. Phys.* 131.2 (2022), p. 025902. DOI: 10.1063/5.0073499. URL: <https://doi.org/10.1063/5.0073499>.
- [163] Wenwen Cui et al. “Route to high- $T_c$  superconductivity via CH<sub>4</sub>-intercalated H<sub>3</sub>S hydride perovskites”. In: *Phys. Rev. B* 101 (13 2020), p. 134504. DOI: 10.1103/PhysRevB.101.134504. URL: <https://link.aps.org/doi/10.1103/PhysRevB.101.134504>.
- [164] Ying Sun et al. “Computational discovery of a dynamically stable cubic SH<sub>3</sub>-like high-temperature superconductor at 100 GPa via CH<sub>4</sub> intercalation”. In: *Phys. Rev. B* 101 (17 2020), p. 174102. DOI: 10.1103/PhysRevB.101.174102. URL: <https://link.aps.org/doi/10.1103/PhysRevB.101.174102>.
- [165] Yanfeng Ge et al. “Hole-doped room-temperature superconductivity in H<sub>3</sub>S<sub>1-x</sub>Z<sub>x</sub> (Z=C, Si)”. In: *Materials Today Physics* 15 (2020), p. 100330. DOI: <https://doi.org/10.1016/j.mtphys.2020.100330>. URL: <https://www.sciencedirect.com/science/article/pii/S2542529320301541>.
- [166] S. X. Hu et al. *Carbon-Doped Sulfur Hydrides as Room-Temperature Superconductors at 270 GPa*. 2020. arXiv: 2012.10259 [cond-mat.supr-con].
- [167] Tianchun Wang et al. “Absence of conventional room-temperature superconductivity at high pressure in carbon-doped H<sub>3</sub>S”. In: *Phys. Rev. B* 104 (6 2021), p. 064510. DOI: 10.1103/PhysRevB.104.064510. URL: <https://link.aps.org/doi/10.1103/PhysRevB.104.064510>.
- [168] Xiaoyu Wang et al. *A Little Bit of Carbon Can do a Lot for Superconductivity in H<sub>3</sub>S*. 2021. arXiv: 2109.09898 [cond-mat.supr-con].
- [169] Dale R. Harshman and Anthony T. Fiory. “The superconducting transition temperatures of C–S–H based on inter-sublattice S–H<sub>4</sub>-tetrahedron electronic interactions”. In: *J. Appl. Phys.* 131.1 (2022), p. 015105. DOI: 10.1063/5.0065317. URL: <https://doi.org/10.1063/5.0065317>.

- [170] Lazar Novakovic et al. “Dispersion interactions in proposed covalent superhydride superconductors”. In: *Phys. Rev. B* 105 (2 2022), p. 024512. DOI: 10.1103/PhysRevB.105.024512. URL: <https://link.aps.org/doi/10.1103/PhysRevB.105.024512>.
- [171] Ivan A. Troyan et al. “Anomalous High-Temperature Superconductivity in YH6”. en. In: *Advanced Materials* 33.15 (2021), p. 2006832. ISSN: 1521-4095. DOI: 10.1002/adma.202006832.
- [172] Xiaohua Zhang et al. “Pressure-induced hydride superconductors above 200 K”. In: *Matter Radiat. at Extremes* 6.6 (2021), p. 068201. DOI: 10.1063/5.0065287. URL: <https://doi.org/10.1063/5.0065287>.
- [173] Guoyin Shen et al. “Toward an international practical pressure scale: A proposal for an IPPS ruby gauge (IPPS-Ruby2020)”. In: *High Pressure Research* 40.3 (2020), pp. 299–314. DOI: 10.1080/08957959.2020.1791107. URL: <https://doi.org/10.1080/08957959.2020.1791107>.
- [174] Dean Smith et al. “Simple imaging for the diamond anvil cell: Applications to hard-to-reach places”. In: *Rev. Sci. Instrum.* 89.10 (2018), p. 103902. DOI: 10.1063/1.5048316.
- [175] M. Einaga et al. “Crystal structure of the superconducting phase of sulfur hydride”. In: *Nature Phys* 12 (2016), pp. 835–838. DOI: 10.1038/nphys3760.
- [176] M. S. Somayazulu et al. “High-Pressure Compounds in Methane-Hydrogen Mixtures”. In: *Science* 271.5254 (1996), pp. 1400–1402. ISSN: 0036-8075. DOI: 10.1126/science.271.5254.1400. URL: <https://www.sciencemag.org/lookup/doi/10.1126/science.271.5254.1400>.
- [177] Timothy A. Strobel et al. “Novel Cooperative Interactions and Structural Ordering in H<sub>2</sub>S–H<sub>2</sub>”. In: *Phys. Rev. Lett.* 107 (25 2011), p. 255503. DOI: 10.1103/PhysRevLett.107.255503. URL: <https://link.aps.org/doi/10.1103/PhysRevLett.107.255503>.

- [178] J. D. Bernal and R. H. Fowler. “A Theory of Water and Ionic Solution, with Particular Reference to Hydrogen and Hydroxyl Ions”. In: *J. Chem. Phys.* 1.8 (1933), pp. 515–548. DOI: 10.1063/1.1749327. URL: <https://doi.org/10.1063/1.1749327>.
- [179] Kyuho Lee et al. “Higher-accuracy van der Waals density functional”. In: *Phys. Rev. B* 82 (8 2010), p. 081101. DOI: 10.1103/PhysRevB.82.081101.
- [180] Arijit Das et al. “The H<sub>2</sub>S Dimer is Hydrogen-Bonded: Direct Confirmation from Microwave Spectroscopy”. In: *Angew. Chem., Int. Ed.* 57.46 (2018), pp. 15199–15203. DOI: <https://doi.org/10.1002/anie.201808162>.
- [181] Edward J. Pace et al. “Properties and phase diagram of (H<sub>2</sub>S)<sub>2</sub>H<sub>2</sub>”. In: *Phys. Rev. B* 101 (17 2020), p. 174511. DOI: 10.1103/PhysRevB.101.174511. URL: <https://link.aps.org/doi/10.1103/PhysRevB.101.174511>.
- [182] Viktor V. Struzhkin et al. “Synthesis of sodium polyhydrides at high pressures”. en. In: *Nature Communications* 7.11 (2016), p. 12267. ISSN: 2041-1723. DOI: 10.1038/ncomms12267.
- [183] Takahiro Matsuoka et al. “Electrical Properties of YH<sub>3</sub> under High Pressure”. In: *Journal of the Physical Society of Japan* 76.Suppl.A (2007), pp. 86–87. ISSN: 0031-9015. DOI: 10.1143/JPSJS.76SA.86.
- [184] Duck Young Kim, Ralph H. Scheicher, and Rajeev Ahuja. “Predicted High-Temperature Superconducting State in the Hydrogen-Dense Transition-Metal Hydride YH<sub>3</sub> at 40 K and 17.7 GPa”. In: *Physical Review Letters* 103.7 (2009), p. 077002. DOI: 10.1103/PhysRevLett.103.077002.
- [185] Jonathan E. Moussa and Marvin L. Cohen. “Two bounds on the maximum phonon-mediated superconducting transition temperature”. In: *Physical Review B* 74.9 (2006), p. 094520. DOI: 10.1103/PhysRevB.74.094520.



- [186] Lu-Lu Liu et al. “High-pressure structures of yttrium hydrides”. en. In: *Journal of Physics: Condensed Matter* 29.32 (2017), p. 325401. ISSN: 0953-8984. DOI: 10.1088/1361-648X/aa787d.
- [187] Clemens Prescher and Vitali B. Prakapenka. “DIOPTAS: a program for reduction of two-dimensional X-ray diffraction data and data exploration”. In: *High Pressure Res.* 35.3 (2015), pp. 223–230. DOI: 10.1080/08957959.2015.1059835.
- [188] *Rigaku Oxford Diffraction, CrysAlisPro Software system, Version 171.40.64.67a, Rigaku Corporation, Oxford, UK.*
- [189] George M. Sheldrick. “*SHELXT* – Integrated space-group and crystal-structure determination”. In: *Acta Cryst. A* 71.1 (2015), pp. 3–8. DOI: 10.1107/S2053273314026370. URL: <https://doi.org/10.1107/S2053273314026370>.
- [190] G.M. Sheldrick. “A short history of SHELX”. In: *Acta Cryst. A* 64 (2008), pp. 112–122. DOI: 10.1107/S0108767307043930.
- [191] Christian B. Hübschle, George M. Sheldrick, and Birger Dittrich. “*ShelXle*: a Qt graphical user interface for *SHELXL*”. In: *J. Appl. Crystallogr.* 44.6 (2011), pp. 1281–1284. DOI: 10.1107/S0021889811043202. URL: <https://doi.org/10.1107/S0021889811043202>.
- [192] James D. Pack and Hendrik J. Monkhorst. ““Special points for Brillouin-zone integrations”—a reply”. In: *Phys. Rev. B* 16.4 (1977), pp. 1748–1749. DOI: 10.1103/physrevb.16.1748.
- [193] P. E. Blöchl. “Projector augmented-wave method”. In: *Phys. Rev. B* 50 (24 1994), pp. 17953–17979. DOI: 10.1103/PhysRevB.50.17953.

## CURRICULUM VITAE

### G. Alexander Smith

University of Nevada, Las Vegas Las Vegas, NV, 89154-4002 *E-mail:*Smith613@live.com

#### Professional Preparation

---

##### UNDERGRADUATE

University of Nevada, Las Vegas B.Sc. Chemistry 12/2018

University of Nevada, Las Vegas B.Sc. Applied Physics 12/2018

##### GRADUATE

University of Nevada, Las Vegas Ph.D. Chemistry 5/2023

PhD title: *Stoichiometric determination of hydride materials at extreme conditions*

#### Research Interests

---

I am interested in exploring the evolution of coordination under extreme conditions and the resulting effects on bulk properties. Studying these systems with multiple complimentary probes in situ, allows for a more complete description of the behavior of a material across complicated thermodynamic landscapes. I enjoy applying and adapting established probes that are uncommon to the diamond anvil cell to expand the breadth of measurements at high pressures. I strive for the advancement of metrology to achieve coherent, high-quality, and transparent data under high-pressure and temperature conditions necessary for the synthesis of exciting, new materials.

## Notable Awards

---

### 2022 GRC Poster Award

Determining stoichiometries of clathrate-like yttrium hydride under megabar conditions

### 2022 GRC Carl Storm Underrepresented Minority Fellowship recipient

### 2020 PLS&PS Graduate Intern at Lawrence Livermore National Lab

2016-present Participated in over 100 shifts of beamtime across various x-ray facilities such as the APS, CLS, ESRF, EuXFEL, and SLS

## Teaching

CHEM122L - General Chemistry Lab II (2018-2020)

## Graduate Advisor and Other Research Sponsors

Graduate Advisor

Ashkan Salamat (UNLV, US)

Livermore PLS&PS Internship Advisor

Federica Coppari (LLNL, US)

## Publications - 8

---

(8) C. Childs, D. Smith, **G. A. Smith**, P. Ellison, D. Sneed, J. Hinton, E. Siska, J. S Pigott, E. Rod, W. O'Donnell, R. Salem, B. Sturtevant, R. J Scharff, N. Velisavljevic, C. Park, A. Salamat *CO<sub>2</sub> laser heating system for in situ radial x-ray absorption at 16-BM-D at the Advanced Photon Source* Review of Scientific Instruments **93**, 8, 083901 (2022)

(7)**G. A. Smith**, I. E Collings, E. Snider, D. Smith, S. Petitgirard, J. S Smith, M. White, E. Jones, P/ Ellison, K. V Lawler, R. P Dias, A. Salamat *Carbon content drives high temperature superconductivity in a carbonaceous sulfur hydride below 100 GPa* Chemical Communications **58**, 65, 9064-9067 (2022)

(6)D. Sayre, E. Siska, **G. Alexander Smith**, Nicholas Chang, Changyong Park, Frederic Poineau, Craig P. Schwartz, Keith V. Lawler, A. Salamat\* *Pressure-induced metallization and 3d-like behavior in TcS<sub>2</sub>* Chemical Communications **58**, 46, 6634-6637 (2022)

(5)**G. Alexander Smith**, D. Schacher, J. K Hinton, D. Sneed, C. Park, S. Petitgirard, K. V Lawler, A. Salamat\*, *Prevalence of pretransition disordering in the rutile-to-CaCl<sub>2</sub> phase transition of GeO<sub>2</sub>* Physical Review B, **104**, 13, 134107 (2021)

(4)D. Durkee, N. Dasenbrock-Gammon, **G. A. Smith**, E. Snider, D. Smith, C. Childs, S. AJ Kimber, K. V Lawler, R. P Dias, A. Salamat\* *Colossal Density-Driven Resistance Response in the Negative Charge Transfer Insulator MnS<sub>2</sub>* Physical Review Letters, **127**, 1, 016401 (2021)

(3)S. R Mulligan, E. Stavrou, S. Chariton, O. Tschauner, A. Salamat, M. L Wells\*, **A. G. Smith**, T. D Hoisch, V. Prakapenka, *Equation of State for Natural Almandine, Spessartine, Pyrope Garnet: Implications for Quartz-In-Garnet Elastic Geobarometry* Minerals, **11**, 5, 458 (2021)

(2)D. Smith, D. Sneed, N. Dasenbrock-Gammon, E. Snider, **G. Alexander Smith**, C. Childs, J. S. Pigott, N. Velisavljevic, C. Park, K. V. Lawler, R. P Dias, A. Salamat\*, *Anomalous Conductivity in the Rutile Structure Driven by Local Disorder* The Journal of Physical Chemistry Letters 10 **18** 5351-5356 (2019)

(1)D. Smith, K. V. Lawler, M. Martinez-Canales, A. W. Daykin, Z. Fussell, **G. A. Smith**, C. Childs, J. S. Smith, C. J. Pickard, A. Salamat\*, *Postaragonite phases of CaCO<sub>3</sub> at lower mantle pressures* Physical Review M **2**, 013605 (2018)

Metrics and complete works can be found through the following Google Scholar link:

[https://scholar.google.com/citations?user=zU\\_TQEQAAAAJ&hl=en](https://scholar.google.com/citations?user=zU_TQEQAAAAJ&hl=en)